DOE/PC/90185--T16

Final Technical Report

Principal Investigator: Mark Richman

Contract Number: DE-AC22-91PC90185

TABLE OF CONTENTS

1. GRANULAR FLOWS OF NEARLY ELASTIC SPHERES DOWN INCLINES: NUMERICAL SOLUTIONS

In this chapter, we focus attention on unconfined, gravity driven granular flows of nearly elastic, identical spheres down bumpy inclines. We do so in order to develop a numerical solution technique that will overcome the difficulties associated with the ill-defined "tops" of these flows. Although the constitutive theory and boundary conditions for nearly elastic particles are not as complex as those that we will develop for highly inelastic particles, the numerical problems associated with flows that extend without bound above the incline are common to assemblies of both nearly elastic and highly inelastic particles. It is therefore our intention first to resolve these problems in the context of the simpler theory.

We will employ the constitutive relations of Jenkins and Richman [1985] and boundary conditions of Richman [1988]. We solve the full equations numerically, and compare the results to those obtained by Richman and Marciniec [1990], who obtained approximate closed form solutions by replacing the solid fraction by its depth averaged value wherever it occurred in the balance equations. In addition, we parameterize the results to facilitate qualitative comparisons with recent experimental studies (Johnson et. al. [1990], for example).

1.1 The Boundary Value Problem

Here we consider steady, fully developed granular flows down bumpy inclines in which the mean velocity is parallel to the flat part of the bumpy incline, and in which spatial variations of the mean fields occur only in the direction perpendicular to that of the mean flow.

We employ a Cartesian coordinate system in which x_1 points in the direction of flow velocity u_1, and x_2 defines the direction upon which the mean fields depend and measures perpendicular distance from the incline. The flows are infinite in the x_1- and x_3-directions. The vertical acceleration due to gravity is g, and the angle between the incline and the horizontal is ϕ. For purposes of nondimensionalization, we introduce the characteristic velocity a. The dimensionless fields of solid fraction ν, velocity $u \equiv u_1/a$, and the measure $w^2 \equiv T/a^2$ of granular temperature depend only on the dimensionless coordinate $Y \equiv x_2/\sigma$.

In these flows, the balance of mass and the x_3-component of the balance of momentum are identically satisfied. If $S \equiv -P_{12}/(\rho_p a^2)$ and $P \equiv P_{22}/\rho_p a^2$ are the dimensionless counterparts of the x_1-x_2 and x_2-x_2 components P_{12} and P_{22} of the pressure tensor, then the x_1-component of the momentum equation is

$$S' = \frac{-\sigma g}{a^2} \nu \sin\phi \quad , \tag{1}$$

where a prime denotes differentiation with respect to Y, and the x_2-component of the momentum equation is

$$P' = \frac{\sigma g}{a^2} \nu \cos\phi \quad . \tag{2}$$

If $q \equiv -Q_2/\rho_p a^3$ and energy dissipation $\Gamma \equiv \sigma\gamma/\rho_p a^3$ are the dimensionless counterparts to the x_2-component Q_2 of the energy flux and the energy dissipation γ, then the balance of energy reduces to

$$q' + Su' - \Gamma = 0 \quad . \tag{3}$$

It remains to express the constitutive relations in dimensionless form. Here and in what follows we take $a^2 = \sigma g$.

Here we employ the constitutive theory of Jenkins and Richman [1985]. The isotropic piece of the pressure tensor gives,

$$P = 4\nu G F w^2 \quad , \tag{4}$$

where $G \equiv \nu(2-\nu)/2(1-\nu)^3$ and $F \equiv 1+1/4G$, and the deviatoric piece gives,

$$S = \frac{2EPu'}{5\sqrt{\pi} F w} \quad , \tag{5}$$

where $E \equiv 1+\pi(1+5/8G)^2/12$. Equation (5) can be rearranged to express the velocity gradient u' in terms of the ratio S/P according to

$$u' = \frac{5\sqrt{\pi} F w S}{2EP} \quad . \tag{6}$$

The constitutive relations for q and Γ are,

$$q = \frac{2MPw'}{\sqrt{\pi}\, F} \quad , \tag{7}$$

where $M \equiv 1+9\pi(1+5/12G)^2/32$, and

$$\Gamma = \frac{6(1-e)Pw}{\sqrt{\pi} F} \quad . \tag{8}$$

Following Richman and Marciniec [1990], we employ equations (7), (6), and (8) to eliminate q, u', and Γ from equation (3), and differentiate equation (4) with respect to Y to write v' in terms of P' and w' wherever it appears. The energy equation can then be written in terms of w and its derivatives:

$$\frac{w''}{w} + \left[(1-2h)\frac{P'}{P}\right]\frac{w'}{w} + 4h\left(\frac{w'}{w}\right)^2 - \lambda^2 = 0 \quad , \tag{9}$$

where λ^2 is defined by

$$\lambda^2 \equiv \frac{1}{2M}\left[6(1-e) - \frac{5\pi F^2 S^2}{2EP^2}\right] \quad , \tag{10}$$

and 2h is the function of solid fraction defined by

$$2h \equiv \frac{-d[\ln(M/F)]/dv}{d[\ln(vGF)]/dv} \quad . \tag{11}$$

The quantity λ^2 is a local measure of the difference between the rate at which energy is dissipated by inelastic collisions and the rate at which energy is supplied to the flow by gravity.

The conditions at the free surface reflect the facts that normal stress, shear stress, and energy flux vanish there:

$$P=0 \quad \text{and} \quad S=0 \quad , \tag{12}$$

and

$$w'=0 \quad . \tag{13}$$

According to Richman and Marciniec [1990], the conditions at the bumpy base determine the slip velocity $v \equiv u(Y=0)$ according to,

$$\frac{v}{w} = \sqrt{\frac{\pi}{2}\frac{S}{P}}\,f \tag{14}$$

in which the dependence of f on boundary geometry and solid fraction is given by,

$$f = \frac{1-\frac{5\bar{\sigma}F}{2^{3/2}\sigma E}(1+\frac{\sigma A}{\bar{\sigma}})\sin^2\theta}{\frac{2}{3}[2(1-\cos\theta)\csc^2\theta-\cos\theta]} + \frac{5\bar{\sigma}F}{2^{3/2}\sigma E} \quad , \tag{15}$$

where $A \equiv \pi(1+5/8G)/12\sqrt{2}$; and the temperature gradient according to,

$$\frac{w'}{w} = -b \quad , \tag{16}$$

in which the dependence of b on boundary geometry and solid fraction is given by,

$$b = \frac{F}{2^{1/2}M}\left[\frac{\pi S^2}{2P^2} f - 2(1-e_w)(1-\cos\theta)\csc^2\theta\right] \quad . \tag{17}$$

The quantity b is the dimensionless difference between the slip work done by the boundary, and the collisional dissipation at the boundary. The boundary supplies fluctuation energy to the flow when b is positive and absorbs fluctuation energy when b is negative.

1.2 Numerical Solution Procedure

In what follows, we take the characteristic velocity $a=(\sigma g)^{1/2}$. Because the velocity has been eliminated from the energy equation and the stress ratio S/P is equal to $\tan\phi$, equations (2) for P(Y), (9) for w(Y), and the constitutive equation (4) for P are uncoupled from equations (1) for S(Y), and (6) for u(Y). Consequently, for fixed values of e, e_w, r, Δ, and ϕ, equations (2), (9), and (4) determine the functions P(Y), w(Y), and v(Y) to within three constants of integration. These three constants and the depth of flow $Y=\beta$ are determined by the second of the stress free conditions (12) at the free surface, energy flux conditions (13) and (16) at the free surface and at the base, and by prescribing the mass hold-up m_t defined by the integral,

$$m_t \equiv \int_0^\beta v(Y)\, dY \tag{18}$$

With v(Y) known, equation (1) may be integrated to determine S(Y) to within a constant of integration that is fixed by the first of stress conditions (12). Alternatively, with P(Y) known, S(Y) is given simply by the product $P(Y)\tan\phi$. Independent of the variation S(Y) but with v(Y) and w(Y) known, equation (6) may be integrated to determine u(Y) to within a constant that is fixed by momentum flux condition (14). The corresponding mass flow rate $\dot{m}$ may then be calculated according to its definition,

$$\dot{m} \equiv \int_0^\beta v(Y)u(Y)\,dY \quad . \tag{19}$$

We employ a fourth order Runge-Kutta technique to integrate equations (2), (9), and (4) from the free surface, where both P and w' vanish, but where the value W of w is not known. In order to parameritize the problem by m_t, we guess at the value of W, integrate the equations from the free surface to the depth at which energy flux condition (16) is satisfied, calculate m_t according to its definition (18), and iterate on W until m_t is equal to its prescribed value.

To carry out the integrations, in equation (9), we employ equations (2) and (4) to write the ratio P'/P as $\cos\phi/(1+4G)w^2$. Whenever necessary, we invert equation (4) to calculate the value of v corresponding to known values of P and w. However, according to constitutive relation (4), v must be equal to zero if P vanishes where w does not. In particular, v must be equal to zero at the free surface. Because the w' is also equal to zero there, equations (2), (4) and (9) demonstrate that P', v', and w'' each vanish at the free surface. Integrations initiated from the top of the flow therefore yield no spatial variations in P, w, and v. This indicates that the theory predicts flows that are infinitely deep and that P, w and v approach their free surface values asymptotically from the base. To overcome this difficulty, we set v at the free surface equal to 10^{-6}, which is equivalent to relaxing very slightly the normal stress condition there, and allows the integrations to proceed away from zero. We have also initiated the integrations with several other values of v between 10^{-5} and 10^{-7}, and in each case obtained results that were indistinguishable from those based on $v=10^{-6}$.

For any value of W, the integrations are concluded when the basal energy flux condition (16) is satisfied. Interestingly, condition (16) may be satisfied at more than one location, and therefore there may be more than one steady, fully developed, solution for that choice of W. If this condition is not satisfied within 800 particle diameters from where the integrations were initiated, then we conclude that no steady, fully developed solution exists for the value of W chosen. If this condition is satisfied, then P(Y), w(Y), and v(Y) are completely determined, and equations (1) and (6) may be integrated numerically to determine S(Y) and u(Y).

1.3 Results and Discussion

In Figure 1.1 we show the variations of $\dot{m}$ with W between 0 and 3 for $e=.8$, $e_w=.95$, $r=1/2$, and $\Delta=-1+2^{1/2}$ at inclinations ϕ of 19.00°, 20.04°, 20.70°, 21.00°, and 21.50° obtained numerically. The numerical solution predicts steady, fully developed flows also occur at these inclinations when W is greater than 3. However, the solid fraction in these flows is everywhere less than .02. The theory predicts that when W is extremely small (<.02), the flows are unrealistically dense. In fact, the lowest value of W on each curve shown in Figure 1.1 corresponds to the minimum value at which the solid fraction everywhere within the flow is less than .65. As W increases from its minimum value, although the flow rates do not vary monotonically, the flows become monotonically more dilute.

In Figure 1.2 we show the variations of $\dot{m}$ with W for $e=.95$, $e_w=.8$, $r=1/2$, and $\Delta=-1+2^{1/2}$ at inclinations ϕ of 11.56°, 11.80°, 12.00°, 12.20°, and 12.90° obtained numerically. Corresponding to each inclination is a finite maximum value of W at which $\dot{m}$ becomes unbounded. When $\phi=12.90°$, as W increases from its minimum value at which the solid fraction everywhere within the flow is less than .65 to its maximum value, the flows become increasingly more dilute. At the remaining inclinations, two flows at different flow rates are physically possible for fixed values of W near its minimum. As W increases from its minimum value, the flow at the higher flow rate becomes more dense until, at a value of W that is less than its maximum, the solid fraction somewhere in the flow reaches .65. The flow at the lower flow rate becomes more dilute as W increases to its maximum value.

To each value of W for which the numerical solution predicts that a steady, fully developed flow occurs, there corresponds a mass hold-up m_t that may be calculated according to its definition (18). In addition to $\dot{m}$ and m_t, the parameters that measure the overall character of the flows, such as the depth of flow β, the depth-averaged solid fraction,

$$\tilde{\nu} \equiv \frac{1}{\beta} \int_0^{\beta} \nu(Y)dY \tag{20}$$

and the depth-averaged velocity,

$$\tilde{u} \equiv \frac{1}{\beta} \int_0^{\beta} u(Y)dY \tag{20}$$

may also be calculated.

Because the numerical integrations in the Runge-Kutta solutions are initiated from a small value of ν, to each parameter set (e, e_w, r, Δ, ϕ, and W), there corresponds a region at the top of the flow in which the solid fraction is essentially zero and the variations of the other mean fields are negligible. However, the depth of this region is as arbitrary as the choice of $\nu(Y=\beta)$. In order to make the numerical determination of the depth β more precise, we take it as the distance from the incline to the point Y below which 99% of the mass m_t is contained. In each figure in this chapter, we have calculated all the numerical solutions' depth-averaged values based on this new definition of β.

In Figure 1.3, for example, we eliminate W and show as a solid curve the variation of $\dot{m}$ with m_t when $\phi=20.70°$ for the values $e=.8$, $e_w=.95$, $r=1/2$, and $\Delta=-1+2^{1/2}$ taken from the numerical solutions in Figure 1.1. In Figures 1.4, 1.5, and 1.6 we show as solid lines the corresponding variations of $\bar{\nu}$, β, and $\bar{u}$. Also shown in Figures 1.3, 1.4, 1.5, and 1.6, as dashed curves are the corresponding variations predicted by the approximate solution obtained by Richman and Marciniec [1990]. In either case, we stop the lines whenever the solid fraction exceeds .65 anywhere in the flow. The most striking feature of the curves in Figures 1.1 and 1.3 is that they demonstrate that there are flow rates at which two very different flows can occur.

For convenience, in each of these figures we have labeled points a, b, c, and d on the numerical solid lines with respective flow rates $\dot{m}=10.0$, 17.8, 50.0, and 134.0. Whenever two solutions exist for the same flow rate, the second, more massive solution (i.e. higher mass hold-up, m_t) is distinguished from the first by a primed label. For example, there exists two numerical solutions at $\dot{m}=17.8$. The less massive one (point b) at $m_t=1.7$ and the more massive (point b') at $m_t=5.4$. In a similar manner, we label corresponding points on the approximate dashed lines with greek letters α, β, γ, and δ. The values of $\dot{m}$, m_t, $\bar{\nu}$, β, and $\bar{u}$ associated with each point labeled in Figures 1.3 through 1.6 are summarized in Table 1.1.

Table 1.1 Points in Figures 1.3-1.6

Point	m_t	$\dot{m}$	$\bar{v}$	β	$\bar{u}$
a	1.25	10.00	.06	20.07	10.21
b	1.67	17.80	.08	20.86	13.26
b'	5.42	17.80	.60	8.94	3.23
c	2.81	50.00	.12	22.58	20.56
c'	5.88	50.00	.48	12.07	8.42
d	5.55	133.94	.28	19.51	23.72
α	1.43	10.00	.13	10.68	8.00
β	1.85	17.80	.14	12.99	10.80
β'	5.56	17.80	.60	9.32	3.22
γ	2.88	50.00	.16	18.58	18.60
γ'	6.30	50.00	.50	12.65	7.82
δ	4.29	133.94	.16	26.36	31.20
δ'	7.77	133.94	.45	17.33	16.40

For the case $\phi=20.70°$ shown in Figures 1.1 and 1.3, the numerical solution predicts that there are two flows possible for fixed flow rates between the maximum 134.0 (point d) and 17.8 (points b and b'); the less massive flow is more dilute, faster, and more thermalized than its more massive counterpart. As $\dot{m}$ decreases in this range, the flow at the higher mass hold-up becomes more dense, slower, and less thermalized, until at $\dot{m}=17.8$ the solid fraction within the flow exceeds .65 and we assume it can no longer be sheared. As $\dot{m}$ decreases from its maximum value to 1, the flow at the lower mass hold-up becomes more dilute, slower, and more thermalized. Quantitatively similar observations may be made for the other inclinations shown in Figure 1.1.

In Figure 1.7 we show as a solid curve the variation of $\dot{m}$ with m_t when $\phi=12.20°$ for the values $e=.95$, $e_w=.8$, $r=1/2$, and $\Delta=-1+2^{1/2}$ taken from the numerical solutions in Figure 1.2, and the same approximate variation as a dashed curve. Figures 1.8, 1.9, and 1.10 show as solid curves (or dashed curves) the corresponding variations of $\bar{v}$, β, and $\bar{u}$ predicted by the numerical (or approximate) solution. Again, the most striking feature of the curves in Figure 1.7 is that it demonstrates that there are flow rates at which two very different flows can occur.

In these figures we label points a, b, c, and d on the numerical solid lines and the corresponding points α, β, α, γ, and δ on the approximate dashed lines, whose respective flow rates are 100, 50, 20, and 10.6. The values of $\dot{m}$, m_t, $\bar{v}$, \beta, and $\bar{u}$ associated with each point labeled in Figures 1.7 through

1.10 are summarized in Table 1.2. In this case, the numerical solution predicts two steady, fully developed flows for fixed flow rates between the minimum 10.6 (point d) and 56.7. Of the two, the less massive is more dilute, faster, and more thermalized than its more massive counterpart. As $\dot{m}$ increases from 10.6 the less massive flow becomes more dilute, faster, and more thermalized. The more massive flow becomes more dense, faster, and only slightly less thermalized, until at $\dot{m}=56.7$ the solid fraction somewhere within the flow exceeds .65. Qualitatively similar observations may be made for the other inclinations shown in Figure 1.2.

Table 1.2 Points in Figures 1.7-1.10

Point	m_t	$\dot{m}$	$\bar{v}$	β	$\bar{u}$
a	4.30	100.00	.06	73.64	33.05
b	3.38	50.00	.07	50.50	21.03
b'	8.89	50.00	.38	23.11	7.47
c	2.55	20.00	.09	27.53	10.94
c'	4.65	20.00	.29	15.57	5.56
d	2.48	10.58	.17	14.60	5.69
α	4.37	100.00	.09	47.98	31.06
β	3.37	50.00	.10	33.57	19.71
β'	9.79	50.00	.49	19.82	5.89
γ	2.45	20.00	.12	20.10	10.52
γ'	5.70	20.00	.44	13.09	4.05
δ	2.02	10.58	.15	13.55	6.56
δ'	3.74	10.58	.38	9.87	3.27

According to Figures 1.3 and 1.7, for those flow rates at which steady, fully developed flows are predicted by both the numerical and approximate solutions, the values of m_t predicted by the two agree quite well. However, according to Figure 1.3, there can be a considerable discrepancy between. the two predictions concerning the range of flow rates within which steady flows are possible.

In Figures 1.11, 1.12, and 1.13 we plot as solid curves the numerical variations of v, w, and u with Y for the case $\phi=20.70°$, $e=.8$, $e_w=.95$, $r=1/2$, and $\Delta=-1+2^{1/2}$ when $\dot{m}=50$. In Figures 1.14, 1.15, and 1.16 we do the same for the case $\phi=12.20°$, $e=.95$, $e_w=.8$, $r=1/2$, and $\Delta=-1+2^{1/2}$. Shown as dashed lines are the corresponding approximate variations. As demonstrated in Figures 1.3 and 1.7, two steady, fully developed flows are possible in both cases. The light curves correspond to the less massive of the two flows and the dark lines correspond to the more massive of the two. In the first case (shown in shown in Figures 1.11, 1.12, and 1.13), the mass hold-ups for the two numerical solutions are m_t=2.81 (point c in Figure 1.3) and 5.88 (point c' in Figure 1.3), and for the two approximate solutions are m_t=2.88 (point γ on Figure 1.3) and 6.30 (point γ' on Figure 1.3). In the second case (shown in shown in Figures 1.14, 1.15, and 1.16), the numerical values are m_t=3.38 (point b in Figure 1.7) and 8.89 (point b' in Figure 1.3), and the approximate values are m_t=3.37 (point β on Figure 1.7) and 9.79 (point β' on Figure 1.7).

Figures 1.11 and 1.14 demonstrate that the approximate solid fraction profiles reach zero at finite distances from the base, whereas the exact profiles vanish only as the distance form the base becomes unbounded. The approximate solutions corresponding to the dilute and dense flows shown in Figures 1.11, 1.12, and 1.13, for example, predict depths 18.58 and 12.65 particles diameters, respectively. Although the corresponding numerical solutions include no such predictions, they do demonstrate that 95.2 percent of the mass of the dilute flow and 99.99 percent of the mass of the dense flow are contained within the depths predicted by the approximate analysis. Similarly, the approximate dilute and dense profiles shown in Figures 1.14, 1.15, 1.16 have depths of 33.6 and 19.8 particle diameters respectively, while the numerical solutions contain 93.3 and 95.5 percent of the total mass of the corresponding flows within these depths. Consequently, although the exact profiles of 1w and u extend indefinitely above the incline whereas their approximate counterparts end abruptly, this discrepancy is not serious. In order to emphasize this fact, we have indicated the locations at which ν=.01 by solid dots on the numerically obtained profiles of u and w shown in Figures 1.12, 1.13, 1.15, and 1.16.

The dependence of mass flow rate on mass hold-up shown in Figures 1.3 and 1.7 are not typical of those made by the theory. For the same values of r (=1/2) and Δ (=-1+$2^{1/2}$), quantitatively different possibilities are shown in Figure 1.17 when 1e=0.91, e_w=.8 and ϕ=15.7°. We have chosen e=.91 and e_w=.8 to agree with values reported by Johnson et. al. [1990], and have chosen a relatively bumpy boundary (r=1/2 and Δ=-1+$2^{1/2}$) to replace their course sandpaper. Shown in Figures 1.18, 1.19, and 1.20 are the corresponding variations of $\bar{\nu}$, β, and $\bar{u}$ with m_t. In these figures we label points a, b, and c on the solid numerical lines whose respective flow rates are 100, 50, and 10. Similarly, we label corresponding points on the dashed approximate lines with greek letters α, β, and γ. The values of $\dot{m}$, m_t, $\bar{\nu}$, β, and $\bar{u}$ associated with each point labeled in Figures 1.17 through 1.20 are summarized in Table 1.3.

Table 1.3 Points in Figures 1.17-1.20

Point	m_t	$\dot{m}$	$\bar{v}$	β	$\bar{u}$
a	3.84	100.00	.07	57.41	34.91
a'	10.00	100.00	.35	28.71	13.90
b	2.92	50.00	.07	44.13	23.26
b'	7.35	50.00	.38	19.10	8.34
c	1.55	10.00	.07	21.09	8.73
c'	4.01	10.00	.44	9.05	2.82
α	4.15	100.00	.11	37.47	31.58
α'	10.43	100.00	.47	22.38	10.60
β	3.15	50.00	.12	27.21	10.43
β'	7.97	50.00	.47	16.87	6.93
γ	1.68	10.00	.14	12.42	7.33
γ'	4.33	10.00	.50	8.65	2.53

The most striking features of the variation of $\dot{m}$ with m_t shown in Figure 1.19 are that only one steady flow is obtained at the lowest flow rates and mass hold-ups, and that two flows are obtained at each flow rate above a critical value. Of these two flows, the more dilute occurs at the lower mass hold-up and travels at the higher velocity. Moreover, along each branch, the mass flow rate is and increasing function of mass hold-up.

Interestingly, Johnson et. al. [1990] made the same observations of their experiments. However the variations of $\bar{v}$, β, and $\bar{u}$ that they observed along the branches of a typical $\dot{m}$ versus m_t curve were quite different from those summarized in Figures 1.17 through 1.20. In particular, these figures indicate that as the flow rate increases from zero along the dilute branch of the $\dot{m}$ versus m_t curve or from the critical value above which two flows are possible along the dense branch, the depth-averaged solid fraction decreases while the depth and depth-averaged velocity both increase. Of these trends, only the variations of the two depths with increasing flow rates above the critical value agree qualitatively with those observed by Johnson et. al. [1990]. In further contrast to their experimental observations. the theory predicts that when two flows are possible at the same flow rate, the more dilute flow is the deeper of the two.

1.4 Figures

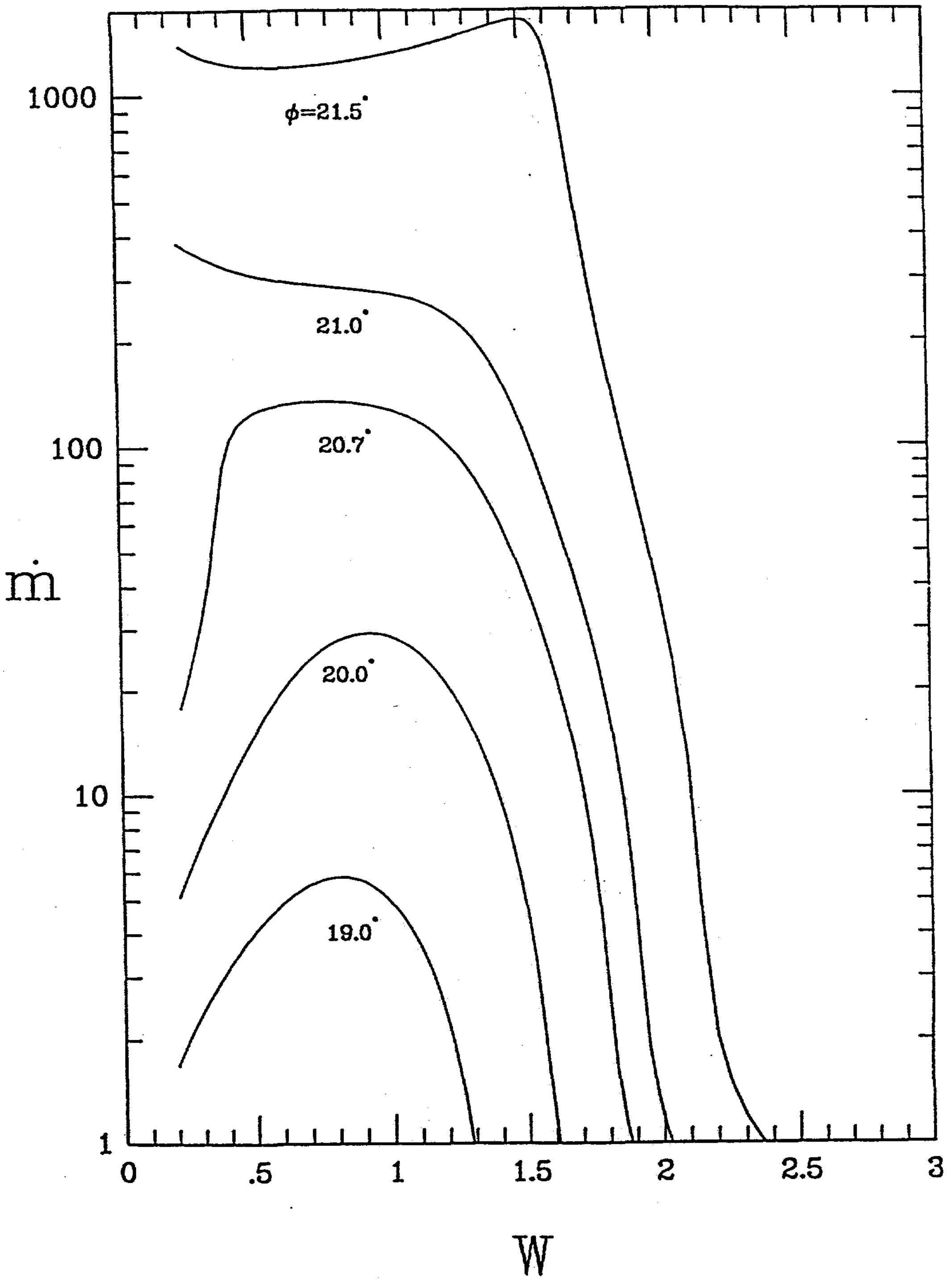

Figure 1.1: The numerical variations of ṁ with W≡w(Y=β) for φ=19.00°, 20.04°, 20.70°, 21.00°, and 21.50° when e=.8, e_w=.95, r=1/2, and $\Delta=-1+2^{1/2}$.

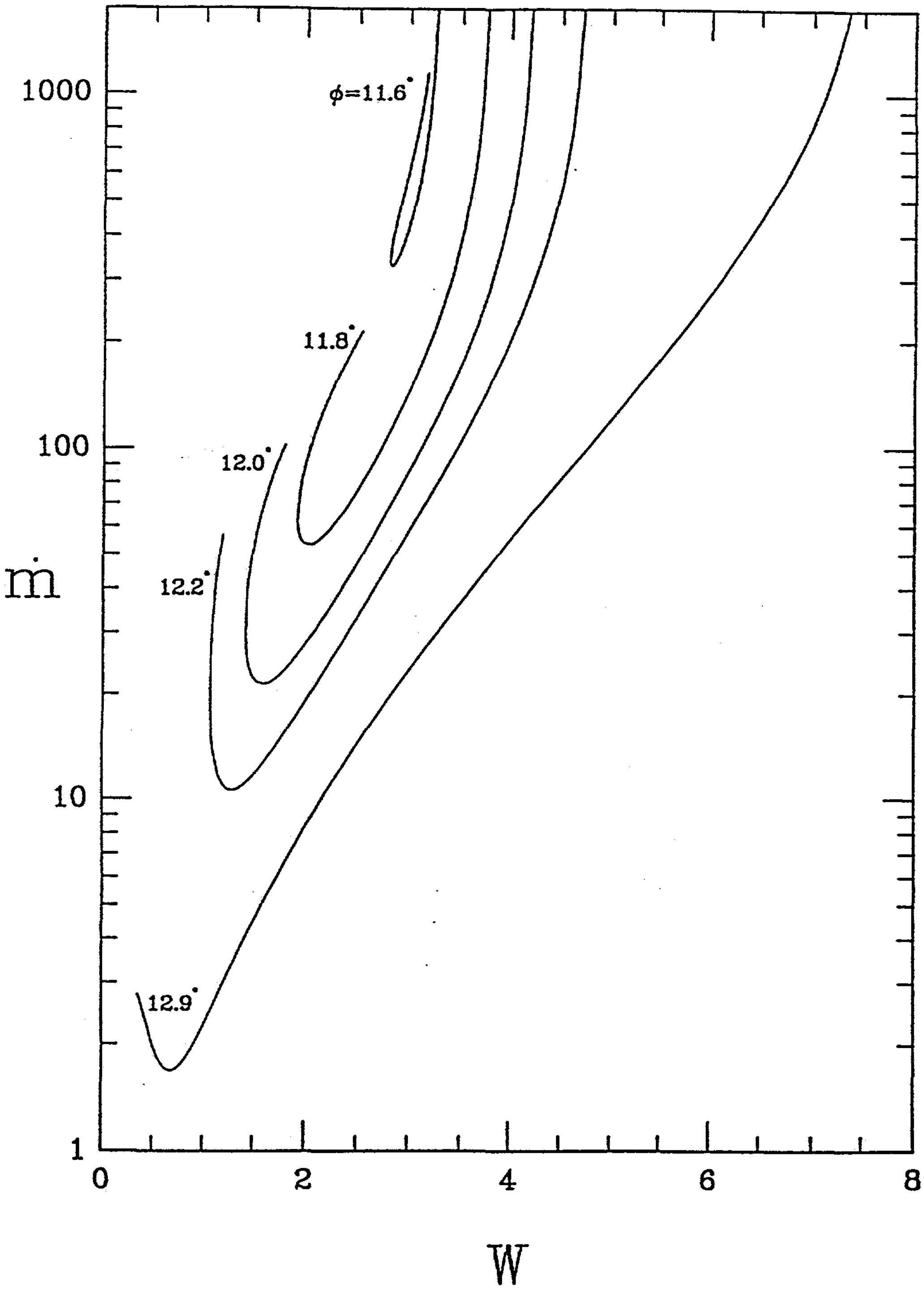

Figure 1.2: The numerical variations of ṁ with W≡w(Y=β) for ϕ=11.56°, 11.80°, 12.00°, 12.20°, and 12.90° when e=.95, e_w=.8, r=1/2, and Δ=-1+$2^{1/2}$.

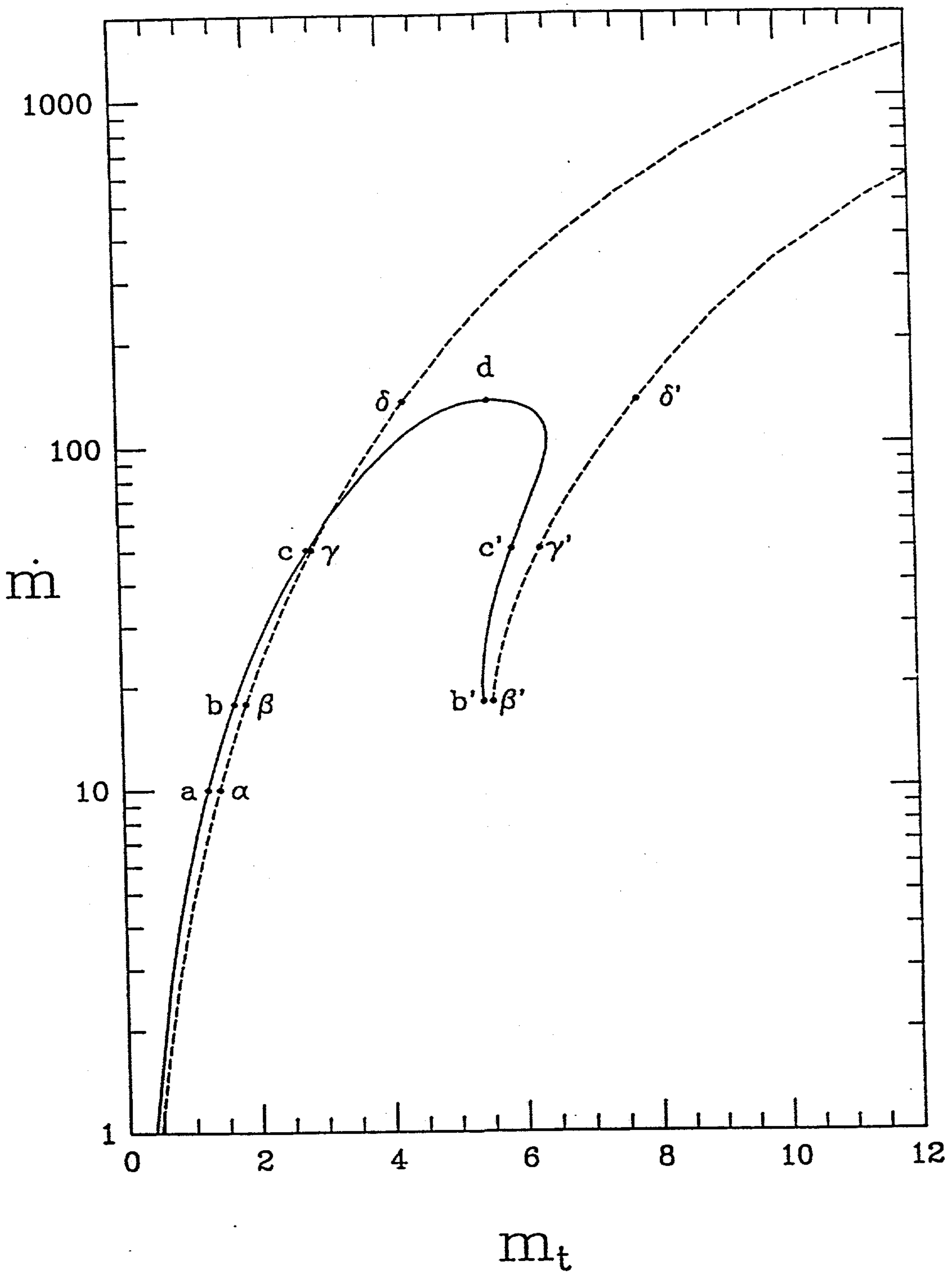

Figure 1.3: The numerical (solid) and approximate (dashed) variations of ṁ with m_t for ϕ=20.70° when e=.8, e_w=.95, r=1/2, and $\Delta=-1+2^{1/2}$. Numerical values of labeled points given in Table 1.1.

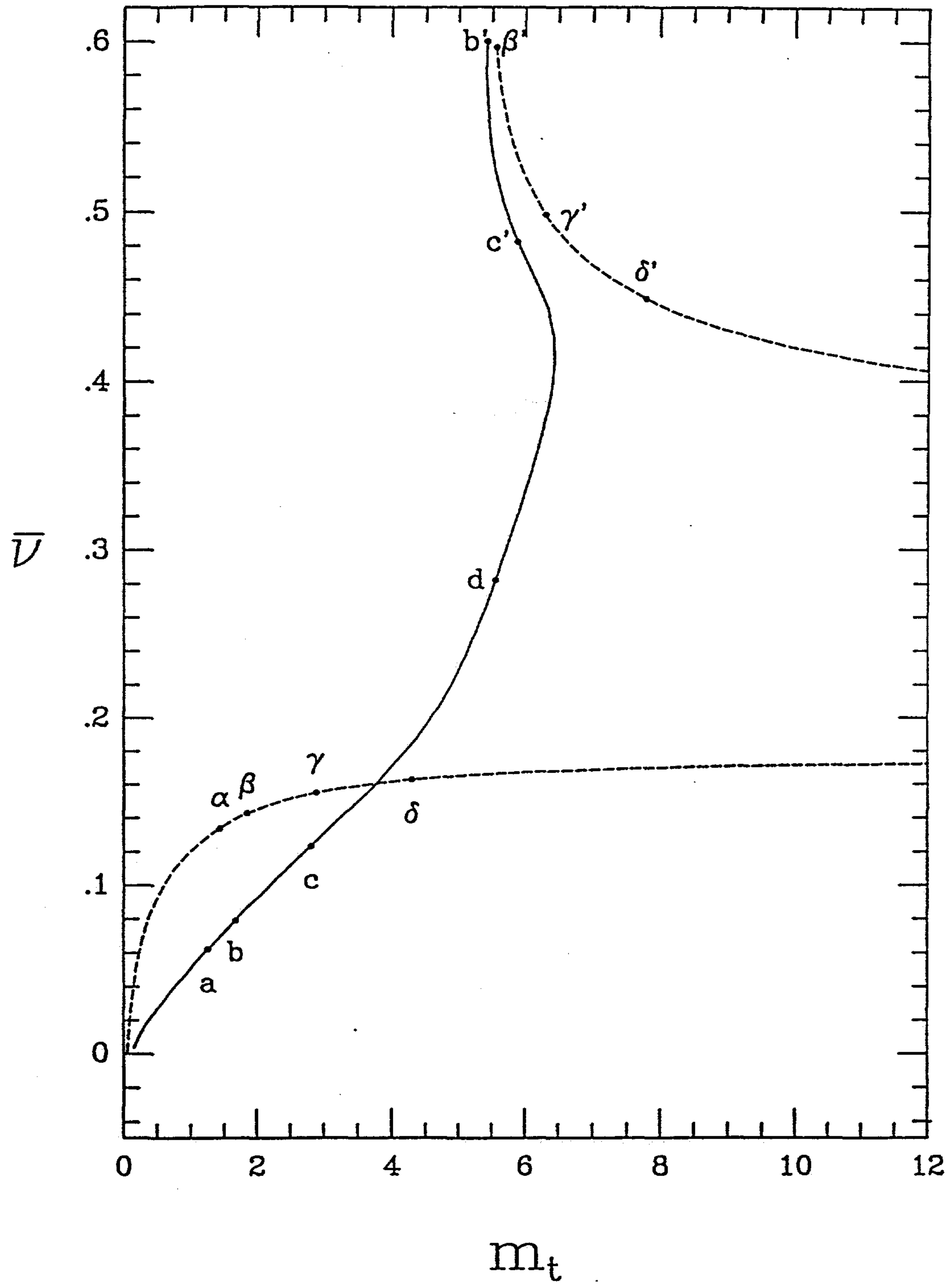

Figure 1.4: The numerical (solid) and approximate (dashed)variations of $\bar{\nu}$ with m_t for ϕ=20.70° when e=.8, e_w=.95, r=1/2, and $\Delta=-1+2^{1/2}$. Numerical values of labeled points given in Table 1.1.

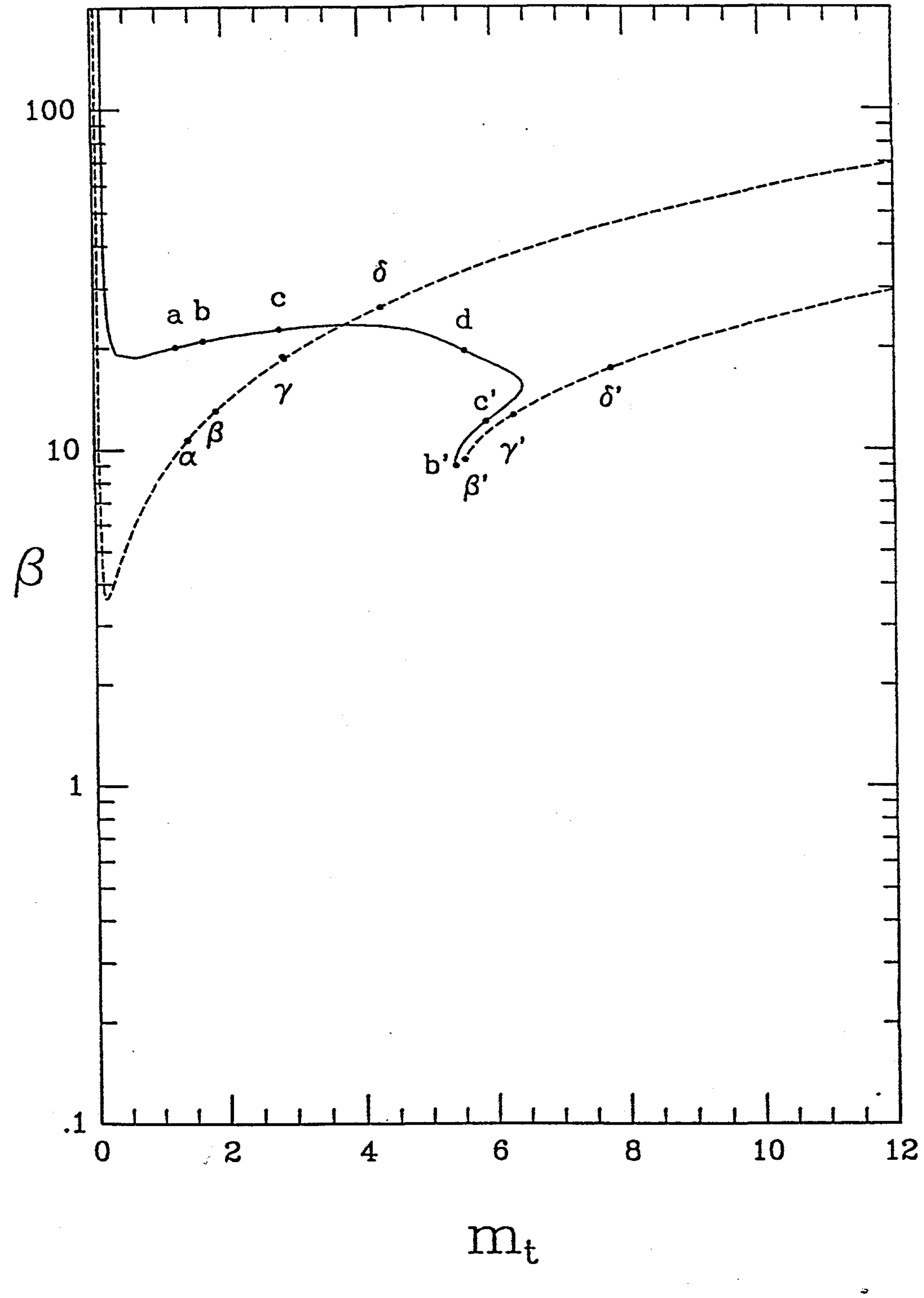

Figure 1.5: The numerical (solid) and approximate (dashed)variations of β with m_t for ϕ=20.70° when e=.8, e_w=.95, r=1/2, and $\Delta=-1+2^{1/2}$. Numerical values of labeled points given in Table 1.1.

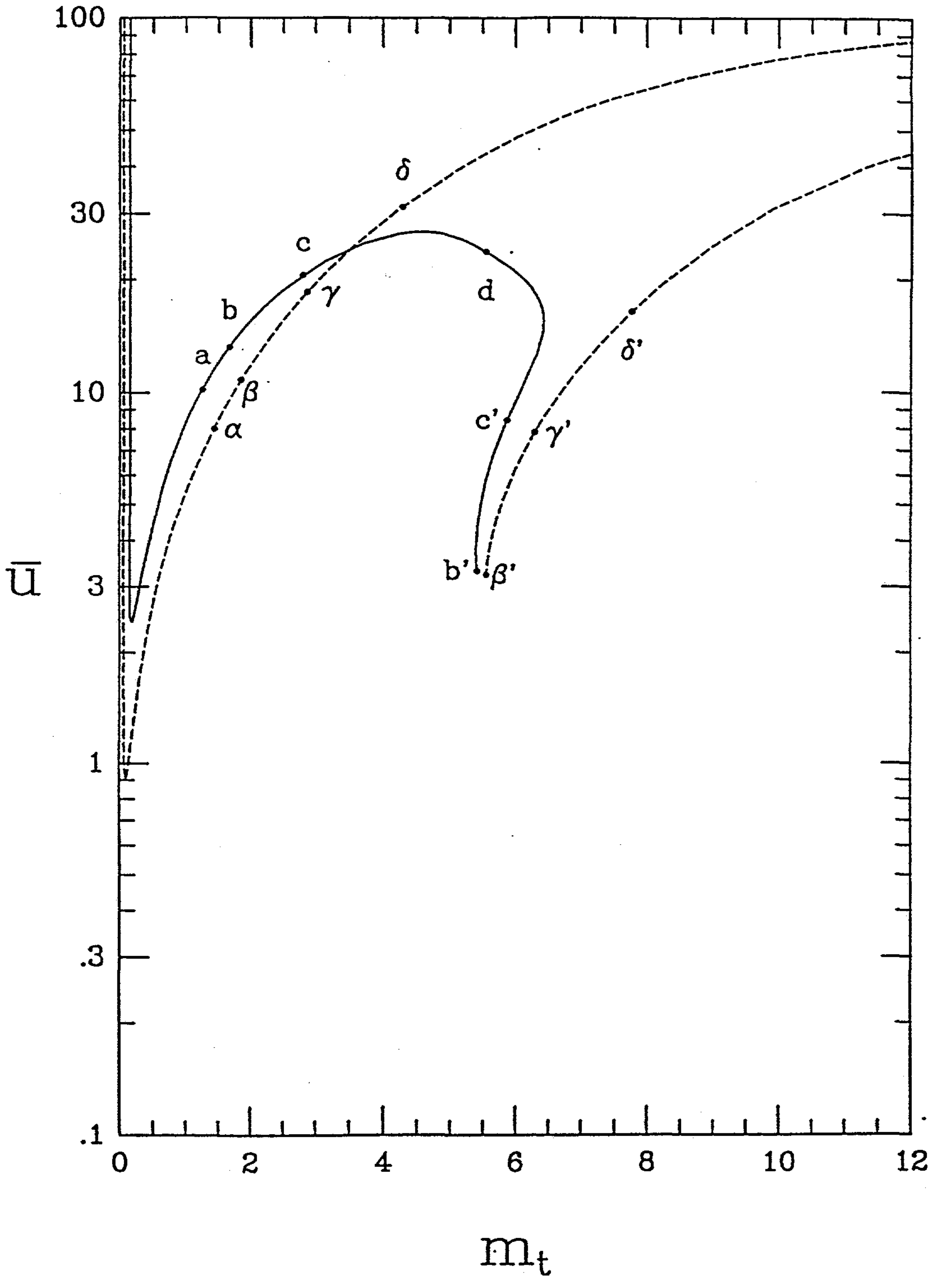

Figure 1.6: The numerical (solid) and approximate (dashed)variations of ū with m_t for $\phi=20.70°$ when e=.8, $e_w=.95$, r=1/2, and $\Delta=-1+2^{1/2}$. Numerical values of labeled points given in Table 1.1.

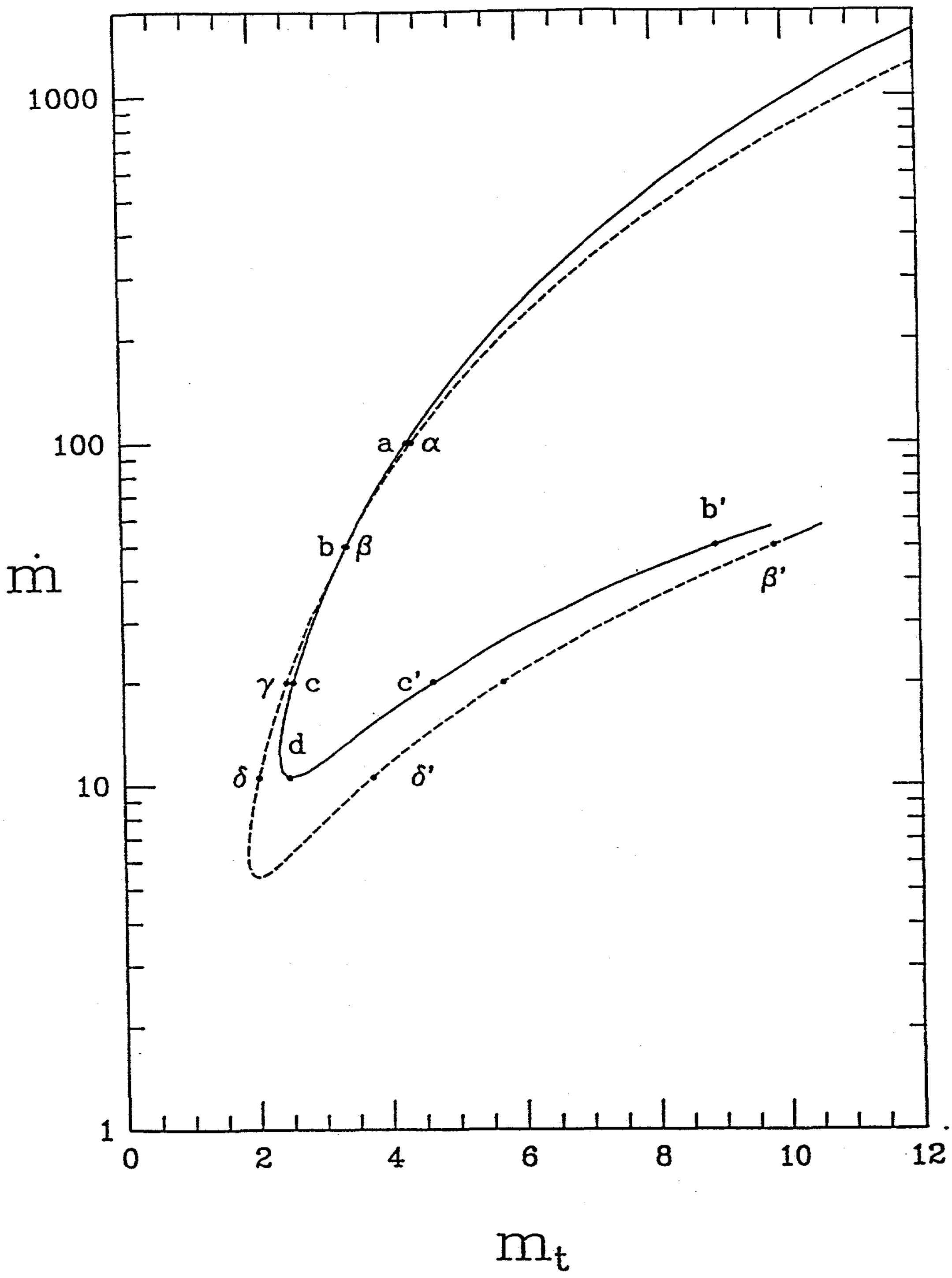

Figure 1.7: The numerical (solid) and approximate (dashed) variations of ṁ with m_t for ϕ=12.20° when e=.95, e_w=.8, r=1/2, and $\Delta=-1+2^{1/2}$. Numerical values of labeled points given in Table 1.2.

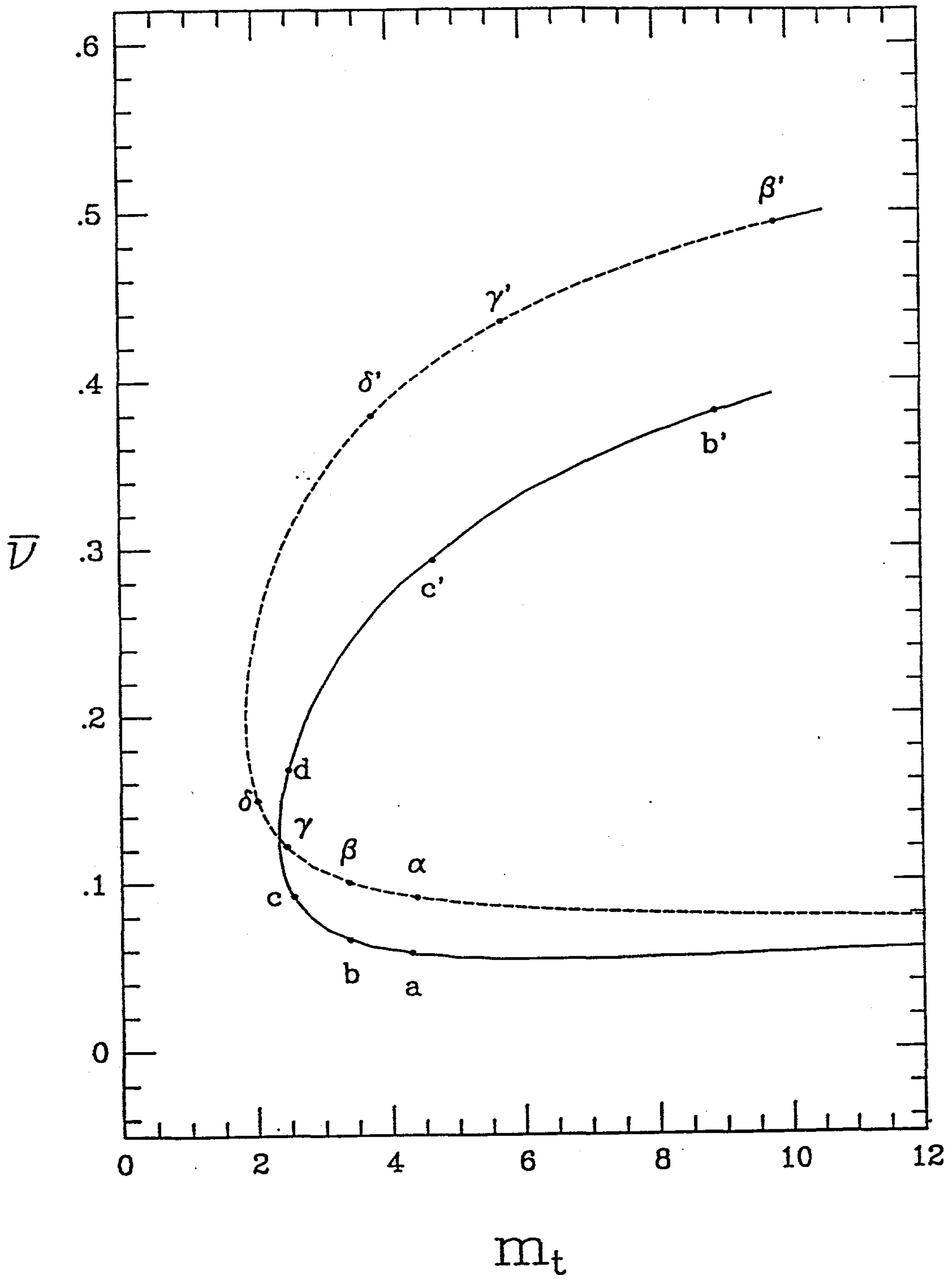

Figure 1.8: The numerical (solid) and approximate (dashed) variations of $\bar{v}$ with m_t for ϕ=12.20° when e=.95, e_w=.8, r=1/2, and $\Delta=-1+2^{1/2}$. Numerical values of labeled points given in Table 1.2.

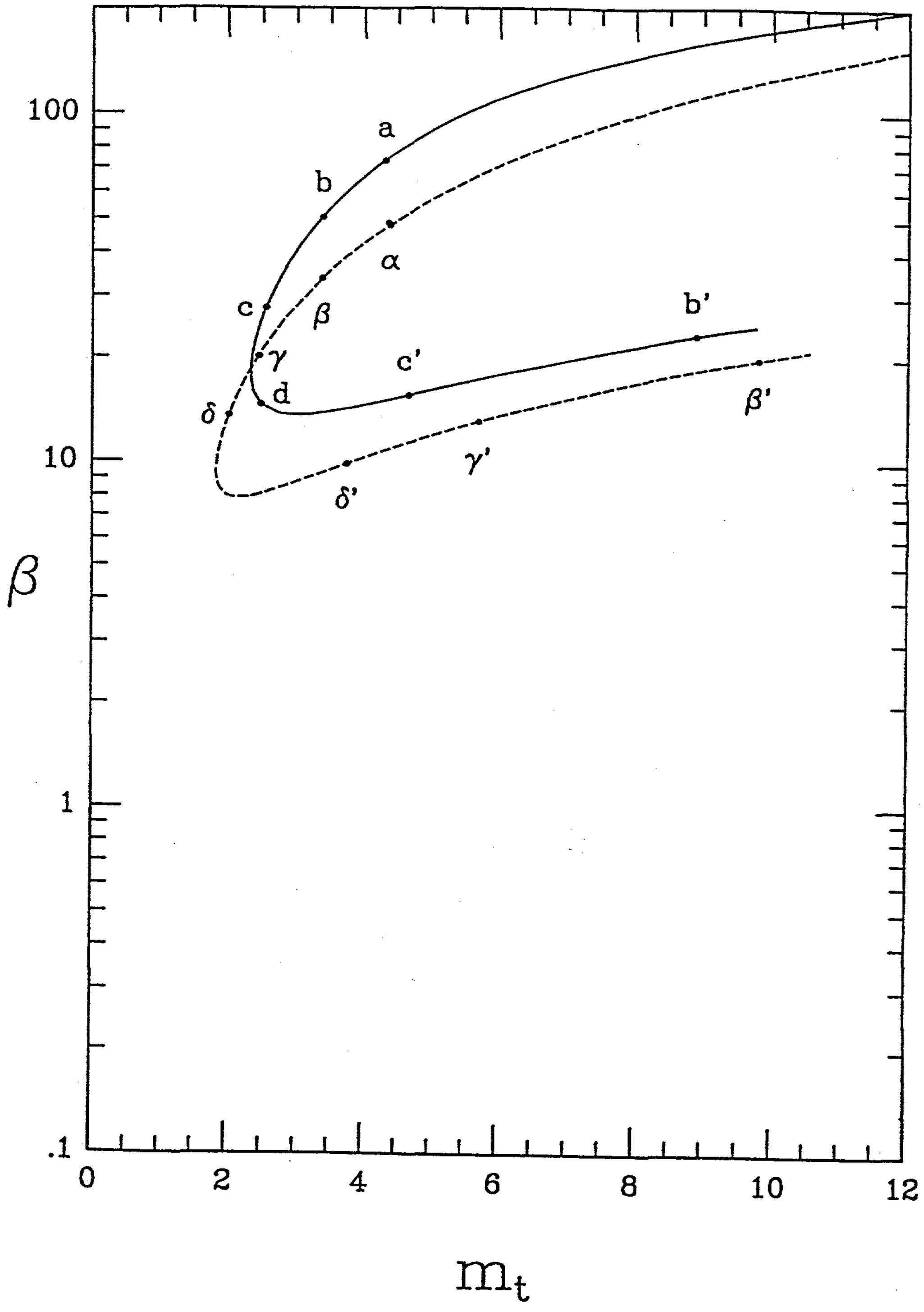

Figure 1.9: The numerical (solid) and approximate (dashed) variations of β with m_t for ϕ=12.20° when e=.95, e_w=.8, r=1/2, and $\Delta=-1+2^{1/2}$. Numerical values of labeled points given in Table 1.2.

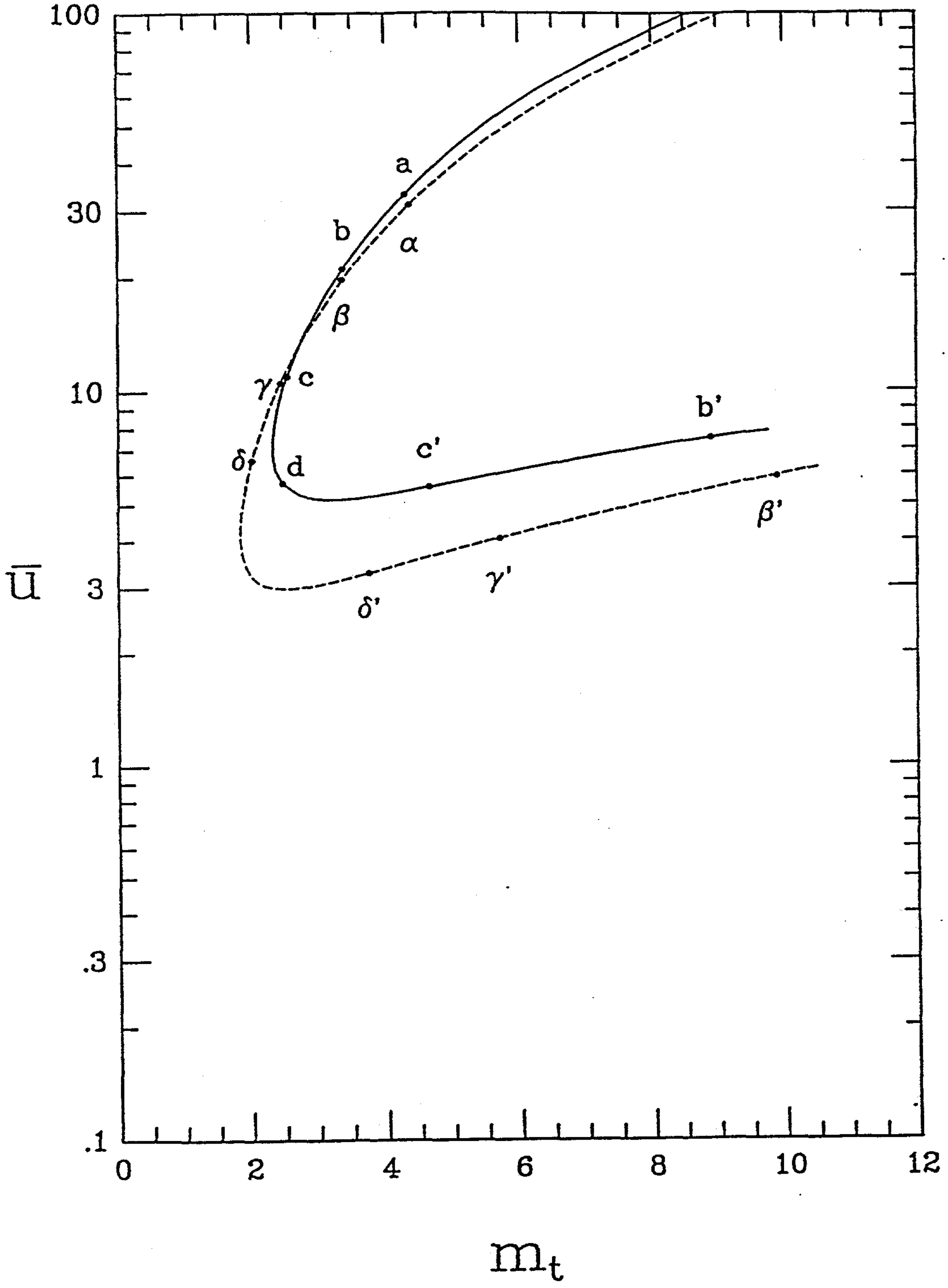

Figure 1.10: The numerical (solid) and approximate (dashed) variations of ũ with m_t for $\phi=12.20°$ when $e=.95$, $e_w=.8$, $r=1/2$, and $\Delta=-1+2^{1/2}$. Numerical values of labeled points given in Table 1.2.

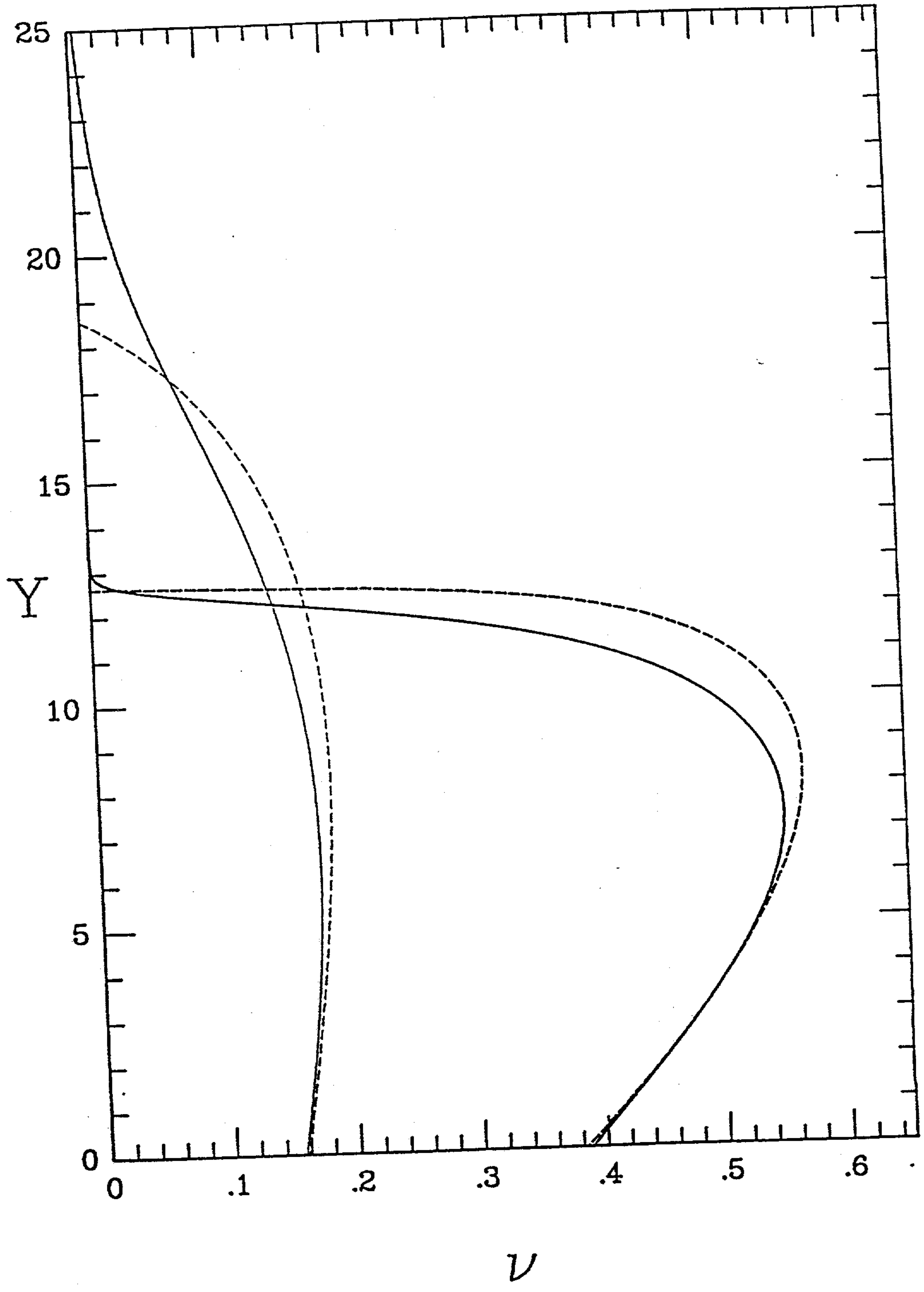

Figure 1.11: The numerical (dark and light solid) and approximate (dark and light dashed) variations of ν with Y for ϕ=20.70° and ṁ=50 when e=.8, e_w=.95, r=1/2, and $\Delta=-1+2^{1/2}$

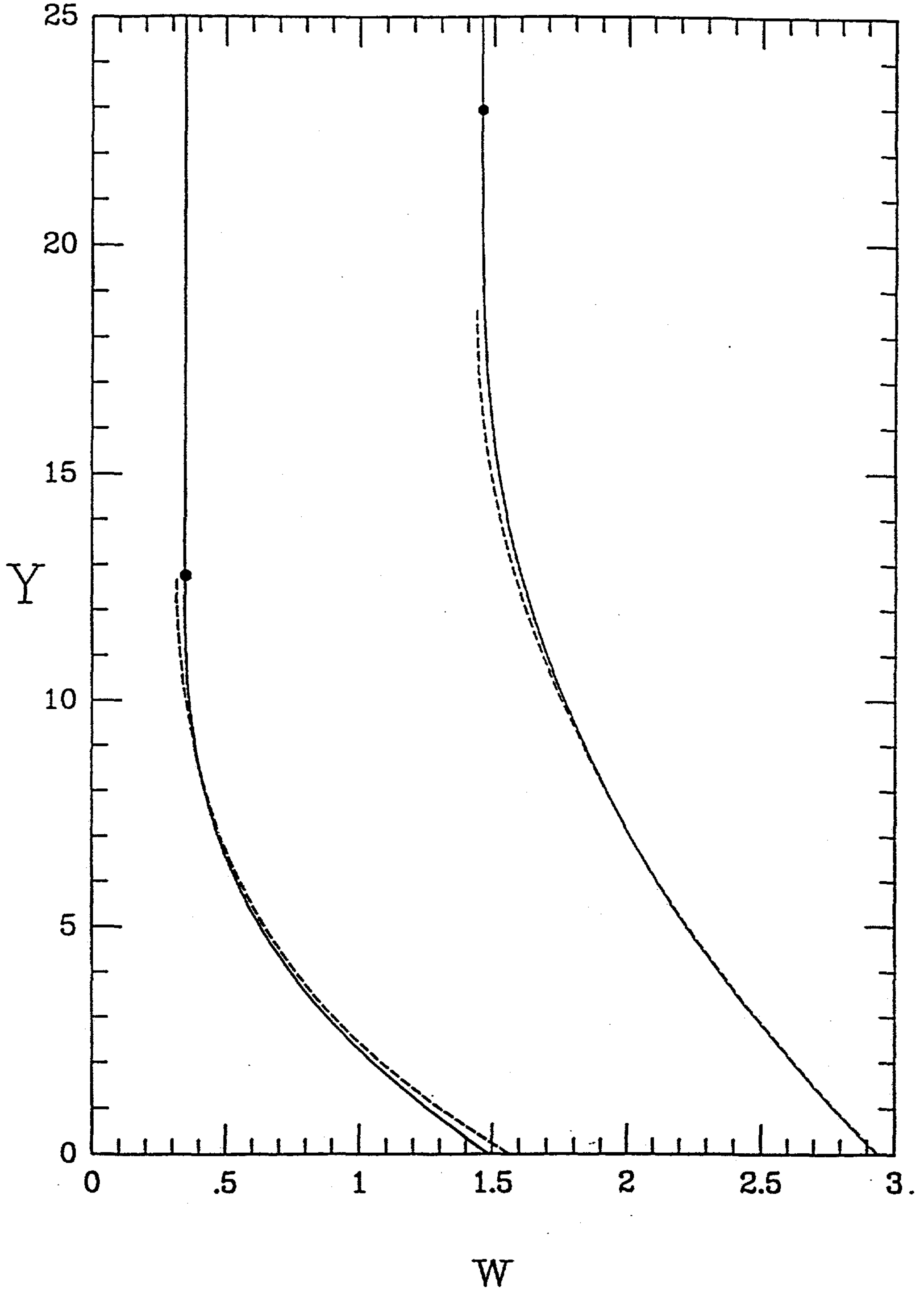

Figure 1.12: The numerical (dark and light solid) andapproximate (dark and light dashed) variations of w with Y for ϕ=20.70° and $\dot{m}$=50 when e=.8, e_w=.95, r=1/2, and Δ=-1+$2^{1/2}$. Solid dots indicate where ν=.01.

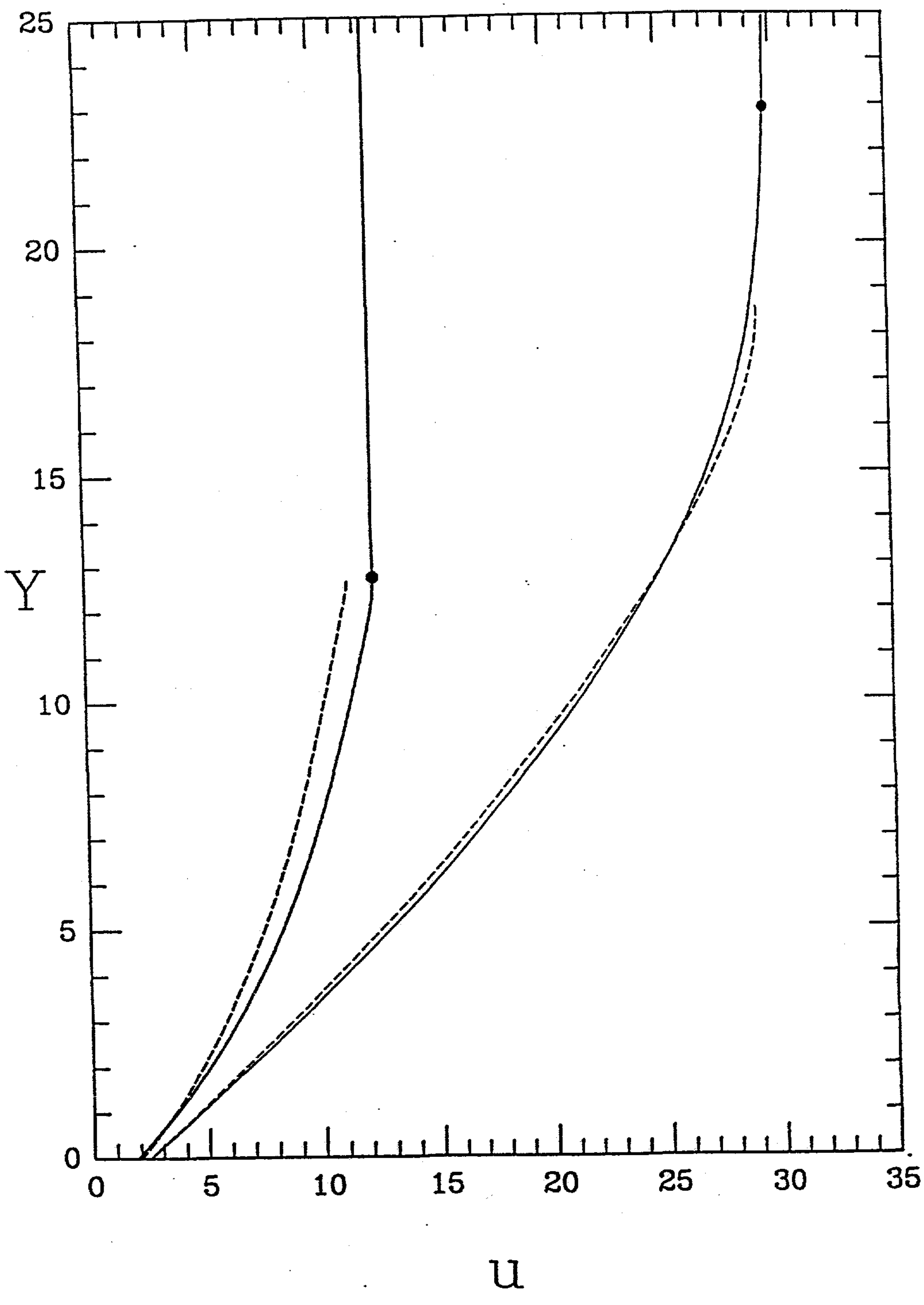

Figure 1.13: The numerical (dark and light solid) and approximate (dark and light dashed) variations of u with Y for ϕ=20.70° and \dot m=50 when e=.8, e_w=.95, r=1/2, and Δ=-1+$2^{1/2}$. Solid dots indicate where ν=.01.

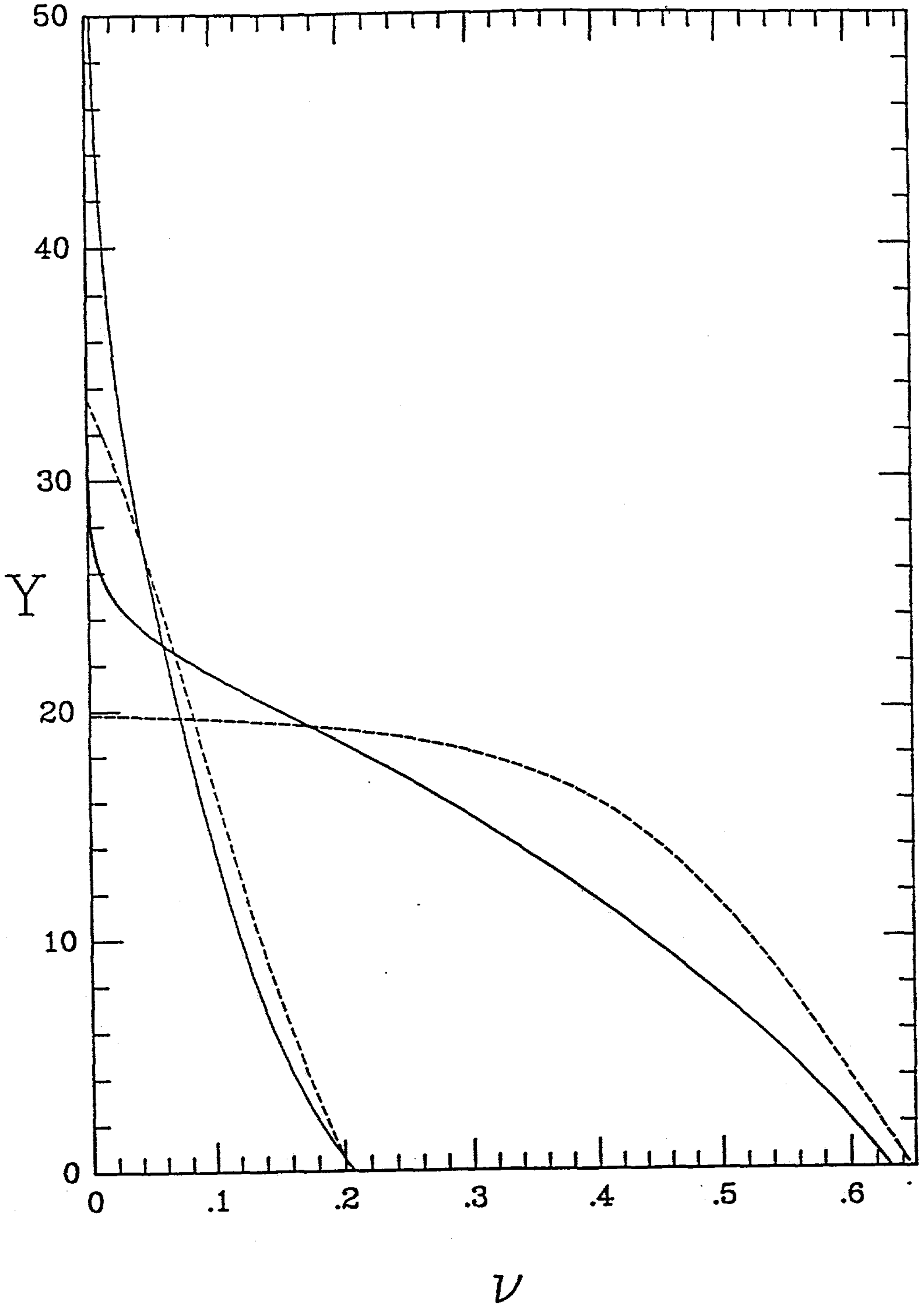

Figure 1.14: The numerical (dark and light solid) and approximate (dark and light dashed) variations of ν with Y for ϕ=12.20° and ṁ=50 when e=.95, e_w=.8, r=1/2, and $\Delta=-1+2^{1/2}$.

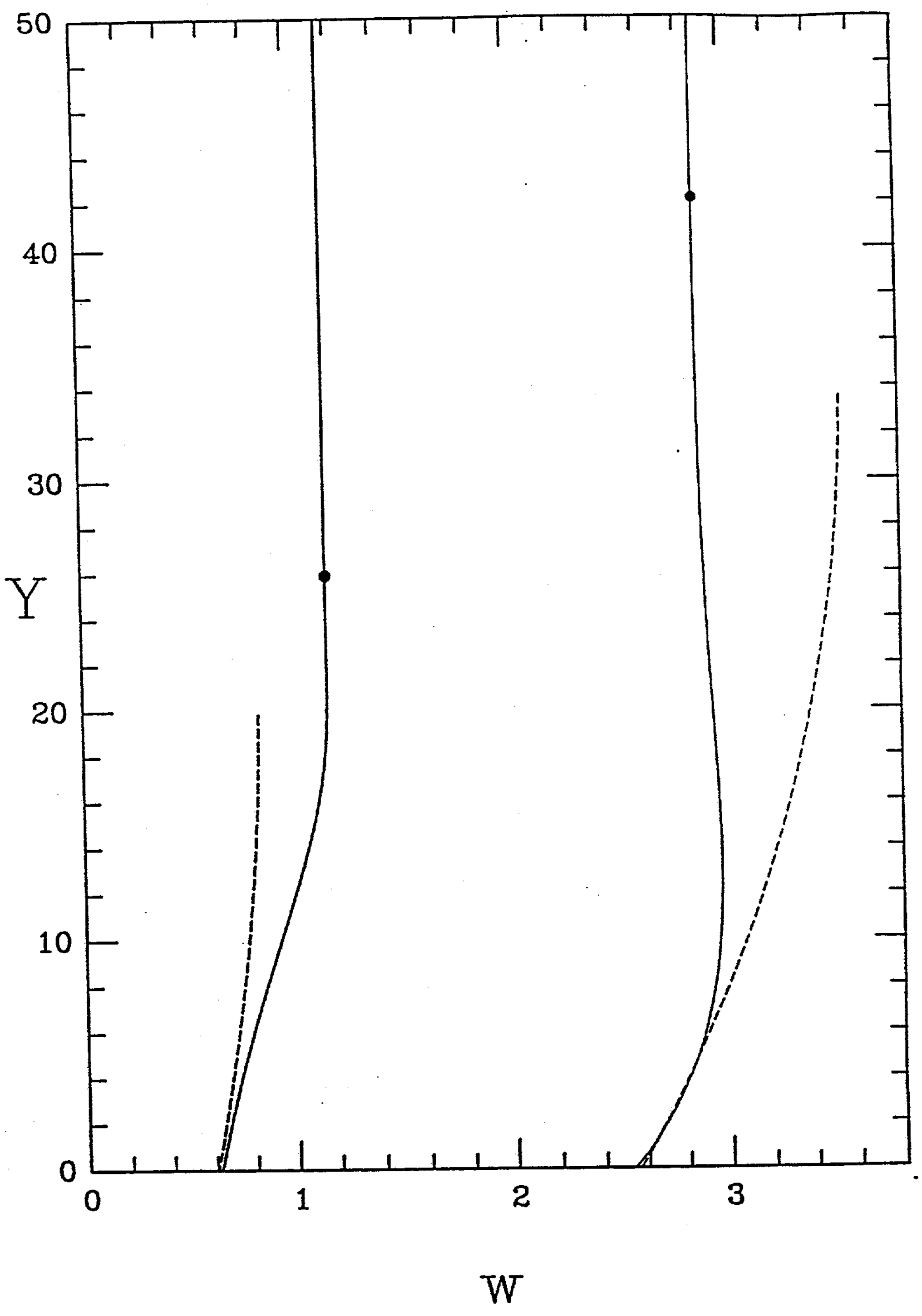

Figure 1.15: The numerical (dark and light solid) and approximate (dark and light dashed) variations of w with Y for ϕ=12.20° and \dot m=50 when e=.95, e_w=.8, r=1/2, and $\Delta=-1+2^{1/2}$. Solid dots indicate where ν=.01.

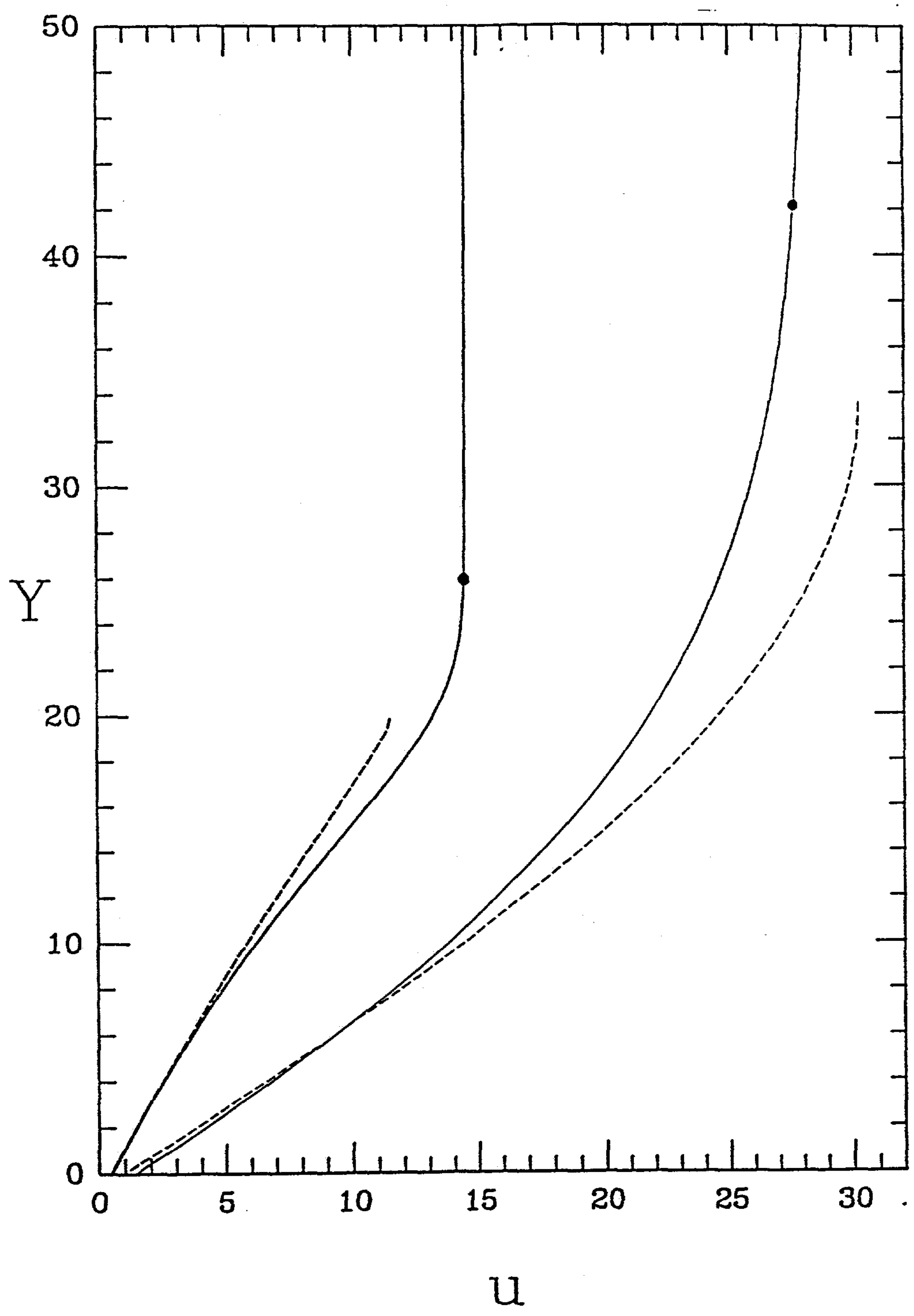

Figure 1.16: The numerical (dark and light solid) andapproximate (dark and light dashed) variations of u with Y for ϕ=12.20° and $\dot{m}$=50 when e=.95, e_w=.8, r=1/2, and $\Delta=-1+2^{1/2}$. Solid dots indicate where ν=.01.

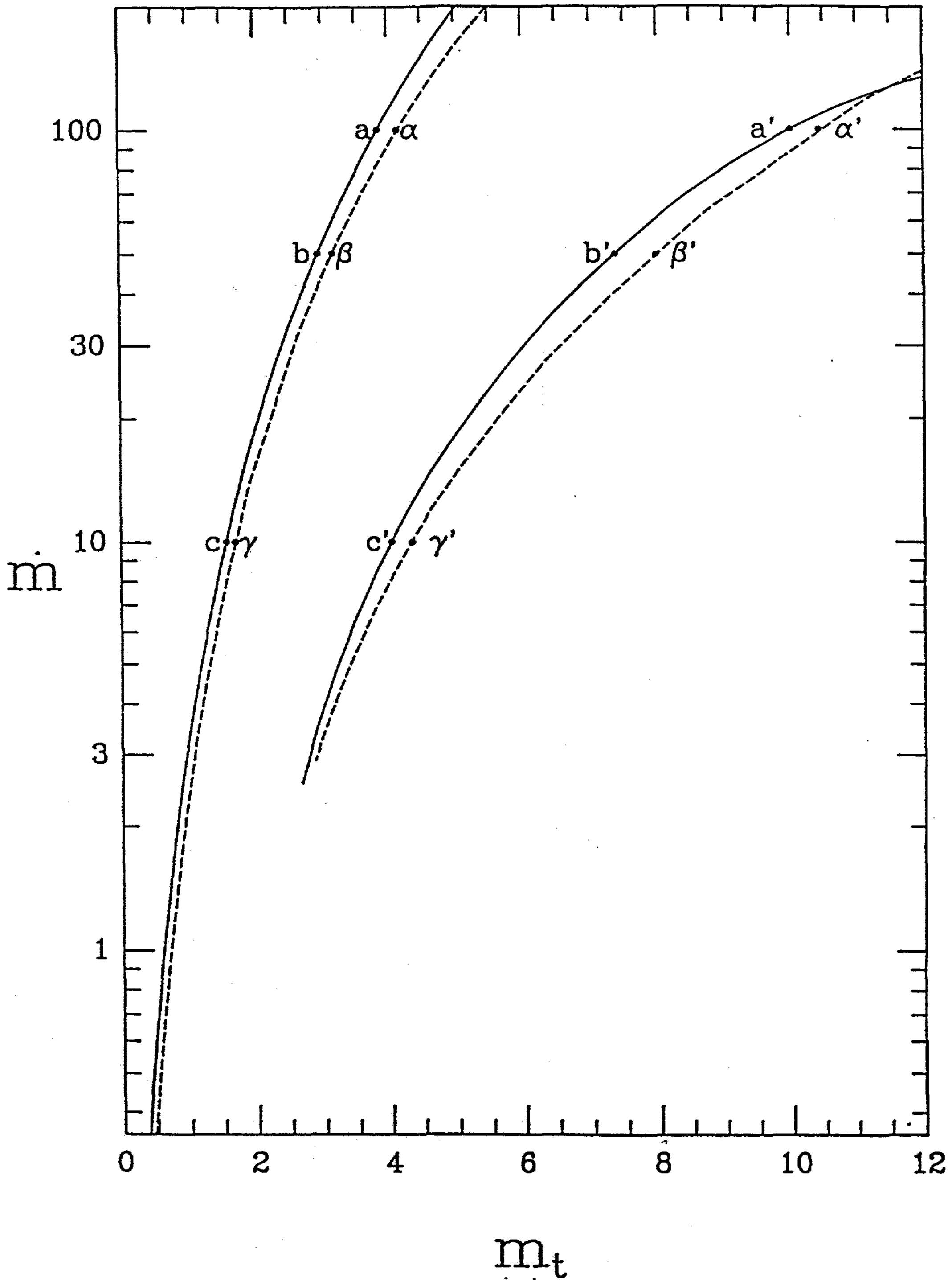

Figure 1.17: The numerical (solid) and approximate (dashed) variations of ṁ with m_t for ϕ=15.70° when e=.91, e_w=.8, r=1/2, and $\Delta=-1+2^{1/2}$. Numerical values of labeled points given in Table 1.3.

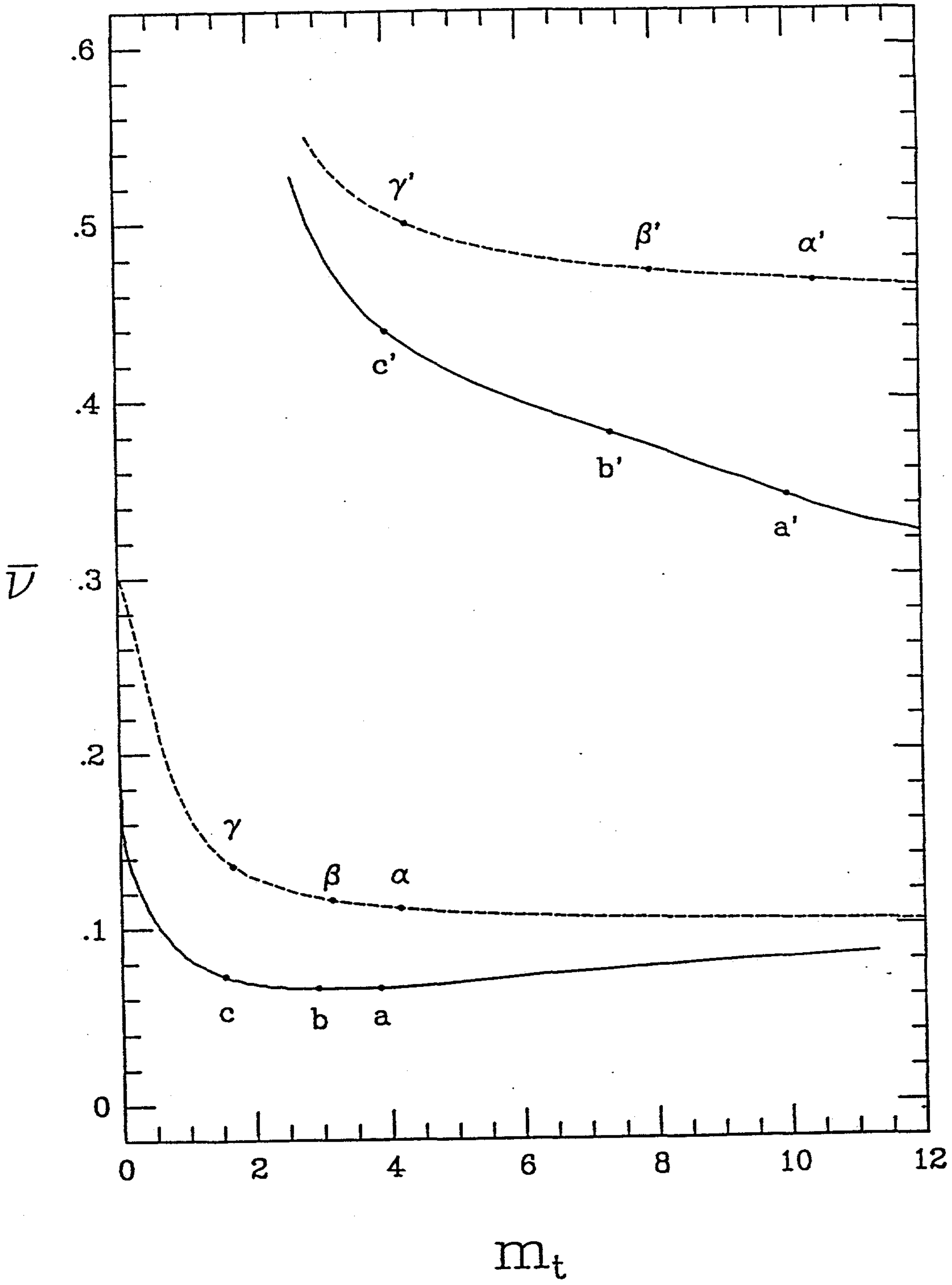

Figure 1.18: The numerical (solid) and approximate (dashed) variations of $\bar{v}$ with m_t for ϕ=15.70° when e=.91, e_w=.8, r=1/2, and $\Delta=-1+2^{1/2}$. Numerical values of labeled points given in Table 1.3.

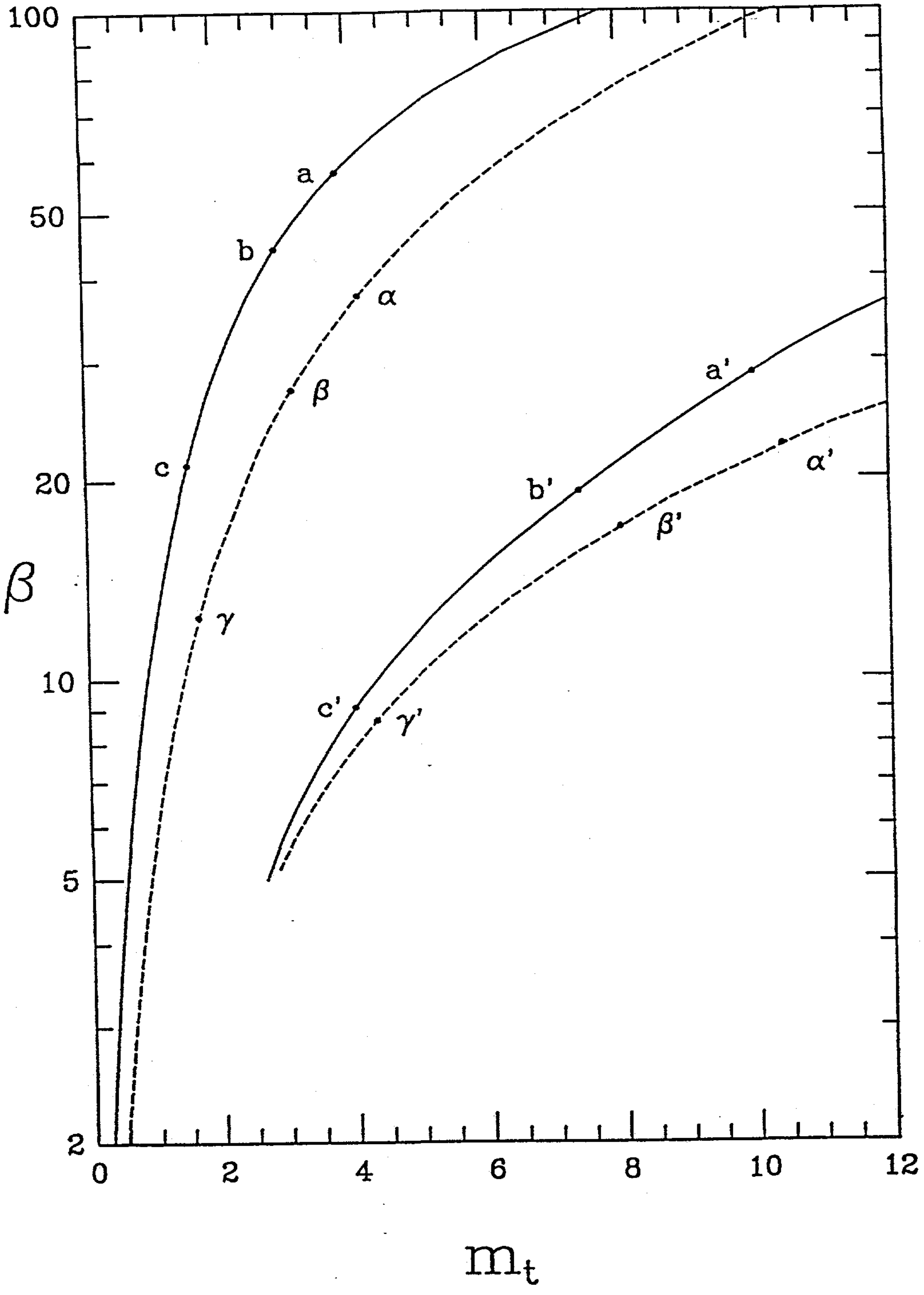

Figure 1.19: The numerical (solid) and approximate (dashed) variations of β with m_t for ϕ=15.70° when e=.91, e_w=.8, r=1/2, and $\Delta=-1+2^{1/2}$. Numerical values of labeled points given in Table 1.3.

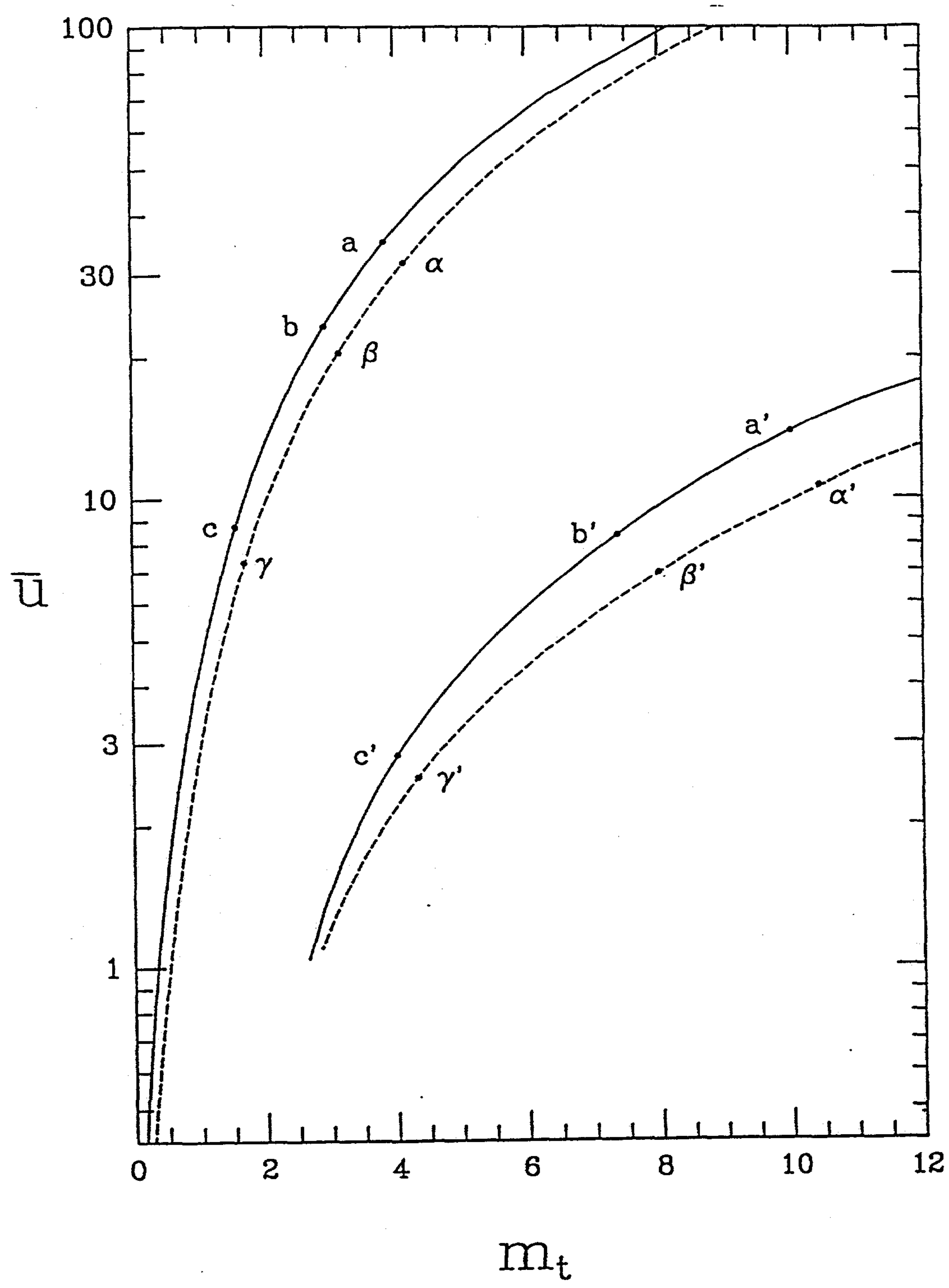

Figure 1.20: The numerical (solid) and approximate (dashed) variations of ū with m_t for ϕ=15.70° when e=.91, e_w=.8, r=1/2, and $\Delta=-1+2^{1/2}$. Numerical values of labeled points given in Table 1.3.

2. GRAVITY-DRIVEN FLOWS OF SMOOTH, INELASTIC SPHERES DOWN BUMPY INCLINES: FORMULATION

In this section, we employ the kinetic theory for highly inelastic spheres to analyze steady, fully developed, gravity-driven flows of identical, smooth, highly inelastic spheres down bumpy inclines. As in the general theory, we treat the solid fraction, mean velocity, and components of the full second moment of fluctuation velocity as mean fields. In addition to the balance equations for mass and momentum, we treat the balance of the full second moment of fluctuation velocity as an equation that must be satisfied by the mean fields. However, in order to simplify the resulting boundary value problem, we retain fluxes of second moments in its isotropic piece only. The constitutive relations for the stresses and and collisional source of second moment depend explicitly on the second moment of fluctuation velocity, and the constitutive relation for the energy flux depends on gradients of granular temperature, solid fraction, and components of the second moment. We obtain numerical solutions that are free of stress and energy flux at the tops of the flows, satisfy momentum and energy balances at the bumpy base, and are most easily parameterized in terms of the granular temperature at the tops of the flows. To each such temperature there corresponds a value of mass hold-up and mass flow rate. For fixed coefficients of restitution, boundary bumpiness, and angle of inclination, we calculate the variation of mass flow rate with mass hold-up, and for a prescribed value of mass hold-up we calculate the profiles of solid fraction, mean velocity, normal components of the second moment, and normal stresses.

2.1 Balance Equations and Constitutive Relations

We are concerned here with steady, fully developed, gravity-driven flows of identical, smooth, highly inelastic spheres down bumpy inclines. The diameter of each sphere is σ, the mass density of each is ρ_p, and the coefficient of restitution between them is e. In what follows, e need not be close to unity. The vertical acceleration due to gravity is g, and the angle between the incline and the the horizontal is ϕ. We introduce an x_1-x_2-x_3 Cartesian coordinate system such that x_1 measures distance along the incline parallel to the flows, and x_2 measures distance above the incline perpendicular to the the flows. The flows are infinitely extended in the x_1- and x_3-directions.

The mean fields of interest in these granular flows are the solid fraction ν, the only non-zero velocity component u_1, the granular temperature T, and the components A_{11}, A_{22}, A_{33}, and A_{12}, of the *deviatoric* part of the second moment of particle fluctuation velocity. Their dimensionless counterparts ν, $u \equiv u_1/(\sigma g)^{1/2}$, $\tau \equiv T/\sigma g$, $a_{11} \equiv A_{11}/\sigma g$, $a_{22} \equiv A_{22}/\sigma g$,

$a_{33} \equiv A_{33}/\sigma g$, and $a_{12} \equiv A_{12}/\sigma g$ depend on the dimensionless coordinate $y \equiv x_2/\sigma$ only. Their variations with y are governed by the x_1- and x_2-components of the balance of momentum, the balance of energy, and the x_1-x_1, x_2-x_2, x_3-x_3 and x_1-x_2 components of the balance of second moment.

Under these circumstances, the balance of mass is satisfied identically. If P_{ij} are the components of the pressure tensor, then in terms of their dimensionless counterparts $p_{ij} \equiv P_{ij}/\rho_p \sigma g$, the x_1- and x_2-components of the balance of momentum are,

$$p_{12}' = \nu \sin\phi \quad , \tag{1}$$

and

$$p_{22}' = -\nu \cos\phi \quad , \tag{2}$$

where primes denote differentiation with respect to y. The x_3-component of the balance of momentum demonstrates that p_{32} does not vary with y. The balance of energy is the isotropic part of the balance of the full second moment of fluctuation velocity. If Q_2 is the x_2-component of the energy flux, Γ is the rate of energy dissipation due to inelastic collisions, and their dimensionless counterparts are $q \equiv 2Q_2/\rho_p(\sigma g)^{3/2}$ and $\gamma \equiv -2\Gamma/\rho_p \sigma^{1/2} g^{3/2}$, then the balance of energy is,

$$q' = \gamma - 2p_{12}u' \quad . \tag{3}$$

The remaining equations are obtained from the deviatoric part of the balance of full second moment. In addition to the components P_{ij} of the pressure tensor, these equations involve the components Q_{ijk} and χ_{ij} of the flux and collisional source of the deviatoric part of the second moment. If the spatial gradients of Q_{ijk} are small compared to χ_{ij}, then, in terms of the dimensionless source components $\gamma_{ij} \equiv \chi_{ij}/\rho_p \sigma^{1/2} g^{3/2}$, the resulting approximate equations for a_{11}, a_{22}, and a_{12} are the x_1-x_1 deviatoric component of the balance of second moment,

$$\frac{4}{3} p_{12}\, u' = \gamma_{11} \quad ; \tag{4}$$

the x_2-x_2 deviatoric component of the balance of second moment,

$$\frac{-2}{3} p_{12}\, u' = \gamma_{22} \quad ; \tag{5}$$

and the x_1-x_2 component of the balance of second moment,

$$p_{22}\, u' = \gamma_{12} \quad . \tag{6}$$

The x_3-x_3 deviatoric component of the second moment equation determines a_{33}, and to within a minus sign is given by the sum of equations (4) and (5).

In what follows, we employ the constitutive theory derived by Richman and Martin [1993]. The constitutive relation for the shear stress p_{12} is given in terms of the solid fraction ν, the granular temperature τ, and the second moment component a_{12} by,

$$p_{12} = -2(1+e)\nu G\tau\left[\frac{2}{5\sqrt{\pi\tau}}\, u' - H\,\frac{a_{12}}{\tau}\right] \quad , \tag{7}$$

in which $G(\nu)$ is equal to $\nu(2-\nu)/2(1-\nu)^3$ and $H(G)$ is equal to $2[1+5/4(1+e)G]/5$. The normal pressure p_{11} is given in terms of ν, τ, and the deviatoric component a_{11} of second moment by,

$$p_{11} = 2(1+e)\nu G\tau\left[F + H\,\frac{a_{11}}{\tau}\right] \quad , \tag{8}$$

in which $F(G)$ is equal to $[1+1/2(1+e)G]$. Similarly, the remaining normal pressures p_{22} and p_{33} are given by,

$$p_{22} = 2(1+e)\nu G\tau\left[F + H\,\frac{a_{22}}{\tau}\right] \quad , \tag{9}$$

and

$$p_{33} = 2(1+e)\nu G\tau\left[F + H\,\frac{a_{33}}{\tau}\right] \quad . \tag{10}$$

Differences between the normal stresses result from corresponding differences between a_{11}, a_{22}, and a_{33}.

The energy flux q is related to gradients of τ, a_{22}, and ν according to the relation,

$$q = \frac{-4(1+e)\nu G\tau^{1/2}}{\pi^{1/2}}\left(\kappa\tau' + \lambda\tau\nu' + \eta\, a_{22}'\right) \quad , \tag{11}$$

in which the coefficients $\kappa(\nu, e)$, $\lambda(\nu, e)$, and $\eta(\nu, e)$ are given by,

$$\kappa = \left\{ 1 + \frac{9\pi(1+e)(2e-1)}{4(49-33e)} \left[1 + \frac{5}{3(1+e)^2(2e-1)G} \right] \left[1 + \frac{5}{6(1+e)G} \right] \right] \right\} \quad , \tag{12}$$

$$\lambda = \frac{-9\pi e(1-e)}{4(49-33e)} \frac{d(\ln \nu G)}{d\nu} \left[1 + \frac{5}{6(1+e)G} \right] \quad , \tag{13}$$

and

$$\eta = \frac{2}{5} \left\{ 1 + \frac{25\pi(3e+1)(\beta+\alpha)}{24(3-e)(49-33e)} \left[1 + \frac{1}{(1+e)(\beta+\alpha)G} \right] \left[1 + \frac{5}{6(1+e)G} \right] \right.$$

$$\left. + \frac{5\pi\xi}{24(3-e)} \left[1 + \frac{1}{(1+e)\xi G} \right] \left[1 + \frac{5}{6(1+e)G} \right] \right\} \quad , \tag{14}$$

where $\beta \equiv (49-33e)[-6(1+e)/5+4(1+e)^2/3]/14(3e+1)$, $\alpha \equiv [-4/5-9(1+e)/5+2(1+e)^2/3]$, and $\xi \equiv [-4/5+6(1+e)/5+4(1+e)^2/21]$. If gradients of a_{22} are ignored and e is set equal to 1, then expression (11) reduces to the expression for the energy flux in assemblies of nearly elastic spheres obtained by Jenkins and Richman [1985].

The remaining constitutive quantity is the collisional source of second moment of fluctuation velocity. In it, we retain terms linear in a_{11}, a_{22}, a_{33}, a_{12}, and u'. In addition, we retain just those nonlinear terms that guarantee that, in the tensoral form of the balance of of second moment, the collisional contribution to the stress is multiplied only by the rate of strain. In this manner, the isotropic piece of the source of second moment is approximated by,

$$\gamma = \frac{-24\nu G(1-e^2)\tau^{3/2}}{\pi^{1/2}} \quad . \tag{15}$$

The corresponding result obtained by Jenkins and Richman [1985] may be obtained by replacing $(1-e^2)$ by $2(1-e)$ in expression (15). The deviatoric parts of the x_1-x_1 and x_2-x_2 components of the source of second moment are given in terms of ν, τ, a_{11}, a_{22}, a_{12}, p_{12}, and u' by the constitutive relations,

$$\gamma_{11} = \frac{-24\nu G(1+e)(3-e)\tau^{3/2}}{5\pi^{1/2}} \frac{a_{11}}{\tau} + (p_{12} - \nu a_{12})u' \quad , \tag{16}$$

and

$$\gamma_{22} = \frac{-24\nu G(1+e)(3-e)\tau^{3/2}}{5\pi^{1/2}} \frac{a_{22}}{\tau} - (p_{12} - \nu a_{12})u' \quad , \tag{17}$$

where p_{12} is given by equation (7). Similarly, the x_1-x_2 component of the source of second moment is,

$$\gamma_{12} = \frac{-24\nu G(1+e)\tau^{3/2}}{5}\left\{\frac{(3-e)}{\pi^{1/2}}\frac{a_{12}}{\tau} - \frac{(2-e)}{4}\frac{u'}{\tau^{1/2}}\right\} + [(p_{22}-p_{11}) - \nu(a_{22}-a_{11})]\frac{u'}{2}\ , \qquad (18)$$

where p_{11} and p_{22} are given by equations (8) and (9). Constitutive relations (16), (17), and (18) have no counterparts in the theory of Jenkins and Richman [1985] for nearly elastic spheres.

In order to reduce the number of equations in the governing system, we employ constitutive relation (16) to eliminate γ_{11} from balance (4) to obtain,

$$\frac{a_{11}}{\tau} = \frac{-5\pi^{1/2}}{24\nu G(1+e)(3-e)\tau}\left[\frac{1}{3}p_{12} + \nu a_{12}\right]\frac{u'}{\tau^{1/2}}\ , \qquad (19)$$

and constitutive relation (17) to eliminate γ_{22} from balance (5) to obtain,

$$\frac{a_{22}}{\tau} = \frac{-5\pi^{1/2}}{24\nu G(1+e)(3-e)\tau}\left[\frac{1}{3}p_{12} - \nu a_{12}\right]\frac{u'}{\tau^{1/2}}\ . \qquad (20)$$

Equations (19) and (20) and constitutive relation (7) demonstrate that the deviatoric components a_{11} and a_{22} are sums of terms proportional to $(u')^2$ or to products of a_{12} and u'. These nonlinear terms were neglected by Jenkins and Richman [1985]. Consequently, they predicted that, for flows of nearly elastic spheres, the components a_{11}, a_{22}, and a_{33} all vanish. In that approximation, the constitutive equations (8), (9), and (10) simplify and guarantee that the normal pressures p_{11}, p_{22}, and p_{33} are all equal.

Finally, we employ constitutive relation (18) to eliminate γ_{12} from balance (6) to obtain,

$$\frac{a_{12}}{\tau} = \frac{-\pi^{1/2}(3e-1)}{12(3-e)}\left[1 + \frac{5}{2(1+e)(3e-1)G}\right]\frac{u'}{\tau^{1/2}}\ , \qquad (21)$$

where we have neglected terms that are cubic in u', a_{12}, and products of u' and a_{12}. If equation (21) is employed to eliminate a_{12} from constitutive relation (7) and e is set equal to 1, then the resulting expression for the shear stress is identical to that obtained by Jenkins and Richman [1985].

2.2 Boundary Conditions

With appropriate conditions applied at the free surface and base of the incline, equations (1), (2), (3), (7), (9), (11), (15), (20), and (21) determine the variations with y of p_{12}, p_{22}, q, τ, γ, u', ν, a_{12}, and a_{22}. Although the location of the free surface is not known, the stresses and the energy flux each vanish there; i.e.

$$p_{12} = 0 \quad \text{and} \quad p_{22} = 0 \quad , \tag{22}$$

and

$$q = 0 \quad . \tag{23}$$

Because the stresses both vanish at the top of the flow, ν may be eliminated between equations (1) and (2) to demonstrate that $p_{12}/p_{22}=-\tan\phi$.

If ν is equal to 0 and τ is not, then according to constitutive relation (9) the normal stress condition at the top of the flow is automatically satisfied. Near the top of the flow, therefore, ν is small, the normal stress may be approximated by

$$p_{22} = \nu(\tau + a_{22}) \quad , \tag{24}$$

and because the ratio p_{12}/p_{22} is everywhere equal to $-\tan\phi$, the shear stress may be approximated by

$$p_{12} = -\nu(\tau + a_{22}) \tan\phi \quad . \tag{25}$$

Furthermore, if equations (21) and (25) are employed to eliminate a_{12} and p_{12} from constitutive relation (7), then we find that near the top of the flow, u' is given approximately by,

$$u' = \frac{24(3-e)(1+e)(\tau+a_{22})\tan\phi}{5\pi^{1/2}\tau^{1/2}}\nu \quad . \tag{26}$$

With u' given by equation (26), the lowest order approximation of equation (7) dictates that,

$$a_{12} = -(\tau + a_{22}) \tan\phi \quad , \tag{27}$$

and with p_{12}, u', and a_{12} given by equations (25), (26), and (27), balance (20) yields,

$$1+\frac{a_{22}}{\tau}=\frac{-3/2+\sqrt{9/4+6\tan^2\phi}}{2\tan^2\phi} \quad . \tag{28}$$

For small values of ν and prescribed values of τ and ϕ, equation (28) fixes a_{22}, equations (24) and (25) fix p_{22} and p_{12}, and for prescribed values of e, equation (26) fixes u'. As ν approaches zero, so too do the stresses p_{22} and p_{12} and the velocity gradient u'. However, in the same limit the components a_{22} and a_{12} of second moment each approach *nonzero* limits that depend only on the inclination angle ϕ and the local value of τ.

Of interest also are the limiting behaviors of the gradients τ', ν', a_{12}' a_{22}' and u" as ν approaches zero. By differentiating approximations (24) and (28) with respect to y, for example, we find that

$$\nu' = \frac{-\nu\cos\phi}{f(\phi)\,\tau}-\frac{\nu\tau'}{\tau} \quad , \tag{29}$$

where $f(\phi)$ is given by the right-hand-side of equation (28), and

$$a_{22}' = [f(\phi)-1]\,\tau' \quad . \tag{30}$$

If these are employed to eliminate ν' and a_{22}', then constitutive relation (11) for the energy flux demonstrates that τ', and therefore ν' and a_{22}', each approach zero with ν. Simple differentiation of approximations (26) and (27) with respect to y then demonstrates that both u" and a_{12}' approach zero in the same manner.

At the base of the incline (i.e. y=0), the rate **M** at which momentum is supplied to the flows by inelastic collisions between flow particles and the base must balance the traction vector at the base. Furthermore, the difference between the rate $-M_1u_1$ at which energy is supplied by slip work and the rate D at which it is absorbed by inelastic collisions between flow particles and the base must balance the energy flux at the base.

The transfer rates **M** and D depend on the geometry and dissipative nature of the incline. Here we focus on inclines that are flat surfaces to which identical, smooth, hemispherical particles of diameter d are randomly attached at an average distance s apart. In order to prevent flow particles from colliding with the flat part of the boundary, the maximum allowable value of s/d is $-1+(1+2\sigma/d)^{1/2}$. When a flow particle collides with a boundary particle the distance between their centers is $\delta\equiv(\sigma+d)/2$, and the energy dissipated is fixed by the coefficient of restitution e_w between them. A measure of the bumpiness of the boundaries is the angle $\theta\equiv\sin^{-1}(d+s)/(d+\sigma)$, which increases from 0 to $\pi/2$ as the boundaries evolve from perfectly flat to extremely bumpy.

We employ the general expressions for **M** and D obtained by Richman and Martin [1993] for assemblies of inelastic spheres that interact with bumpy boundaries described above. The expression for **M** involves an unknown factor that accounts for excluded volume and particle shielding at the boundary. If we first employ the balance between the x_2-components of **M** and the traction vector to write the unknown factor in terms of p_{22}, a_{22}, τ, and θ, then the balance between the x_1-components of **M** and the traction vector determines the slip velocity u(0) according to,

$$\frac{u}{\tau^{1/2}} = \frac{-\pi^{1/2}}{2^{1/2} I}\left[1 + \frac{a_{22}}{\tau}\left(1 - \frac{3}{4}\sin^2\theta\right) \right]\frac{p_{12}}{p_{22}} + \frac{\delta}{\sigma}\frac{(2I - \sin^2\theta)}{2I}\frac{u'}{\tau^{1/2}} + \frac{\pi^{1/2}}{2^{3/2} I}\frac{a_{12}}{\tau} \quad , \tag{31}$$

where $I(\theta) \equiv 2[2\csc^2\theta(1-\cos\theta)-\cos\theta]/3$. Furthermore, the energy flux at the boundary is determined by,

$$q = 2\left\{ -p_{12}u - \frac{2^{3/2}}{\pi^{1/2}}(1-e_w)\csc^2\theta(1-\cos\theta)\left[1 + \frac{a_{22}}{\tau}\left(1 - \frac{3}{4}\sin^2\theta\right) \right]^{-1}\tau^{1/2}p_{22} \right\} \quad . \tag{32}$$

Conditions (22), (23), (31), and (32) are the five conditions needed to complete the set of equations (1), (2), (3), (7), (9), (11), (15), (20), and (21). We provide a detailed description of the solution procedure in the following section.

2.3 Solution Procedure

The shear stress constitutive relation (7), the normal stress constitutive relation (9), and the x_2-x_2 and x_1-x_2 deviatoric components (20) and (21) of the balance of second moment determine ν, u', a_{12}, and a_{22} as functions of τ, p_{12}, and p_{22}. *In principle,* these functions may be employed to eliminate ν from the momentum equations (1) and (2), ν and u' from the energy equation (3) in which γ is replaced by expression (15), and ν, τ, ν', and a_{22}' from the energy flux constitutive equation (11). The four equations that result are first order ordinary differential equations that determine $\tau(y)$, $p_{12}(y)$, $p_{22}(y)$, q(y), and therefore $\nu(y)$, u'(y), $a_{12}(y)$, and $a_{22}(y)$ to within four constants of integration. These four constants and the dimensionless depth L (measured in particle diameters) are determined by the shear and normal stress conditions (22), the energy flux conditons (23) and (32), and by prescribing a nonzero value W^2 of τ at the top of the flow. The mass hold-up corresponding to this choice of W^2 may be calculated according to its definition,

$$m_t = \int_0^L \nu \, dy \quad . \tag{33}$$

The component $a_{11}(y)$ is then determined algebraically by equation (19), the component $a_{33}(y)$ is simply the sum $-(a_{11}+a_{22})$, and the stresses $p_{11}(y)$ and $p_{33}(y)$ are fixed by their constitutive relations (8) and (10). Finally, by direct integration of $u'(y)$, the profile $u(y)$ may be found to within a fifth constant that is determined by the momentum flux condition (31), and the mass flow rate may be calculated according to its definition,

$$\dot{m} = \int_0^L \nu u dy \quad . \tag{34}$$

Unfortunately, it is not possible in closed form to eliminate ν, u', a_{12}, and a_{22} from equations (1), (2), (3), and (11). Consequently, in the numerical integration of these equations, at each spatial location at which τ, p_{12}, and p_{22} are known it is necessary to invert the nonlinear algebraic equations (7), (9), (20), and (21) to determine the corresponding values of ν, u', a_{12}, and a_{22}. In order to avoid this difficulty, we actually *raise* the order of the system by differentiating equations (7), (9), (20), and (21) with respect to y. In this manner, the four resulting equations and the energy flux constitutive relation (11) may be written in matrix form:

$$[C]\{L\} = \{R\} \quad , \tag{35}$$

in which the components of the five dimensional vectors {L} and {R} are:

$$L_1 = \tau' , \qquad L_2 = \nu' , \qquad L_3 = a_{22}' , \qquad L_4 = a_{12}' , \qquad L_5 = u'' ; \tag{36}$$

and

$$R_1 = \frac{-\sin\phi}{2(1+e)G} , \; R_2 = \frac{-\nu\cos\phi}{2(1+e)} , \; R_3 = \frac{-\pi^{1/2}q}{4(1+e)\nu G\tau^{1/2}} , \; R_4 = \frac{\nu u'\sin\phi}{3} , \; R_5 = 0 . \tag{37}$$

The components of the 5x5 coefficient matrix [C], which are given explicitly in the Appendix, depend on various combinations of the unknowns τ, p_{12}, ν, u', a_{12}, and a_{22}. The momentum equations (1) and (2), the energy equation (3) in which γ is replaced by expression (15), and the matrix equation (35) are eight first order equations for τ, p_{12}, p_{22}. q, ν, u', a_{12}, and a_{22} that may be solved by straightforward numerical integration. The first and second rows of equation (35) are the differentiated forms of the shear stress relation (7) and the normal stress relation (9); the third row is the energy flux relation (11); and the fourth and fifth rows are the differentiated forms of the x_2-x_2

component (20) and the x_1-x_2 component (21) of the balance of second moment.

For fixed values of e, e_w, σ/d, s/d, and ϕ, we employ a fourth order Runge-Kutta technique to integrate equations (1), (2), (3), and (35) from the top of the flow, where p_{12}, p_{22}, and q vanish and τ is equal to its prescribed value W^2. Because, at the top of the flow, p_{22} vanishes and τ does not, ν must vanish there. However, we have seen in the previous section that under these circumstances the gradients τ', ν', a_{12}', a_{22}', and u" also vanish. Moreover, equations (1), (2), (3) and (15) demonstrate that when ν is equal to zero, so to are p_{12}', p_{22}', and q'. Integrations initiated when ν=0 therefore yield no spatial variations in p_{12}, p_{22}, q, τ, ν, a_{12}, a_{22}, and u'. This indicates that the theory predicts that the flows are infinitely deep and that p_{12}, p_{22}, q, τ, ν, a_{12}, a_{22}, and u' each approach their values at the top of the flow asymptotically from the base. To overcome this difficulty, we follow Oyediran et. al. [1992] and set ν equal to 10^{-6} at the top of the flow, which is equivalent to relaxing very slightly the normal stress condition there. Then with $\tau=W^2$, q=0, and a_{22}, a_{12}, u', p_{12}, and p_{22} given by equations (28), (27), (26), (25), and (24), the integration produces spatial variations as it proceeds toward the base. We have also initiated the integrations with several other combinations of ν and q between 10^{-5} and 10^{-7}, and in each case obtained results that were indistinguishable from those based on $\nu=10^{-6}$ and q=0.

For any value of W^2, the depth L is the distance from the point at which the integrations are initiated to the location at which the basal energy flux condition (32) is satisfied. When condition (32) is satisfied, the variations $p_{12}(y)$, $p_{22}(y)$, q(y), $\tau(y)$, $\nu(y)$, $a_{12}(y)$, $a_{22}(y)$, and u'(y), and the mass-hold-up are completely determined. With the slip velocity fixed by condition (31), the variation u(y) may then be determined by direct integration of u'(y), and the mass flow rate is fixed by its definition (34). The process of finding solutions is complicated only by the fact that there are a great variety of parameter values (e, e_w, σ/d, s/d, and ϕ) and initial values W^2 for which condition (32) can not be satisfied; under these circumstances the theory predicts that no steady, fully-developed flows can be maintained.

3. GRAVITY-DRIVEN FLOWS OF SMOOTH, INELASTIC SPHERES DOWN BUMPY INCLINES: RESULTS AND DISCUSSION

3.1 Initial Results

In this sub-section, we present a sample of the results obtained from the solution procedure described in section 2.3 above. In two previous papers, Richman and Marciniec [1990] and Oyediran et.al. [1992] employed a theory for nearly elastic particles, focused much of their attention on flow particles with $e=.8$, and boundaries with $e_w=.95$, $\sigma/d=1/2$, and $s/d=-1+2^{1/2}$, and found that steady, fully developed flows could be maintained at inclinations roughly between $\phi=19°$ and $21.5°$. In order to focus on flows more inelastic than these, we simply double their value of $(1-e)$ by taking $e=.6$, and do not alter their values of e_w, σ/d, and s/d. We find that for these more dissipative flows, the theory for highly inelastic particles predicts that the range of inclinations for which steady, fully developed flows may be maintained is raised to roughly between 20° and 26°. In all that follows, we take an intermediate inclination of $\phi=23°$ near the upper limit of the range.

In the left-hand panel of Figure 3.1, we show the variations of flow rate $\dot{m}$ with the value W of $\tau^{1/2}$ at the top of the flow. In in the right-hand panel, we eliminate W and show the corresponding variation of $\dot{m}$ with mass hold-up m_t. The lowest value (.158) of W shown on the curve in the left-hand panel is the minimum value at which the solid fraction throughout the flow is everywhere less than .65. The largest value (.990) of W shown on the curve is the maximum value that yields a mass hold-up m_t that is greater than unity. As W decreases from its maximum to its minimum value, the flows become less thermalized, more massive, faster, more shallow, and more dense. The flow rate increases because both the mass and the speed increase. For the parameters used here, there is only one flow for each flow rate.

In Figure 3.2, we plot the profiles of v, $w\equiv\tau^{1/2}$, and u for $m_t=4$, and $\dot{m}=103.2$, and $W=.498$. In Figure 3.3, we plot the corresponding profiles of $k_{11}^{1/2}\equiv(\tau+a_{11})^{1/2}$, $k_{22}^{1/2}\equiv(\tau+a_{22})^{1/2}$, and $k_{33}^{1/2}\equiv(\tau+a_{33})^{1/2}$, and p_{11}, p_{22}, and p_{33}. Solid dots on the profiles indicate the location ($y=13.47$) below which ninety-nine percent of the mass is contained. Within the flows, the rate at which energy is dissipated by inelastic collisions is greater than the rate at which it is supplied by gravity. For this reason, the boundary must supply energy to the flow, and the energy flux must be positive at the boundary. Interestingly, in the case shown here the gradients of τ and v make positive contributions to the energy flux at the boundary while the gradient of a_{22} actually makes a negative contribution.

The left-hand panels of Figures 3.2 and 3.3 demonstrate that near the top of the flow, the solid fraction is small, the components k_{22} and k_{33} are nearly equal, and both are less than k_{11}. As y decreases from about 15 to 9.4, the solid fraction increases dramatically from 0 to its maximum value .39, k_{22} rapidly approaches k_{11}, and both are greater than k_{33}. As y decreases from 9.4 to 0, the solid fraction gradually decreases from its maximum value to .15 at the boundary, k_{22} gradually approaches k_{33}, and both are less than k_{11}. Except near the top of the flow, where the solid fraction, velocity gradient, and normal stresses each vanish, the variations of the differences between p_{11}, p_{22}, and p_{33} with depth follow from the behaviors of k_{11}, k_{22}, and k_{33}. These variations are due primarily to variations in solid fraction and have been observed in the numerical simulations of homogeneous shearing by Walton and Braun [1986], Campbell [1989], and Hopkins and Shen [1992].

3.2 Search for Steady, Fully Developed, Gravity-Driven Flows

Next we conduct a study to determine a range of parameters over which steady, fully developed, gravity driven granular flows of identical, smooth, inelastic spheres down bumpy inclines could be maintained. The appropriate boundary value problem and the numerical solution procedure have been described in detail in sections XXX. In what follows, we describe the parameters relevant to the inclined flows investigated, the range of these parameters that we included in our study, and the resulting ranges over which steady, fully developed flows could be maintained.

3.2.1 Parameters

We are concerned with steady, fully developed, gravity driven flows of identical, inelastic spheres down bumpy inclines. The diameter of each sphere is σ, the coefficient of restitution between them is e. and the angle between the incline and the horizontal is ϕ.

Here we focus on inclines that are flat surfaces to which identical, smooth, hemispherical particles of diameter d are randomly attached at an average distance s apart. Dimensionless measures of the boundary geometry are $r \equiv \sigma/d$ and $\Delta \equiv s/d$. In order to prevent flow particles from colliding with the flat part of the boundary, the maximum value of Δ is equal to $-1+(1+2r)^{1/2}$. When a flow particle collides with a boundary particle the energy dissipated is fixed by the coefficient of restitution e_w between them.

Additional parameters are the granular temperature at the "top" of the flow, and the "depth" of flow. However in our previous progress report, we showed that if the stresses and energy flux vanish at the top of the flows, then the kinetic theory predicts that the flows are infinitely deep, and that the stresses, energy flux, and solid fraction each approach zero asymtotically from the base. This presents a numerical difficulty because the integrations proceed *from* the top of the flow *to* the base, and requires somewhat artificial definitions of the "top" of the flow and the "depth" of the flow.

To address these issues, we define the "top" of the flow as the location at which the energy flux vanishes but where the solid fraction is equal to a small non-zero value (typically 10^{-6}). With the granular temperature τ_{top} fixed at a nonzero value there, this allows the integrations to be initiated from this location and is equivalent to relaxing very slightly the normal stress condition at the "top" of the flow. Because the ratio of the shear stress to normal stress is everywhere equal to $\tan\phi$, in this manner the shear stress condition is also relaxed very slightly at the "top" of the flow. The dimensionless parameter corresponding to τ_{top} is $T_{top} \equiv \tau_{top}/\sigma g$, where g is the vertical acceleration due to gravity.

However, it is not appropriate to define the "depth" of flow as the distance from the base to the location at which the integrations are initiated. This is because the integrations may include great distances over which the solid fraction is extremely small, and these distances may be quite sensitive to the arbitrary value that the solid fraction is assigned at the "top." For these reasons, proceeding from the "top" of the flow, we instead take the "depth" of flow L to be the height below which ninety-nine percent of the mass of the flow resides. Defined in this manner, the depth does not include the great distances over which the solid fraction is extremely small, and is not dependent on the small value of solid fraction that we choose to initiate the integrations. The dimensionless parameter measuring this "depth" is $\beta \equiv L/\sigma$.

We have experimented with values of solid fraction at the "top" ranging from 10^{-3} to 10^{-7} and have observed that while the distances required for the solid fraction to reach .01, for example, may be quite sensitive to these values and may be quite large, the variations in all other mean fields from their values at the "top" are quite small over these same distances. Consequently, the dimensionless value of the granular temperature at the upper portion of the flow may be accurately approximated by T_{top}. Most importantly, we have observed that the profiles of all the mean fields are quite insensitive to the value of the solid fraction chosen to initiate the integration from the "top."

In summary, the *input* parameters of interest here are the angle of inclination ϕ, the coefficient of restitution e between flow particles, the boundary bumpiness parameters r and Δ, the coefficient of restitution e_w between flow particles and boundary particles, and the granular temperature at the "top" of the flow T_{top}. The only *output* parameters that we are concerned with in this study are the depth β and the solid fraction ν.

3.2.2 Range of Parameters

In this study, we focus on boundaries for which r=1. These are boundaries with bumps that have the same diameters as the flow particles. Consequently, the range on Δ is between 0 (i.e. no spacing between bumps) to the maximum value .732 beyond which flow particles will collide with the falt part of the boundary. We consider all angles of inclination ϕ between 0°

and 90°, but limit our attention to cases in which the coefficients of restitution e and e_w are equal and between .5 and 1.0. In addition, we accept a solution to the boundary value problem only if the flow depth predicted by the theory is greater than one particle diameter, and only if the theory predicts that the solid volume fraction ν is everywhere less than .65.

In order to determine a reasonable range of the final input parameter T_{top}, we imagine the flow as consisting of an observable collisional portion of depth β above which there exists a diffuse saltating region of height h. The saltating region occurs because particles with mean square fluctuation speeds $3\tau_{top}$ at the upper layer of the collisional portion of the flows rarely collide with other particles and are influenced primarily by gravity alone. Simple conservation of energy arguments dictate that $3\tau_{top} \leq 2gh$, or in dimensionless form,

$$T_{top} \leq \frac{2h}{3\sigma} \quad , \tag{1}$$

where the height h should be at least half of the depth of the collisional layer. A flow depth β=100 would dictate that h=50, and therefore that, for fixed values of r, Δ, e, e_w, and ϕ, we consider all values of $T_{top} \leq 33$. However, in the interest of saving computer time and because we have found that most solutions have depths no greater than 30 particle diameters, we instead take h=15 and consider the smaller range $0 \leq T_{top} \leq 10$. In this manner, we consider saltating layers that are at least half the height of the collisional portion of most flows, and more typically are of the same heights or of greater heights than the collisional portion of the flow.

In summary, the ranges of *input* parameters that we consider here are:

$$r = 1 \qquad \text{and} \qquad 0 \leq \Delta \leq .732 \quad ; \tag{2}$$

$$.5 \leq e{=}e_w \leq 1.0 \qquad \text{and} \qquad 0° \leq \phi \leq 90° \quad ; \tag{3}$$

and

$$0 \leq T_{top} \leq 10 \quad . \tag{4}$$

The ranges of *output* parameters are:

$$\beta \geq 1 \qquad \text{and} \qquad \nu \leq .65 \quad . \tag{5}$$

3.2.3 First Search Procedure: Finding *at Least One* Solution for prescribed values of e, e_w, r, Δ, and ϕ

A recurring question that we answer in this first search is the following: for prescribed values of r(=1), Δ, $e=e_w$, and ϕ, can a steady, fully developed, gravity-driven flow within the ranges (4) and (5) be maintained?

In order to answer this question, we pick a value for T_{top} within range (4) and integrate downward until we either find a solution (i.e. satisfy the basal boundary conditions) within each of ranges (5), or until either ν exceeds .65, or until it appears that the basal boundary condition will not be satisfied regardless of how far the integrations proceed. If we find a solution, then we have demonstrated that at least one such steady, fully developed flow can be maintained for the prescribed values of r(=1), Δ, $e=e_w$, and ϕ, and we need not proceed further. If we do not find a solution, then we increment the value of T_{top} and repeat the downward integration. We continue to increment T_{top} until we either find a solution for some value of T_{top} within range (4), or until we have varied T_{top} throughout the entire range (4) and have not found any such solutions.

In order to determine, for prescribed values of r(=1), Δ, and $e=e_w$, the *range* of angles ϕ between which steady, fully developed, gravity-driven flows can be maintained, we repeat the process described above for all values of ϕ between 0° and 90° incremented by 1°.

3.2.4 Results of the First Search

In Figure 3.4, we show as a darkened area in the ϕ-e plane the values of ϕ and e for which steady, fully developed, flows are possible within the bounds described by inequalities (4) and (5) for $.5<e=e_w<1.0$, when r=1 and $\Delta=.414$. As expected, as $e=e_w$ increases from .5, the typical inclinations at which steady, fully developed flows are possible generally decrease. In these flows, the rate at which energy is dissipated must help to balance the rate at which it is supplied by gravity. Furthermore, the rate at which energy is supplied to the flow by gravity decreases as the angle of inclination decreases. Consequently, as the flows become less dissipative, the work done by gravity, and therefore the angles of inclination decrease. When $e=e_w=1.0$, no energy is dissipated within the flow or at the boundary, and the work done by gravity must vanish. In this limit, the theory predicts that steady, fully developed flows can be maintained only when $\phi=0°$.

In Figure 3.5, we show as a darkened area in the ϕ-Δ plane the values of ϕ and Δ for which steady, fully developed, flows are possible within the bounds described by inequalities (4) and (5) for $0<\Delta<.732$, when r=1 and $e=e_w=.5$. (If Δ exceeds .732 when r=1, then the flow particles could collide with the flat part of the boundary.) As expected, as Δ increases from 0 to its maximum value, the typical inclinations at which steady, fully developed flows are possible generally increase. As Δ increases, the boundary becomes bumpier, the slip velocity decreases, and the energy supplied to the flow by the working of the traction at the boundary decreases. In order to balance the energy dissipated due to inelastic collisions in the flow and at the boundary, the work done by gravity, and therefore the angles of inclination, must increase.

3.2.5 Second Search Procedure: Finding *All* Solutions for prescribed values of e, e_w, r, Δ, and ϕ

We have focused on steady, fully developed, gravity-driven flows of identical, smooth spheres down bumpy inclines, with flow depths greater than one particle diameter, solid fraction profiles everywhere less than .65. For prescribed boundary bumpiness (r and Δ), restitution coefficients of the boundary (e_w) and the flow particles (e), and angle of inclination (ϕ), we have determined whether *at least one* such flow could be maintained. We did so by determining whether there was at least one value of dimensionless granular temperature T_{top} within the range $0<T_{top}\leq 10$ for which the appropriate boundary value problem (described in section XXX) could be solved.

Now we choose values of r, Δ, e, e_w, and ϕ for which we know that at least one solution of the type described above may be maintained, and determine the *complete* range of T_{top} (within $0<T_{top}\leq 20$ in the first case that we will consider, and within $0<T_{top}\leq 10$ in the second case) for which such flows can be maintained. For each value of T_{top} in this range, we can calculate the corresponding values of mass hold-up (m_t), mass flow rate ($\dot{m}$), depth β, total fluctuation energy per unit area (E), slip velocity (v) at the base, velocity ($u(y=\beta)$) at the top, and the depth-averaged values of solid fraction, velocity, and granular temperature. In this manner, we thoroughly characterize *all* the steady, fully developed, gravity driven flows that are possible for prescribed sets of r, Δ, e, e_w, and ϕ.

We characterize the solutions by calculating the corresponding values of mass hold-up (m_t), mass flow rate ($\dot{m}$), depth β, total fluctuation energy per unit area (E), slip velocity (v) at the base, the velocity ($u(y=\beta)$) at the top, and the depth-averaged values of solid fraction $\bar{\nu}$, velocity $\bar{u}$, and granular temperature $\bar{T}$. Here, the dimensionless depth β and distance y from the base are nondimensionalized by particle diameter σ, the dimensionless velocities u, v, and $u(y=\beta)$ are nondimensionalized by $(\sigma g)^{1/2}$, the dimensionless granular temperature T is nondimensionalized by σg, the depth-average of any quantity q(y) is defined by,

$$\bar{q} \equiv \frac{1}{\beta}\int_0^{\beta} q(y)dy \quad , \tag{1}$$

and the depth-totaled quantities m_t, $\dot{m}$, and E are equal to $\beta\bar{v}$, $\beta\overline{vu}$, and $\beta\overline{vT}$, respectively.

3.2.6 Results of the Second Search

Figure 3.5 demonstrates that when r=1, $e=e_w=.5$, and $\Delta=0$, for example, steady, full developed flows are possible when ϕ is approximately between 14° and 26°. In what follows, we consider three intermediate angles ϕ for this value of Δ, and for each angle determine the *full range* of T_{top} that yields solutions to the boundary value problem.

Here we consider the case in which r=1, $e=e_w=.5$, $\Delta=0$, and choose three angles $\phi=21°$, 22.5°, and 24° in the range $14°<\phi<26°$. In Figure 3.6, we show the variations of β, m_t, $\dot{m}$, $\bar{T}$, $\bar{v}$, E, $\bar{u}$, v, and $u(y=\beta)$ with $T_{top}\equiv T(y=\beta)$. At the maximum value of $T(y=\beta)=20$, the flows are quite deep and quite dilute. The minimum values of $T(y=\beta)$ for $\phi=21°$, 22.5°, and 24° are 0.013613, 0.014549, and 0.015889, respectively. In each case, as $T(y=\beta)$ decreases to its minimum value, the flows become more shallow, more massive, and therefore more dense. In fact, the theory predicts that for values of $T(y=\beta)$ below the minima, the solid fraction somewhere within the flows exceeds .65. For each inclination, when $T(y=\beta)$ is exactly equal to its minimum value, the flow rate assumes a corresponding *finite maximum* value.

To make the variations with $T(y=\beta)$ near its minimum value more clear, in Figure 3.7 we replot the variations of $\dot{m}$, m_t, and $\bar{v}$ with $T(y=\beta)$ on log-log scales. The values of $\dot{m}$, m_t, $\bar{v}$ and β corresponding to the minimum value of $T(y=\beta)$ for each angle shown in Figures 3.6 and 3.7 are summarized in the table below:

ϕ	$T(y=\beta)$ (minimum)	$\dot{m}$	m_t	$\bar{v}$	β
21°	.013613	32.236	2.672	.494	5.357
22.5°	.014549	73.566	3.142	.416	7.478
24°	.015889	168.411	3.727	.318	11.621

The variations of $\dot{m}$ with $T(y=\beta)$ shown in both Figures 3.6 and 3.7 also indicate that corresponding to each inclination is a *nonzero minimum* value of $\dot{m}$. Indeed, we have found that corresponding to every angle in the range $14^\circ \leq \phi < 26^\circ$ is a nonzero minimum value and a finite maximum value of $\dot{m}$ between which steady, fully developed flows can be maintained.

According to Figure 3.6, as $T(y=\beta)$ decreases from 20 over most of its range, the flows become less thermalized (as might be expected) and slower. However as $T(y=\beta)$ continues to decrease near its minimum value, these trends are reversed. Furthermore, the quantities m_t, $\dot{m}$, $\bar{v}$, and to a lesser extent E are extremely sensitive to changes in $T(y=\beta)$ near its minimum value but relatively insensitive to changes in $T(y=\beta)$ away from its minimum value. These observations indicate that there is no simple relationship between $T(y=\beta)$, which can not be controlled experimentally, and such parameters as $\dot{m}$ and E, which may be controllable. For this reason, when presenting the results, it is probably better to parameterize the solutions by either $\dot{m}$ or E.

In Figure 3.8, for example, we eliminate $T(y=\beta)$ and plot the variations of E and m_t with $\dot{m}$ when $r=1$, $e=e_w=.5$, and $\Delta=0$, for $\phi=21^\circ$, 22.5°, and 24°. At each inclination, there are two flows for each flow rate near the minimum. One is less thermalized and more massive than its counterpart. At higher flow rates, only the less thermalized and more massive flow is possible; as the flow rate increases to its maximum, this flow becomes more thermalized and more massive.

In a typical experiment, the thermal energy at the inlet of an incline is influenced by the height from which the particles are dropped and/or by vibrating the inlet. The left-hand panel of Figure 3.8 gives some indication of how much thermal energy should be imparted to the particles at the inlet to to ensure that their initial states are near to the steady, fully developed states predicted by the theory. Conversely, the left-hand panel of Figure 3.8 indicates that the steady, fully developed flows predicted by the theory may not be established if, for a fixed flow rate, the magnitude of difference between the thermal energy at the inlet and the predicted value of E is too great. We anticipate that the maximum mismatch between the thermal energy at the inlet and the predicted value of E (beyond which a steady, fully developed flow can not be established) increases as the length of the chute increases.

In Figure 3.9, we plot the variations of β, $\bar{v}$, and $\bar{u}$ with $\dot{m}$ corresponding to those of E and m_t shown in Figure 3.8. For a given angle, Figure 3.9 demonstrates that of the two flows that are possible at flow rates near the minimum, the less thermalized and more massive flow is also more shallow, more dense, and slower than its counterpart. At higher flow rates, only the more shallow, more dense, slower flow is possible; as the flow rate increases to its maximum the depth of this flow changes only slightly as it becomes more dense and faster. For completeness, we have also included in Figure 3. 9 the corresponding variations of β, $\bar{v}$, and $\bar{u}$ with E.

We have found that (when $r=1$, $e=e_w=.5$, and $\Delta=0$), for all inclinations in the range $14^\circ<\phi<26^\circ$ for which at least one steady, fully developed flow could be maintained, we found that there was a finite maximum value of $\dot{m}$

between which steady, fully developed flows could be maintained. However, as the next case that we investigate will demonstrate, there are boundaries, flow particles, and inclinations for which the kinetic theory predicts that steady, fully developed flows can be maintained at *all flow rates* above a minimum value. These are qualitatively different from the results presented in Figures 3.6 through 3.9, in which maximum flow rates (above which steady flows could not be maintained) were determined for each case considered. The fact that it is possible to find circumstances under which there are *no maximum flow rates* that limits the occurrence of steady flows may be useful when in practice it is necessary to steadily transport extremely high volumes of granular materials.

Figure 3.2 demonstrates that when $e=e_w=.5$, $r=1$, and $\Delta=.414$, for example, steady, full developed flows are possible when ϕ is approximately between 21° and 35°. In what follows, we consider four intermediate angles ϕ for these values of e, e_w, r and Δ, and for each angle determine the *full range* of $T(y=\beta)$ that yields solutions to the boundary value problem. In addition, we characterize the solutions by calculating the corresponding values of mass hold-up (m_t), mass flow rate ($\dot{m}$), depth β, total fluctuation energy per unit area (E), slip velocity (v) at the base, the velocity ($u(y=\beta)$) at the top, and the depth-averaged values of solid fraction $\bar{\nu}$, velocity $\bar{u}$, and granular temperature $\bar{T}$.

We choose four intermediate angles $\phi=25.5°$, $27.505°$, $28°$, and $34°$ in the range $21°<\phi<35°$. In Figure 3.10, we show for each angle the variations of β, m_t, $\dot{m}$, $\bar{T}$, $\bar{\nu}$, E, $\bar{u}$, v, and $u(y=\beta)$ with $T(y=\beta)$. At the maximum value of $T(y=\beta)=10$, the flows are quite deep and quite dilute. In each case, as $T(y=\beta)$ decreases from its maximum value, the flows become more massive and more shallow. However, as $T(y=\beta)$ nears its minimum value, the flow depths reach their minimum values and then begin to increase. For $\phi=25.5°$ and $27.505°$, the increase in depth is not sufficient to mitigate the increase in mass hold-up, and the assemblies become too dense to flow as $T(y=\beta)$ decreases near its minimum value. For these two lower inclinations, the theory predicts that for values of $T(y=\beta)$ below the minima, the solid fraction somewhere within the flows exceeds .65. For these inclinations, when $T(y=\beta)$ is exactly equal to its minimum value, the flow rate assumes a corresponding *finite maximum* value. However, for the two upper inclinations $\phi=28°$ and $34°$, the increase in depth as $T(y=\beta)$ decreases near its minimum value is sufficient to compensate for the increase in mass hold-up. For these two higher inclinations, the assemblies do not become too dense to flow, and the mass flow rates increase without bound as $T(y=\beta)$ approaches its minimum value. **Consequently, we find here that for $r=1$, $e=e_w=.5$, $\Delta=.414$** (unlike for the case $r=1$, $e=e_w=.5$, and $\Delta=0$) **there are relatively high inlinations at which the flow rates are unbounded.** For the same values of r, e, e_w, and Δ, there are lower inclinations at which the flow rate is bounded by a finite maximum. In figures yyy we will focus on the transition from inclinations at which the flow rates are bounded to those at which the flow rates are unbounded.

To make the variations with $T(y=\beta)$ near its minimum value more clear, in Figure 3.11 we replot the variations of $\dot{m}$, and $\bar{v}$ with $T(y=\beta)$ on log-log scales. The variations of $\dot{m}$ with $T(y=\beta)$ shown in both Figures 3.10 and 3.11 also suggest that corresponding to each inclination is a *nonzero minimum* value of $\dot{m}$ above which steady, fully developed flows can be maintained.

According to Figure 3.10, as $T(y=\beta)$ decreases from 10 over most of its range, the flows become less thermalized (as might be expected) and slower. However as $T(y=\beta)$ continues to decrease near its minimum value, these trends are reversed. Furthermore, the quantities m_t, $\dot{m}$, $\bar{v}$, and E are extremely sensitive to changes in $T(y=\beta)$ near its minimum value but relatively insensitive to changes in $T(y=\beta)$ away from its minimum value. These observations indicate that there is no simple relationship between $T(y=\beta)$, which can not be controlled experimentally, and such parameters as $\dot{m}$ and E, which may be controllable. For this reason, when presenting the results, it is probably better to parameterize the solutions by either $\dot{m}$ or E.

In Figure 3.12, for example, we eliminate $T(y=\beta)$, and plot the variations of E and m_t with $\dot{m}$ when $r=1$, $e=e_w=.5$, and $\Delta=.414$, for $\phi=25.5°$, 27.505°, 28° and 34°. The left-hand panel of Figure 3.12 indicates how much thermal energy should be imparted to the particles at the inlet to to ensure that their initial states are near to the steady, fully developed states predicted by the theory. For each inclination, the endpoints of these curves at the lower flow rates correspond to very deep, very dilute flows of nonzero mass hold-ups. The endpoints for the two lower inclinations at the upper flow rates correspond to relatively dense flows in which the solid fraction is somewhere equal to .65. The two upper inclinations have no corresponding (high-flow-rate) endpoints.

In the upper portion of Figure 3.13, we plot the variations of β, $\bar{v}$, and $\bar{u}$ with $\dot{m}$ corresponding to those of E and m_t shown in Figure 3.12. Of particular interest is the variation of $\bar{v}$ with $\dot{m}$ shown in the middle panel. At the two lower inclinations, Near the higher-flow-rate end points, the depth-averaged solid fraction increases rapidly with small changes in flow rate. This indicates that these endpoints occur because the assemblies become too dense to flow rapidly. At the two lower inclinations, the depth-averaged solid fractions are quite insensitive to large increases in the high flow rates, and appear to approach relatively dilute asymptotic values. This indicates that at these inclinations, the flows do not become too dense regardless of how large the flow rates become.

For completeness, we have included in the lower portion of Figure 3.13, the corresponding variations of β, $\bar{v}$, and $\bar{u}$ with E.

3.2.7 The Transition From Inclinations with Finite Maximum Flow Rates to those with Unbounded Maximum Flow Rates

For prescribed boundary bumpiness ($r=1$ and $\Delta=.414$), restitution coefficients of the boundary ($e_w=.5$) and the flow particles ($e=.5$), and angles of inclination ($\phi=25.5°$, $27.505°$, $28°$, and $34°$), we determined what appeared to be *complete* range of $T(y=\beta)$ (within $0<T(y=\beta)\leq 10$) for which such flows can be maintained. For the two lower inclinations ($\phi=25.5°$ and $27.505°$), we found that there was a nonzero minimum and a finite maximum flow rate between which steady, fully developed flows can be maintained. However, for the two upper inclinations ($\phi=28°$ and $34°$), although there was a nonzero minimum flow rate for each, *it appeared* that there was no maximum flow rate that limited the occurrence of steady, fully developed flows.

We now consider in greater detail the same parameter values ($r=1$, $\Delta=.414$, and $e=e_w=.5$) and focus on inclinations near the apparent transition from the those for which there exists a maximum flow rate to the inclinations for which there appeared to be no such maximum. Using careful numerical computations, we demonstrate that the transition is real and we determine the angle at which it occurs. We have devoted the time to these issues because the existence of cases in which there are *no maximum flow rates* that limit the occurrence of steady flows may be of great practical value when it is necessary to steadily transport extremely high volumes of granular materials.

Here we consider the case in which $r=1$, $e=e_w=.5$, $\Delta=.414$, and choose six angles $\phi=27.3°$, $27.5°$, $27.52°$, $27.55°$, $27.75°$, and $28°$ near the apparent transition from the those angles for which there exists a maximum flow rate to those angles for which there appeared to be no such maximum. In addition, we focus on values of $T(y=\beta)$ (between 0 and ,.8) near the apparent minimum values suggested by the figures 3.10 through 3.13. We do so because the flow rate increases rapidly with decreasing values of $T(y=\beta)$ near the minimum values of $T(y=\beta)$. We determine whether a distinction can be made between those angles for which the flow rate increases to a finite maximum and those angles for which the flow rate increases without bound.

In Figure 3.14, we show for each angle the variations of β, m_t, $\dot{m}$, $\bar{T}$, $\bar{v}$, E, $\bar{u}$, v, and $u(y=\beta)$ with $T(y=\beta)$ between 0 and .8. For $\phi=27.3°$ and $27.5°$, as $T(y=\beta)$ decreases from .8, *the flow rates increase to an identifiable finite maximum values* and then decrease until the assemblies become too dense to flow. For these inclinations, there are no gaps in the range of $T(y=\beta)$ for which steady, fully developed flows can be found. At these angles, the occurrences of steady fully-developed flows are limited by finite maximum flow rates.

However, for $\phi=27.52°$, $27.55°$, $27.75°$, and $28°$, we find that between the extreme values of $T(y=\beta)$ for which steady, fully developed flows can be found, there is a sub-range $T'\leq T(y=\beta)\leq T^*$ for which steady, fully developed flows can not be found. Most importantly, *the flow rates apparently become infinite as $T(y=\beta)$ approaches T' from below or T^* from above.* Consequently, inclinations for which such a gap in $T(y=\beta)$ occurs are those at which steady, fully developed flows are not limited by a maximum flow rate.

As $T(y=\beta)$ approaches T^* from above, the flow rates increase dramatically, while the flows do not become too dense to prevent the assemblies from flowing. For values of $T(y=\beta)$ between T^* and T', integrations proceed from the top of the flow indefinitely downward without satisfying the basal boundary condition. However, at no point in the integrations does the solid fraction exceed .65. As $T(y=\beta)$ decreases away from T', the flow rates at first decrease, and the depth-averaged solid fraction eventually increases until the assemblies become too dense to flow. Based on these observations, we believe that, independent of such artificial restrictions as $\nu \leq .65$, the theory predicts that there is a real gap in the values of $T(y=\beta)$ for which steady, fully-developed flows can be found, and that the flow rates corresponding to the cases $T(y=\beta)=T^*$ and $T(y=\beta)=T'$ are unbounded. Interestingly, it appears that the upper and lower limits, T' and T^*, of the gap depend on inclination angle ϕ, and that the size of the gap increases as the inclination increases from the angle at which the gap first appears.

The results shown in Figure 3.14 suggest that the transition from those angles for which the flow rate increases to a finite maximum and those angles for which the flow rate increases without bound occurs between $\phi=27.5°$ and 27.52°. In what follows, we determine the transition angle with more precision and further demonstrate the qualitative differences between those flows that occur below the transition angle and those that occur above the transition angle. In Figures 3.15, 3.16, 3.17, 3.18, and 3.19 we show the variations of β, m_t, $\dot{m}$, $\bar{T}$, $\bar{\nu}$, E, $\bar{u}$, ν, and $u(y=\beta)$ with the difference $T(y=\beta)-T^*$, for $\phi=27.5°$, 27.505°, 27.51°, 27.75°, and 28°, respectively.

Of greatest interest here are the variations of $\dot{m}$ and $\bar{\nu}$ with the difference $T(y=\beta)-T^*$. Figures 3.15 and 3.16 demonstrate that when $\phi=27.5°$ and 27.505°, for example, the flow rates increase at diminishing rates as $T(y=\beta)$ approaches T^* from above (i.e. as the positive difference $T(y=\beta)-T^*$ becomes smaller). This suggests that the theory would predict a finite maximum rate (corresponding to the limit $T(y=\beta)=T^*$) that limits the occurrence of steady, fully developed flows. Because there is no gap in the range of $T(y=\beta)$ for which steady, fully developed flows can be found, the values of T^* for $\phi=27.5°$ and $\phi=27.505°$ are taken to be the values of $T(y=\beta)$ at which the "spikes" occur in the variations of flow rate with $T(y=\beta)$, shown in the uppermost right-hand panels of Figures 3.14 and 3.10.

By contrast, Figures 3.17, 3.18, and 3.19 demonstrate that when $\phi=27.51°$, 27.75°, and 28°, the flow rates increase nearly linearly with $-\log[T(y=\beta)-T^*]$. This suggests that the flow rates would become unbounded in the limiting case $T(y=\beta)=T^*$. To check that the increase in flow rate does not diminish, we have have observed the linear relationship between flow rate and the quantity $-\log[T(y=\beta)-T^*]$ when the difference $T(y=\beta)-T^*$ is as small as 10^{-7} when $\phi=27.75°$ (Figure 3.18), and when the difference is as small as 10^{-9} when $\phi=28°$, (Figure 3.19).

Based on these results, we conclude that when r=1, $e=e_w=.5$, and $\Delta=.414$, the transition between those angles for which the flow rate increases to a finite maximum and those angles for which the flow rate increases without bound occurs at inclinations ϕ between 27.505° and 27.51°.

3.3 Figures

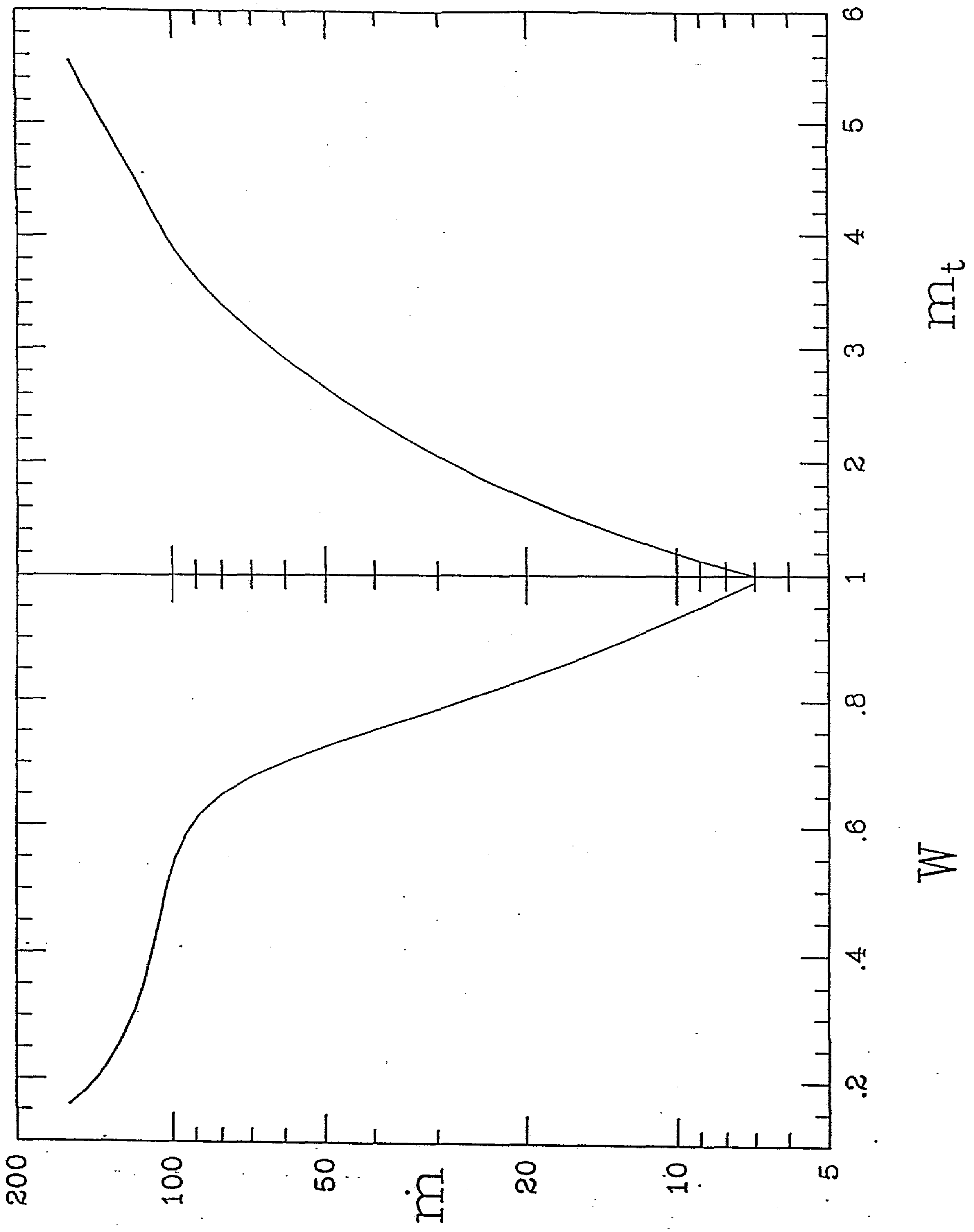

Figure 3.1: The variations of $\dot{m}$ with W and m_t for e=.6, e_w=.95, $\sigma/d=1/2$, $s/d=-1+2^{1/2}$ and $\phi=25°$.

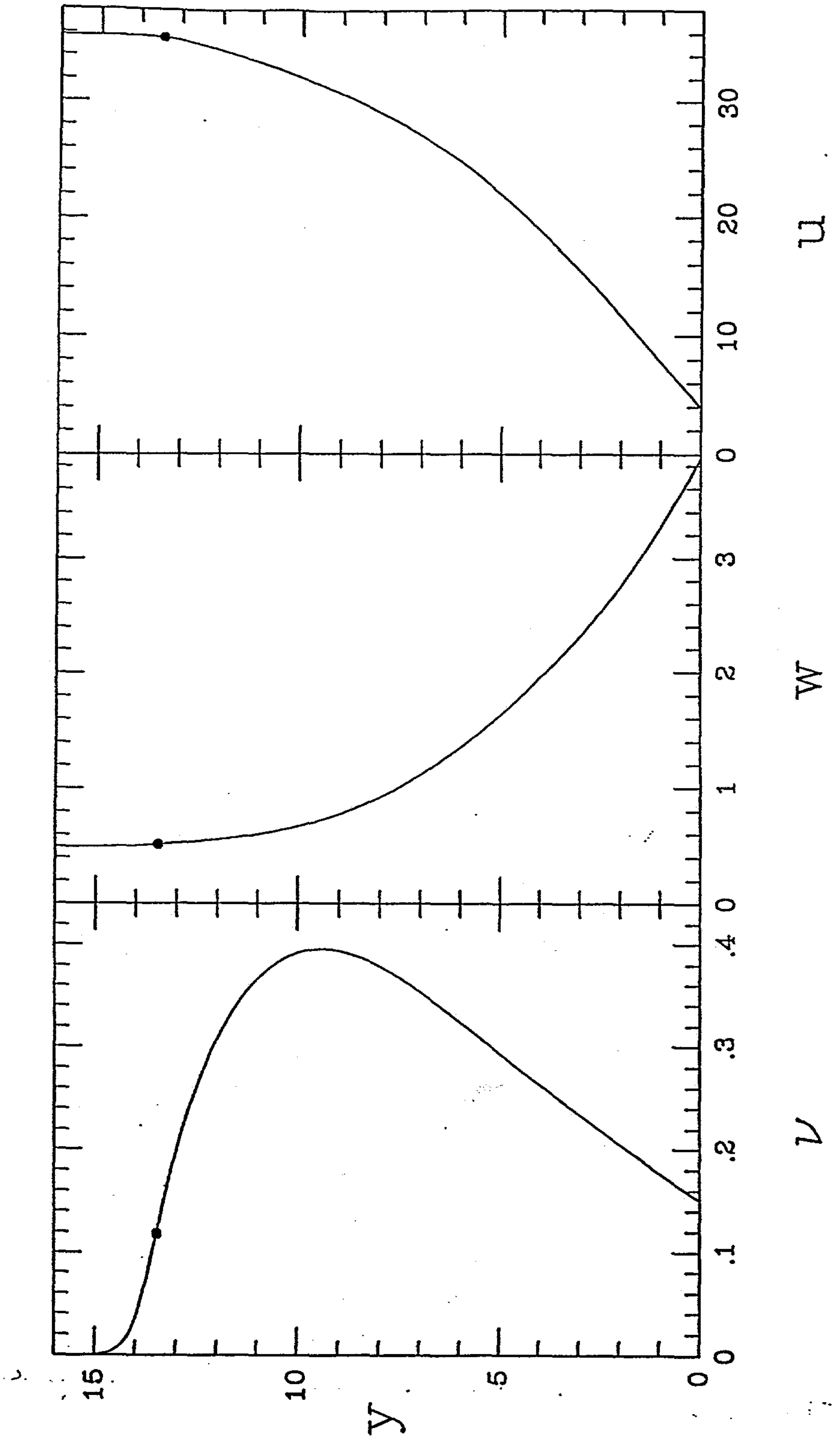

Figure 3.2: The variations of v, w, and u with y for e=.6, e_w=.95, $\sigma/d=1/2$, $s/d=-1+2^{1/2}$ and $\phi=25°$, when $m_t=4$.

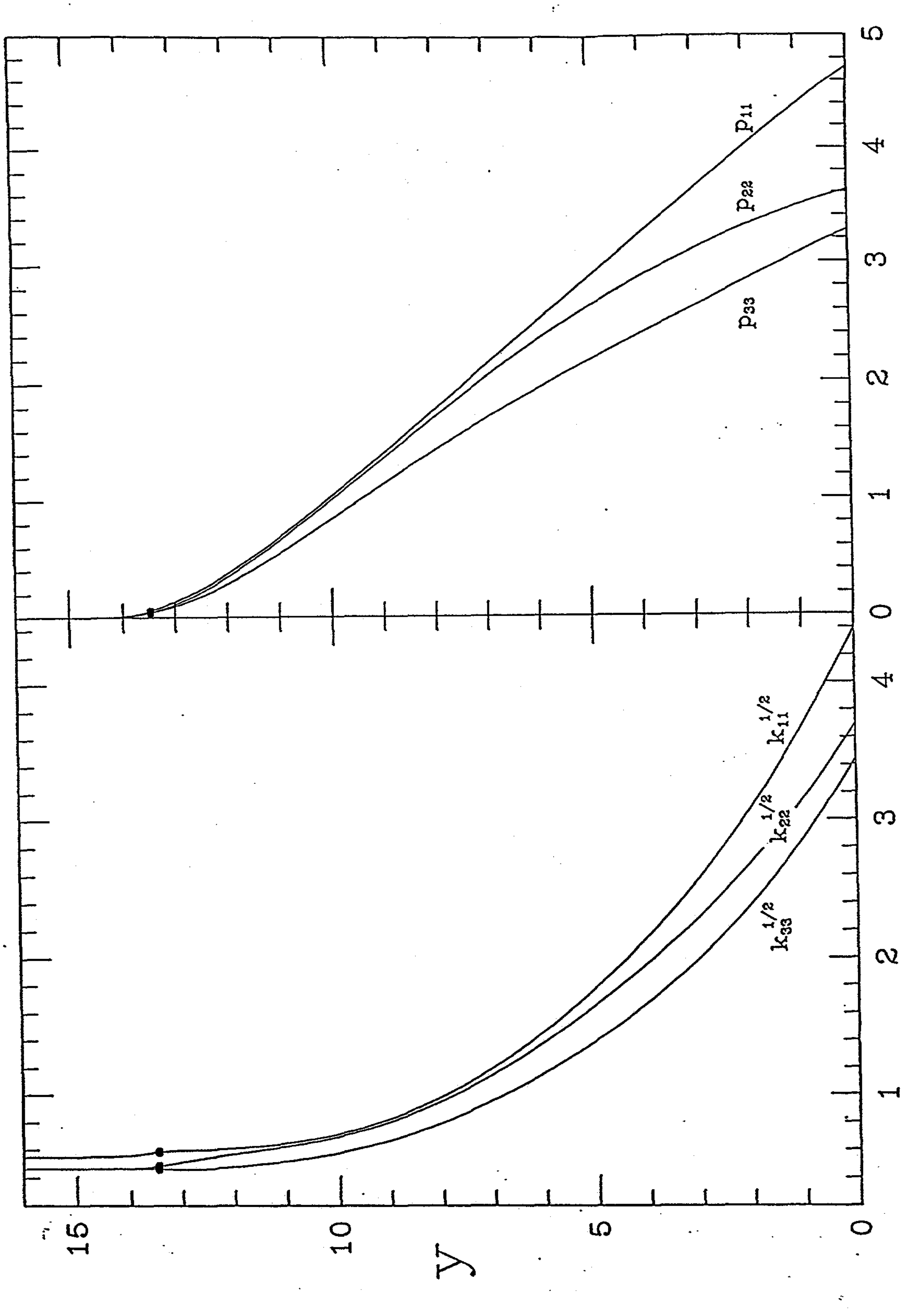

Figure 3.3: The variations with y of $k_{11}^{1/2}$, $k_{22}^{1/2}$, and $k_{33}^{1/2}$; and the variations with y of p_{11}, p_{22}, and p_{33} for e=.6, e_w=.95, $\sigma/d=1/2$, $s/d=-1+2^{1/2}$ and $\phi=25°$, when $m_t=4$.

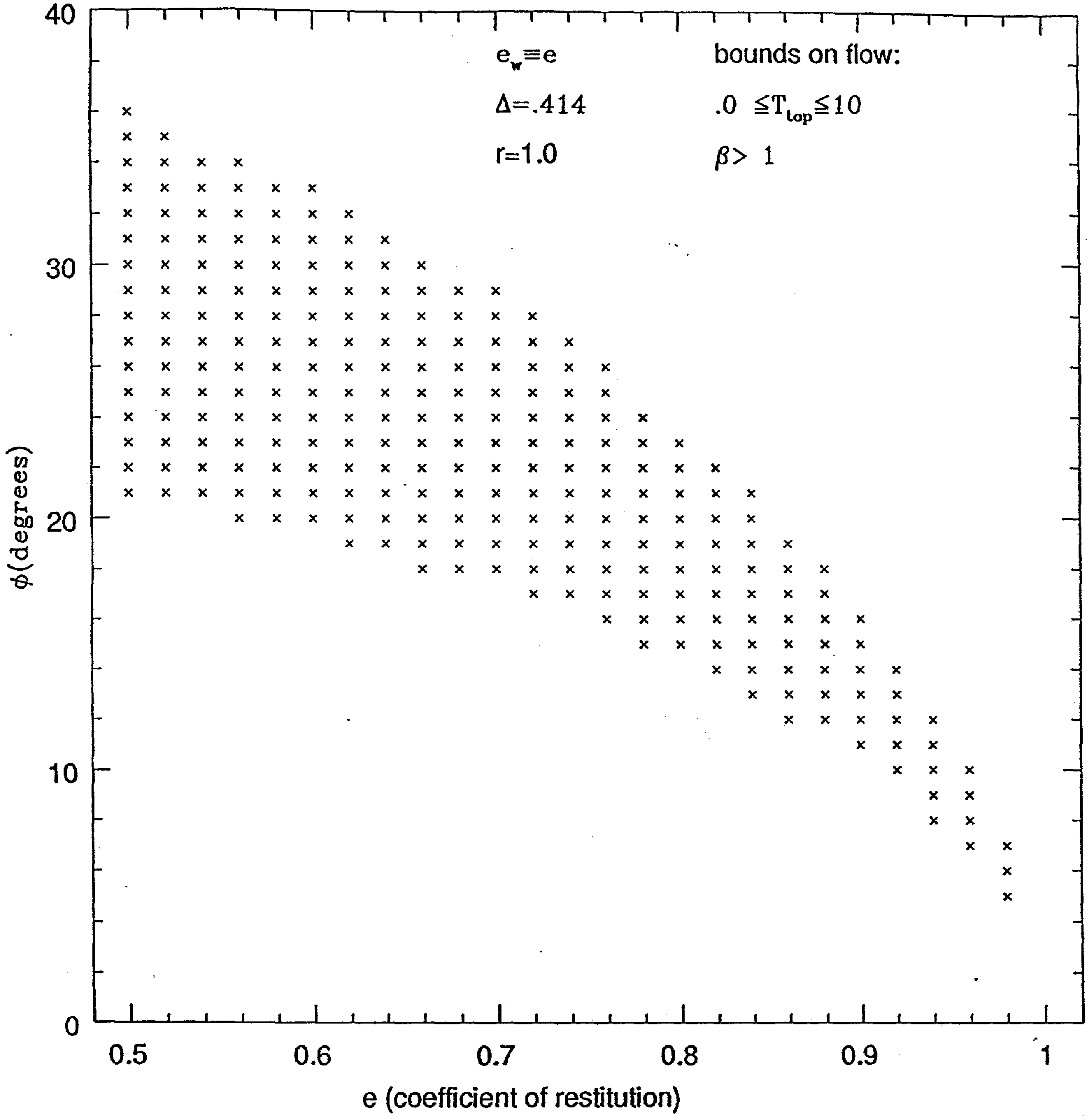

Figure 3.4: The area in the ϕ-e plane in which steady, fully developed, gravity driven flows are possible when r=1, Δ=.414, and $0<e=e_w<1.0$.

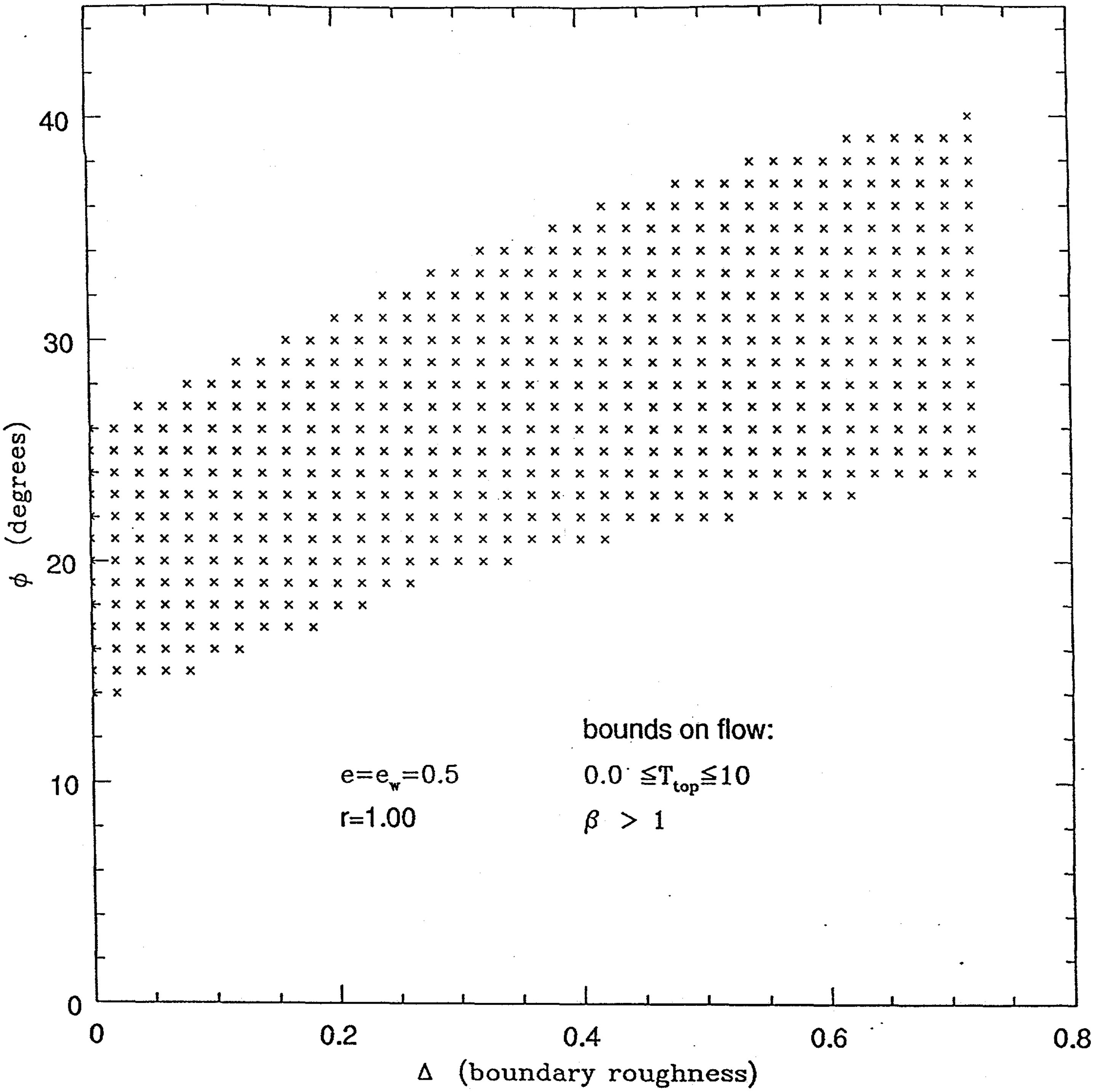

Figure 3.5: The area in the φ-Δ plane in which steady, fully developed, gravity driven flows are possible when r=1, $e=e_w=.5$, and $0<\Delta<.732$.

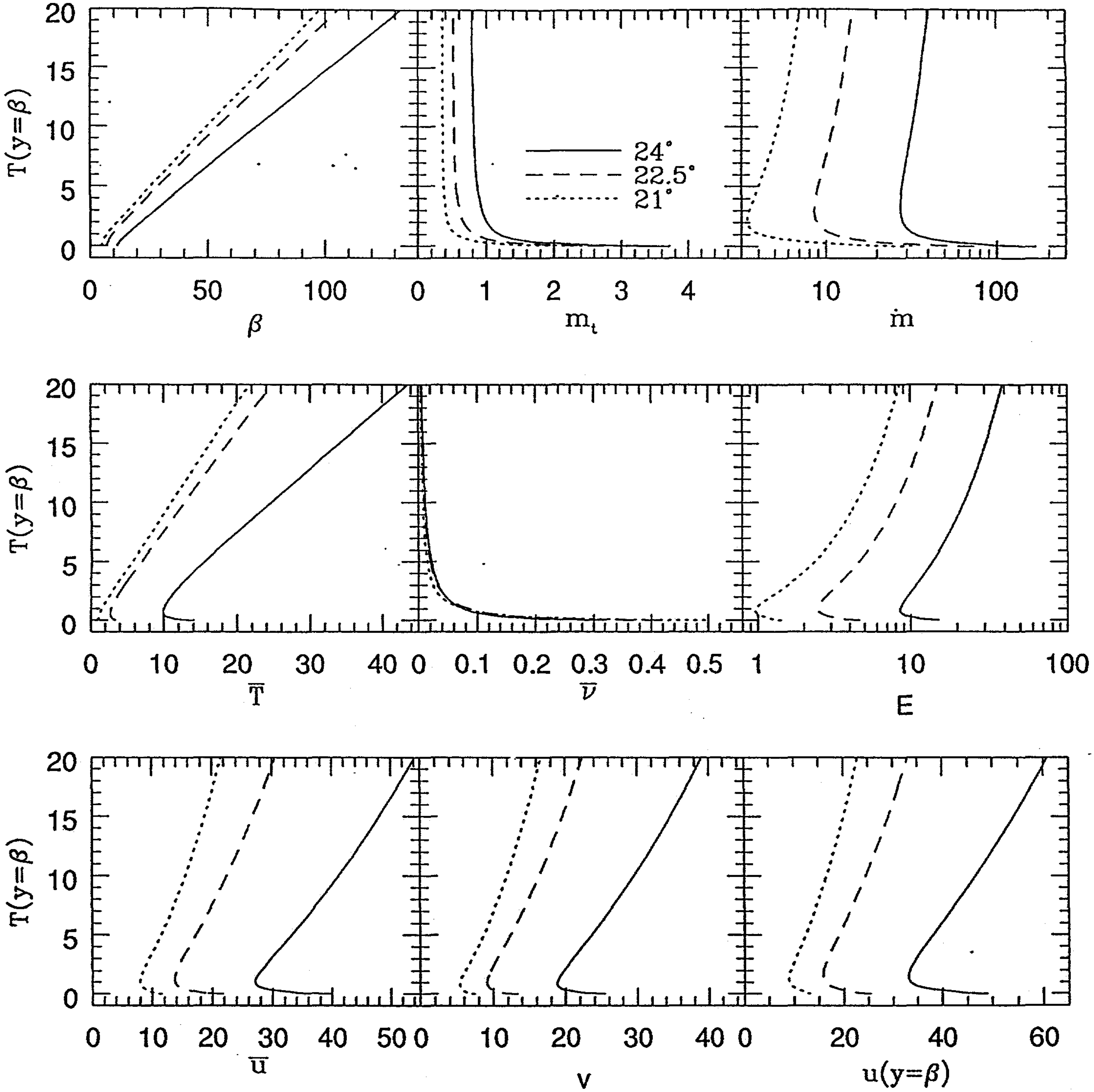

Figure 3.6: The variations of β, m_t, ṁ, $\bar{T}$, $\bar{v}$, E, $\bar{u}$, v, and u(y=β) with T(y=β) for φ=21°, 22.5°, and 24° when r=1, $e=e_w=.5$, and Δ=0.

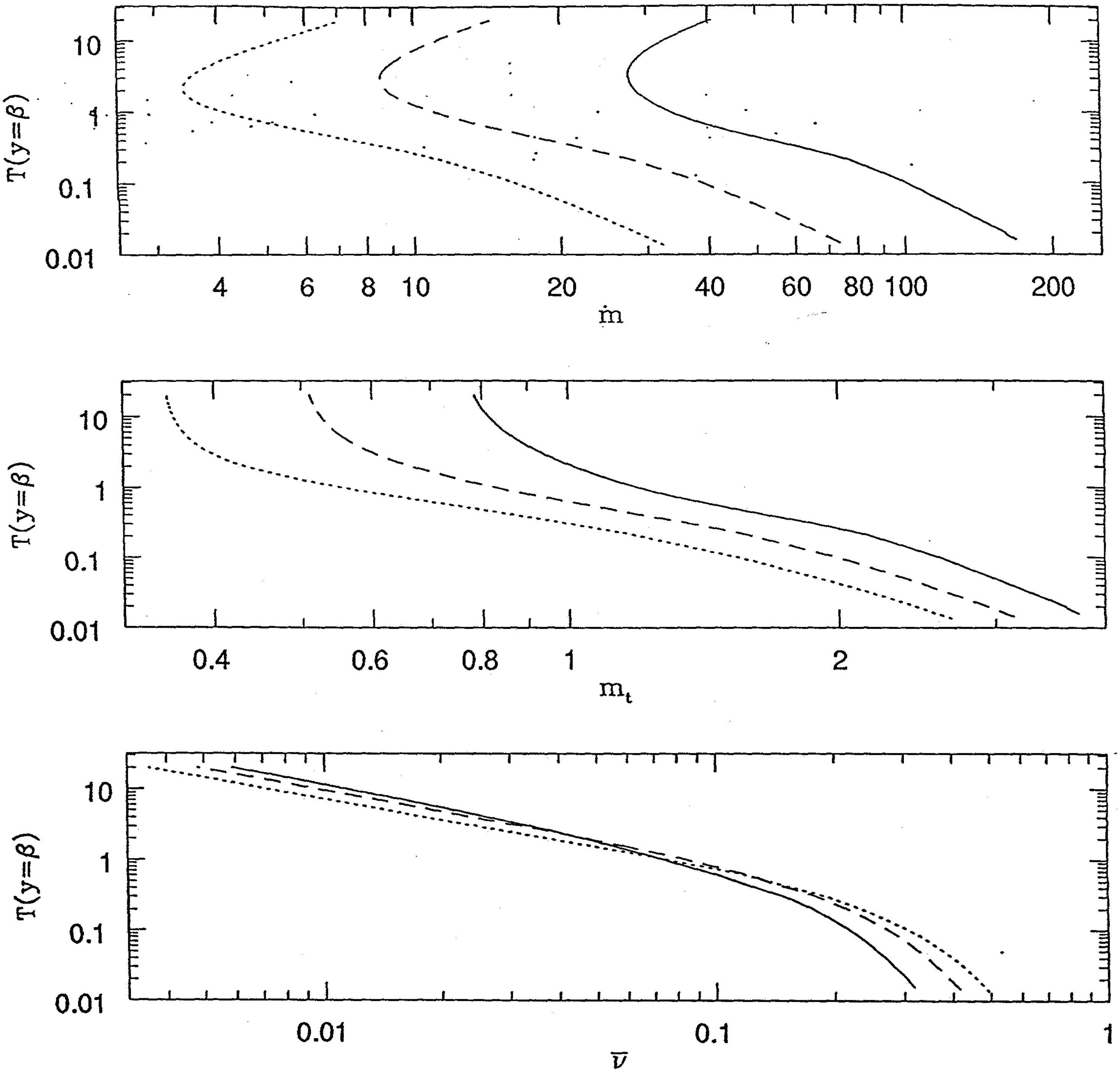

Figure 3.7: The variations of $\dot{m}$, m_t, and $\bar{v}$ with $T(y=\beta)$ for $\phi=21°$, $22.5°$, and $24°$ when $r=1$, $e=e_w=.5$, and $\Delta=0$.

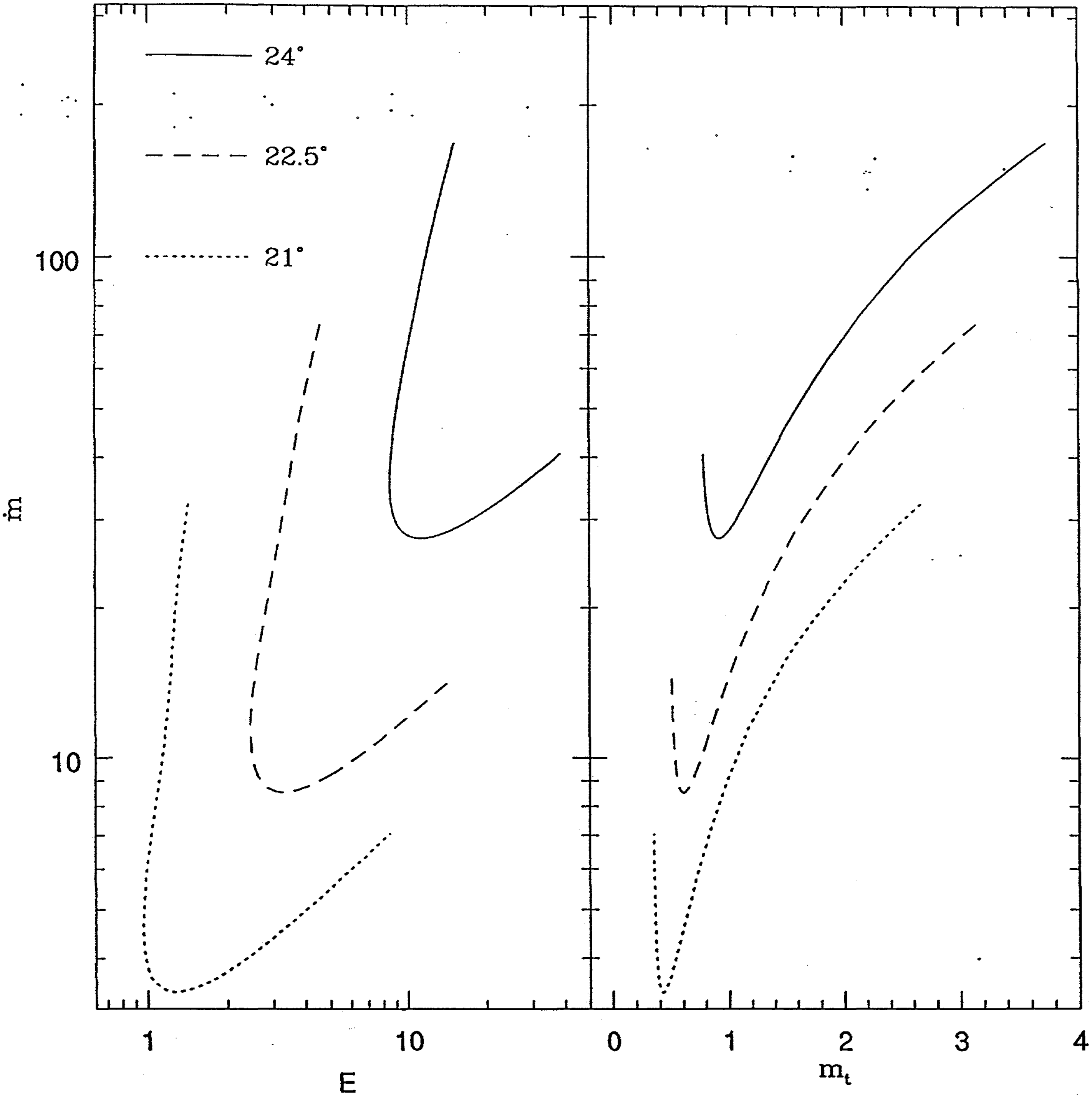

Figure 3.8: The variations of E and m_t with $\dot{m}$ for ϕ=21°, 22.5°, and 24° when r=1, e=e_w=.5, and Δ=0.

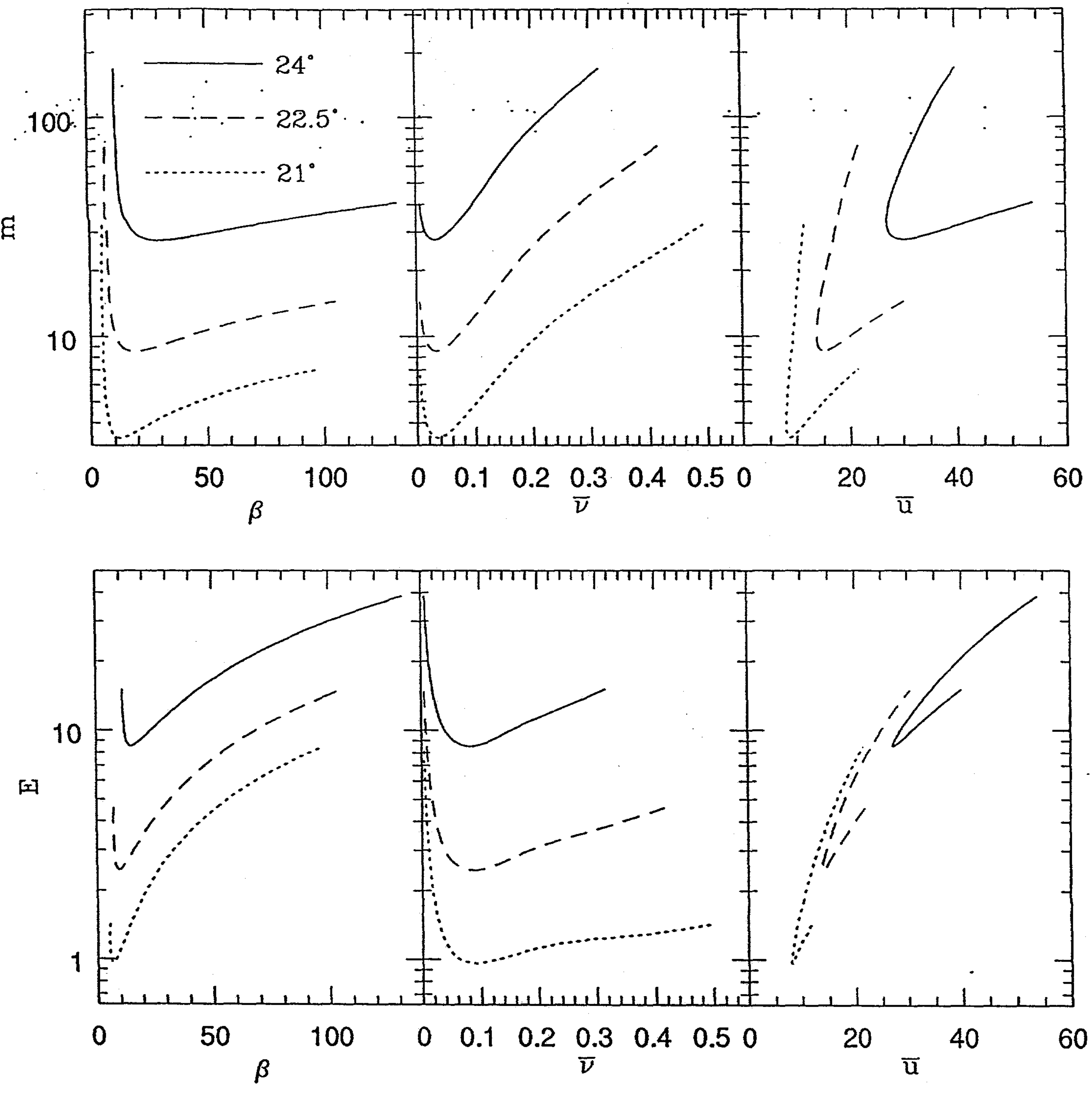

Figure 3.9: The variations of β, $\bar{v}$, and $\bar{u}$ with $\dot{m}$ and E for ϕ=21°, 22.5°, and 24° when r=1, e=e_w=.5, and Δ=0.

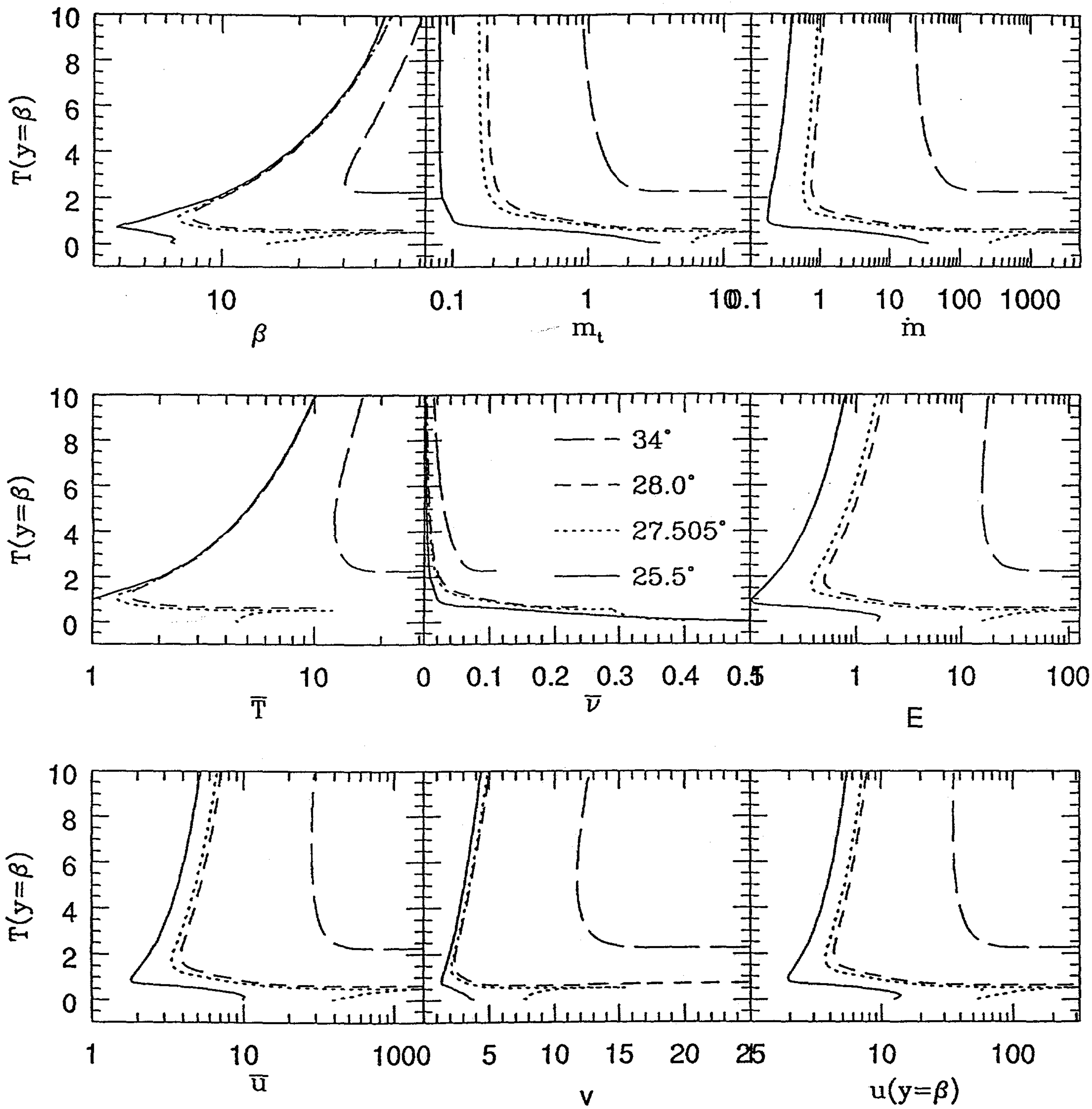

Figure 3.10: The variations of β, m_t, $\dot{m}$, $\bar{T}$, $\bar{v}$, E, $\bar{u}$, v, and $u(y=\beta)$ with $T(y=\beta)$ for $\phi=25.5°$, 27.505°, 28° and 34° when $r=1$, $e=e_w=.5$, and $\Delta=.414$.

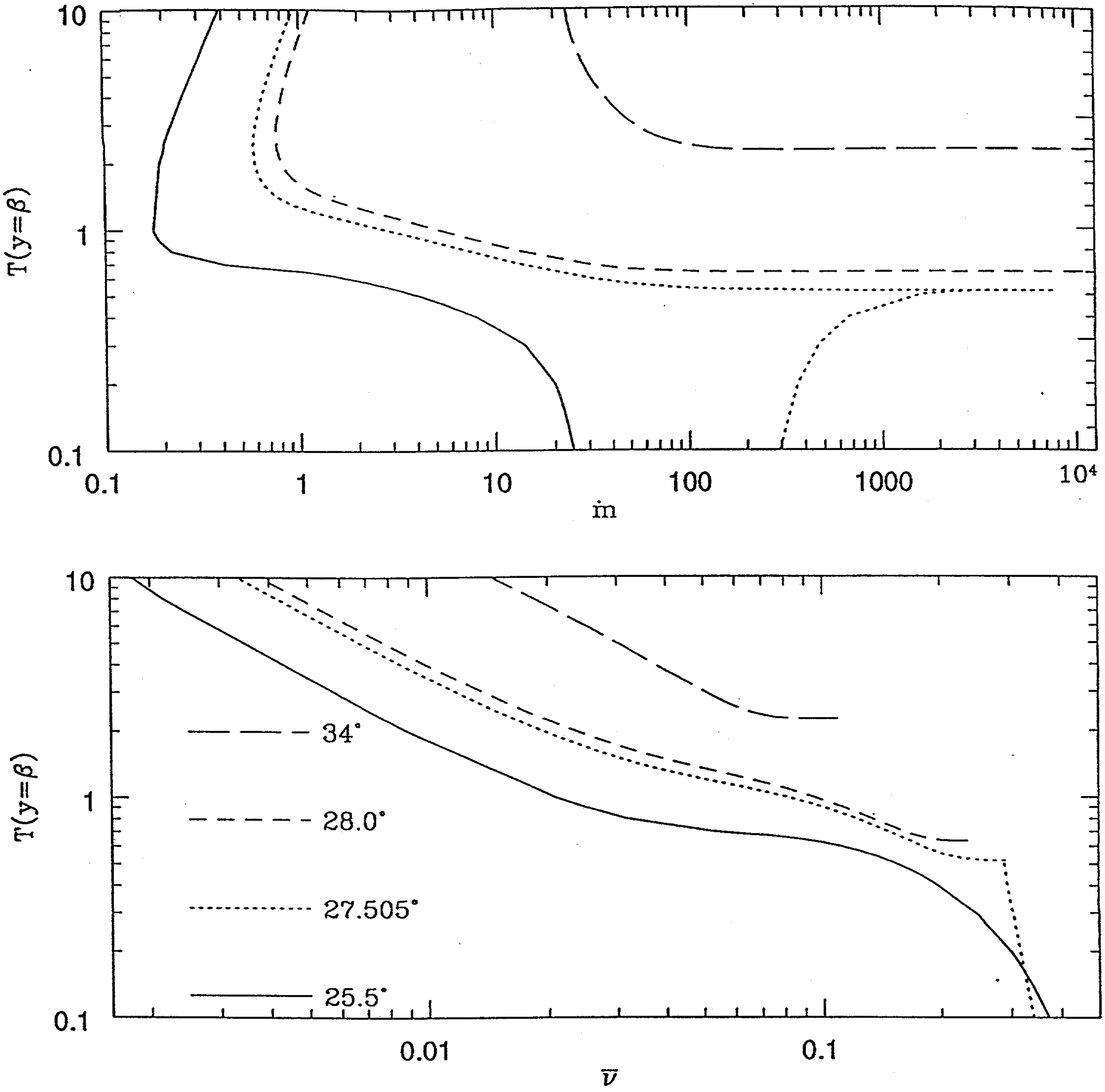

Figure 3.11: The variations of ṁ, and $\bar{\nu}$ with T(y=β) for ϕ=25.5°, 27.505°, 28° and 34° when r=1, $e=e_w=.5$, and Δ=.414.

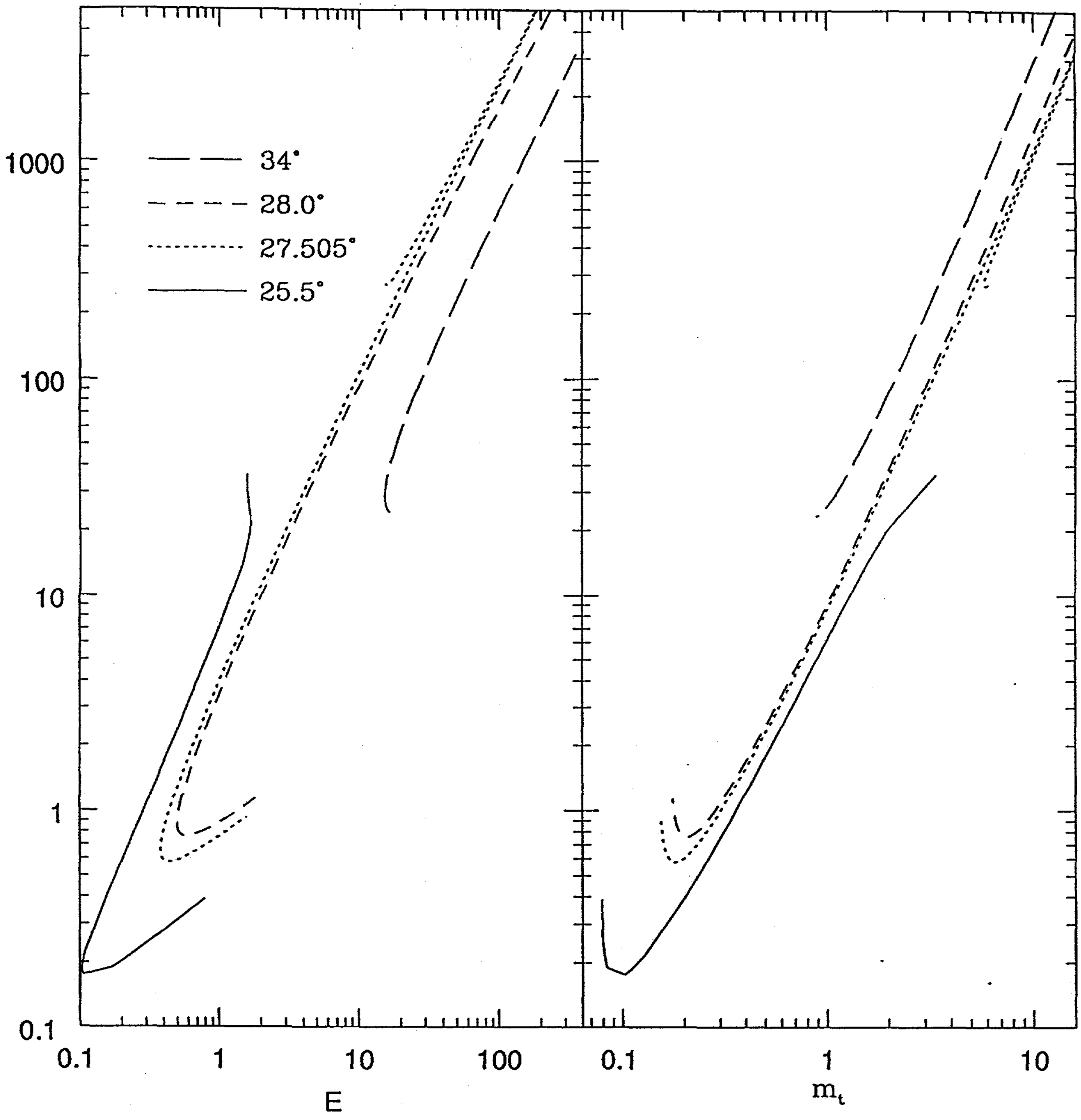

Figure 3.12: The variations of E and m_t with $\dot{m}$ for ϕ=25.5°, 27.505°, 28° and 34° when r=1, e=e_w=.5, and Δ=.414.

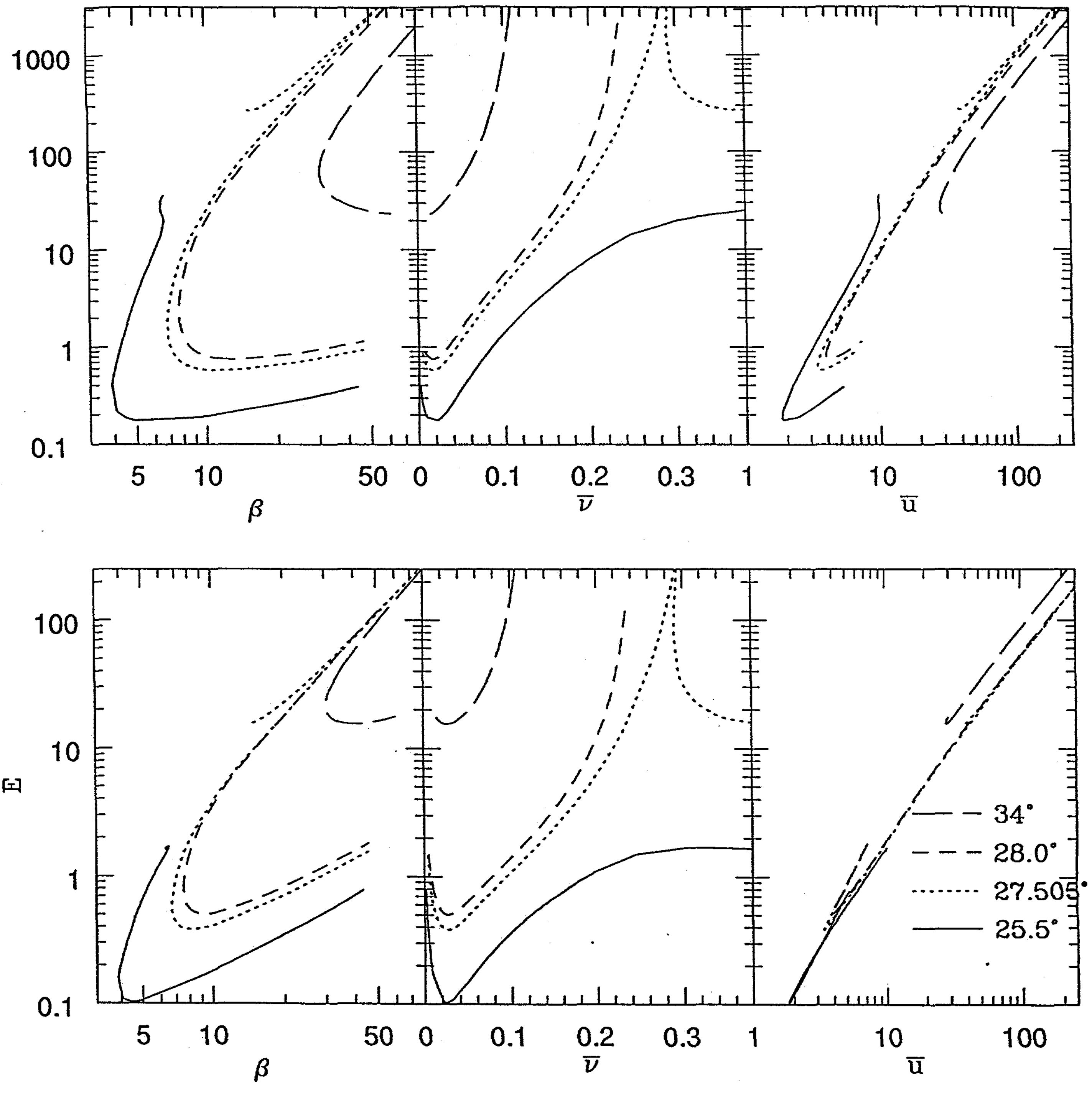

Figure 3.13: The variations of β, $\bar{v}$, and $\bar{u}$ with $\dot{m}$ and E for ϕ=25.5°, 27.505°, 28° and 34° when r=1, e=e_w=.5, and Δ=.414.

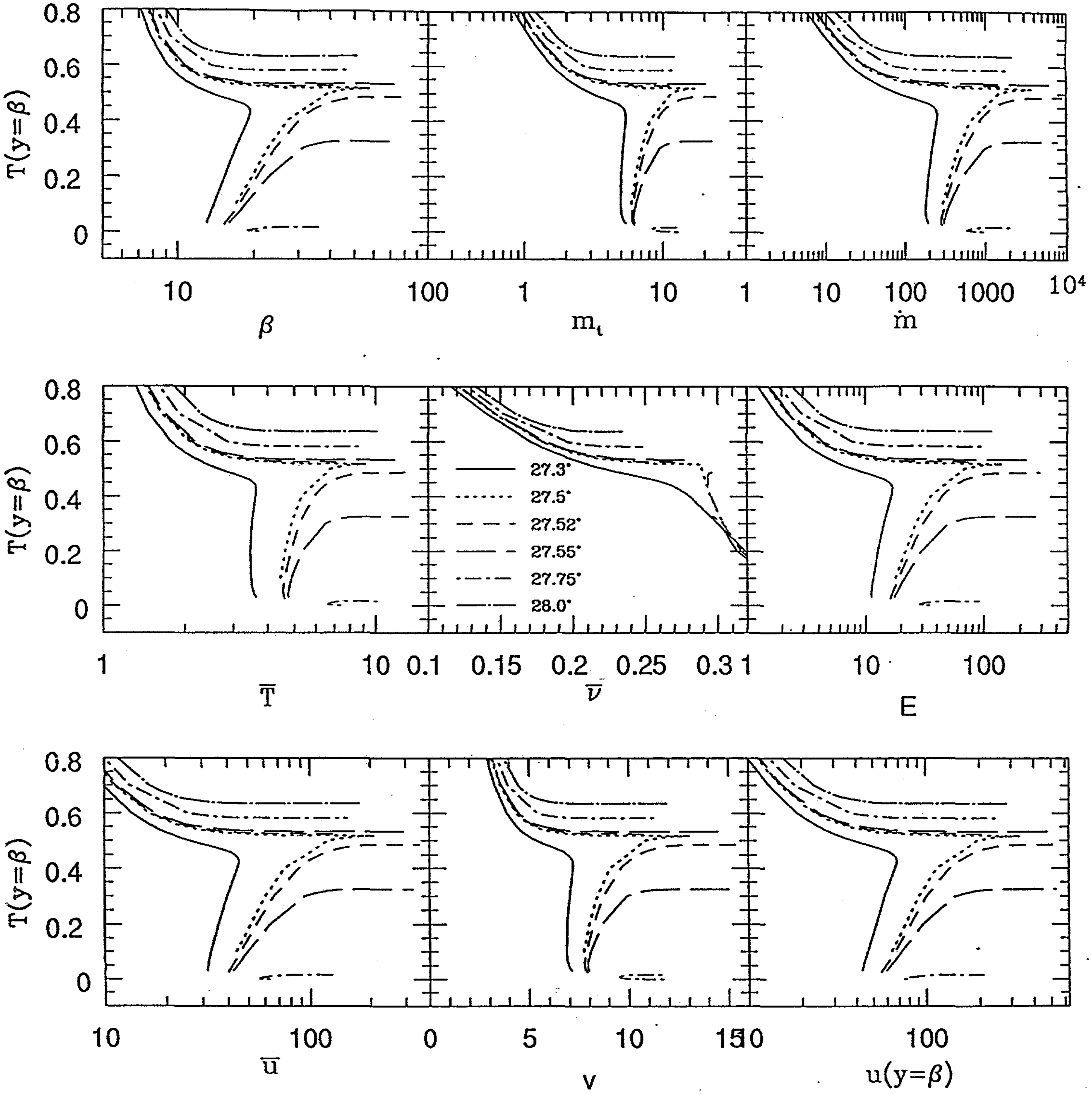

Figure 3.14: The variations of β, m_t, ṁ, $\bar{T}$, $\bar{\nu}$, E, ū, v, and u(y=β) with T(y=β) for φ=27.3°, 27.5°, 27.52° 27.55°, 27.57°, and 28° when r=1, $e=e_w=.5$, and Δ=.414.

$\phi=27.5°$

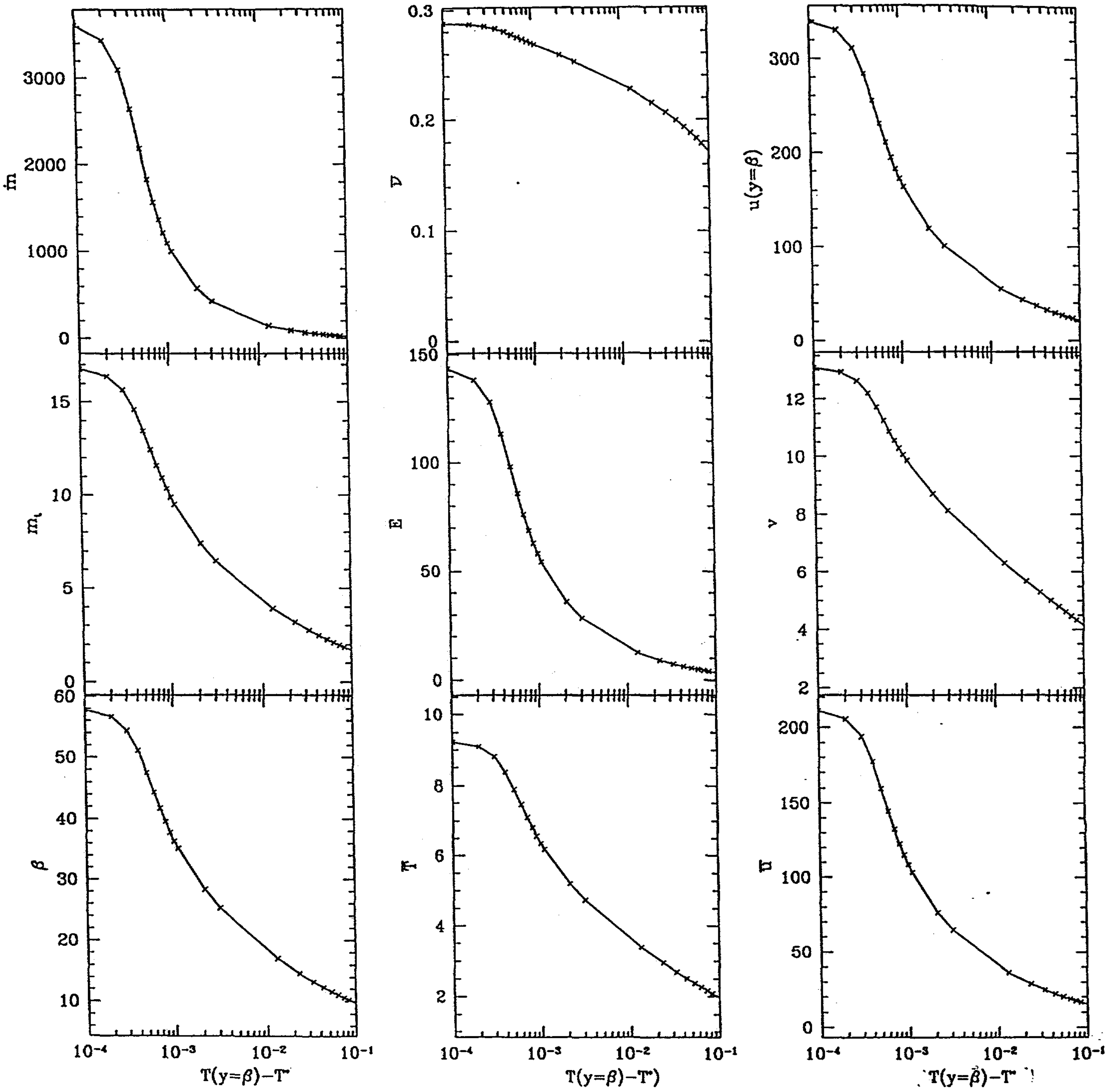

Figure 3.15: The variations of β, m_t, $\dot{m}$, $\bar{T}$, $\bar{v}$, E, $\bar{u}$, v, and $u(y=\beta)$ with $T(y=\beta)$ -T* for ϕ=27.5°, when r=1, e=e_w=.5, and Δ=.414.

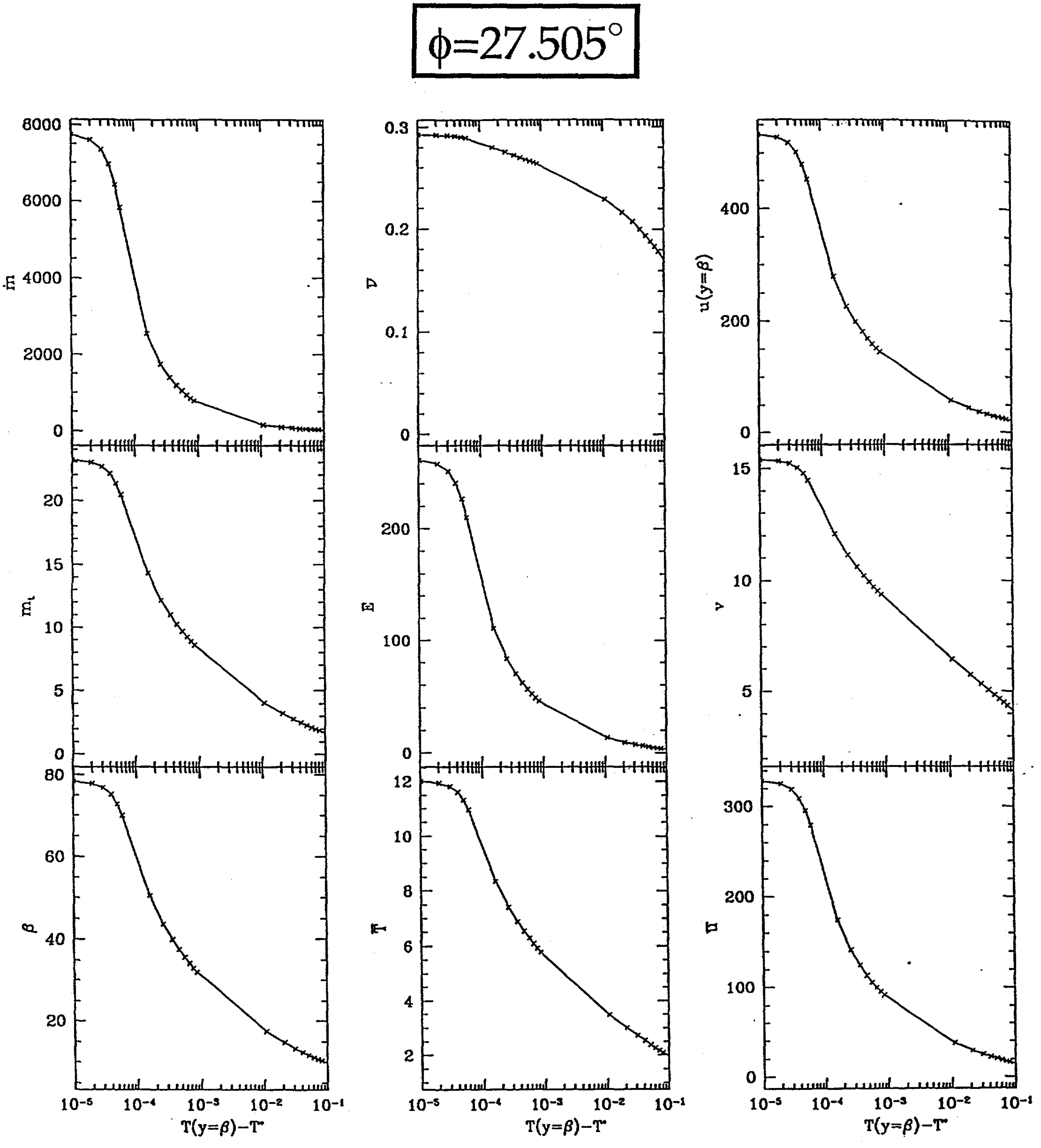

Figure 3.16: The variations of β, m_t, $\dot{m}$, $\bar{T}$, $\bar{v}$, E, $\bar{u}$, v, and $u(y=\beta)$ with $T(y=\beta) - T^*$ for $\phi=27.505°$, when r=1, $e=e_w=.5$, and $\Delta=.414$.

$\boxed{\phi=27.51^\circ}$

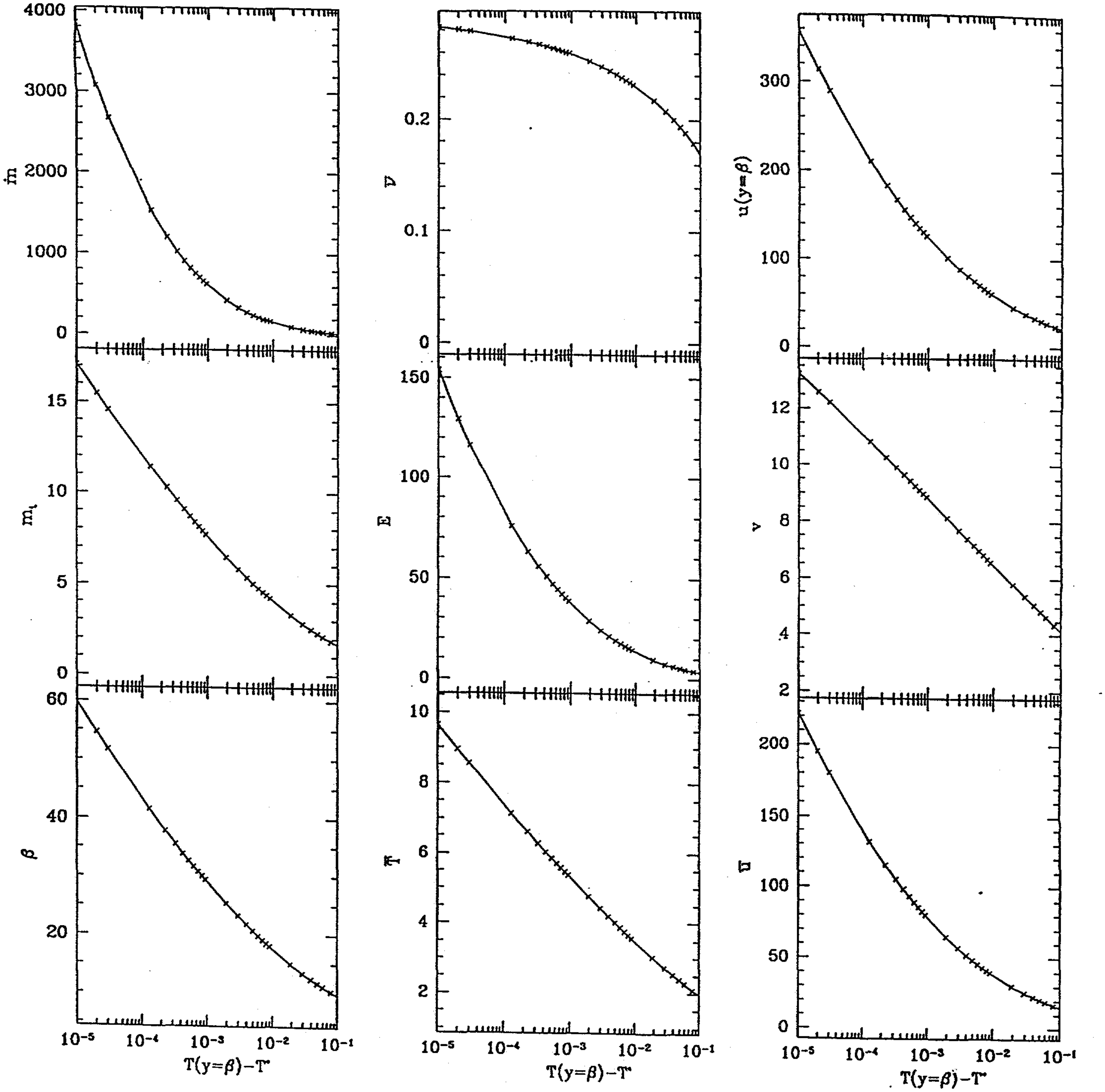

Figure 3.17: The variations of β, m_t, $\dot{m}$, $\bar{T}$, $\bar{v}$, E, $\bar{u}$, v, and u(y=β) with T(y=β) -T* for ϕ=27.51, when r=1, e=e_w=.5, and Δ=.414.

ϕ=27.75°

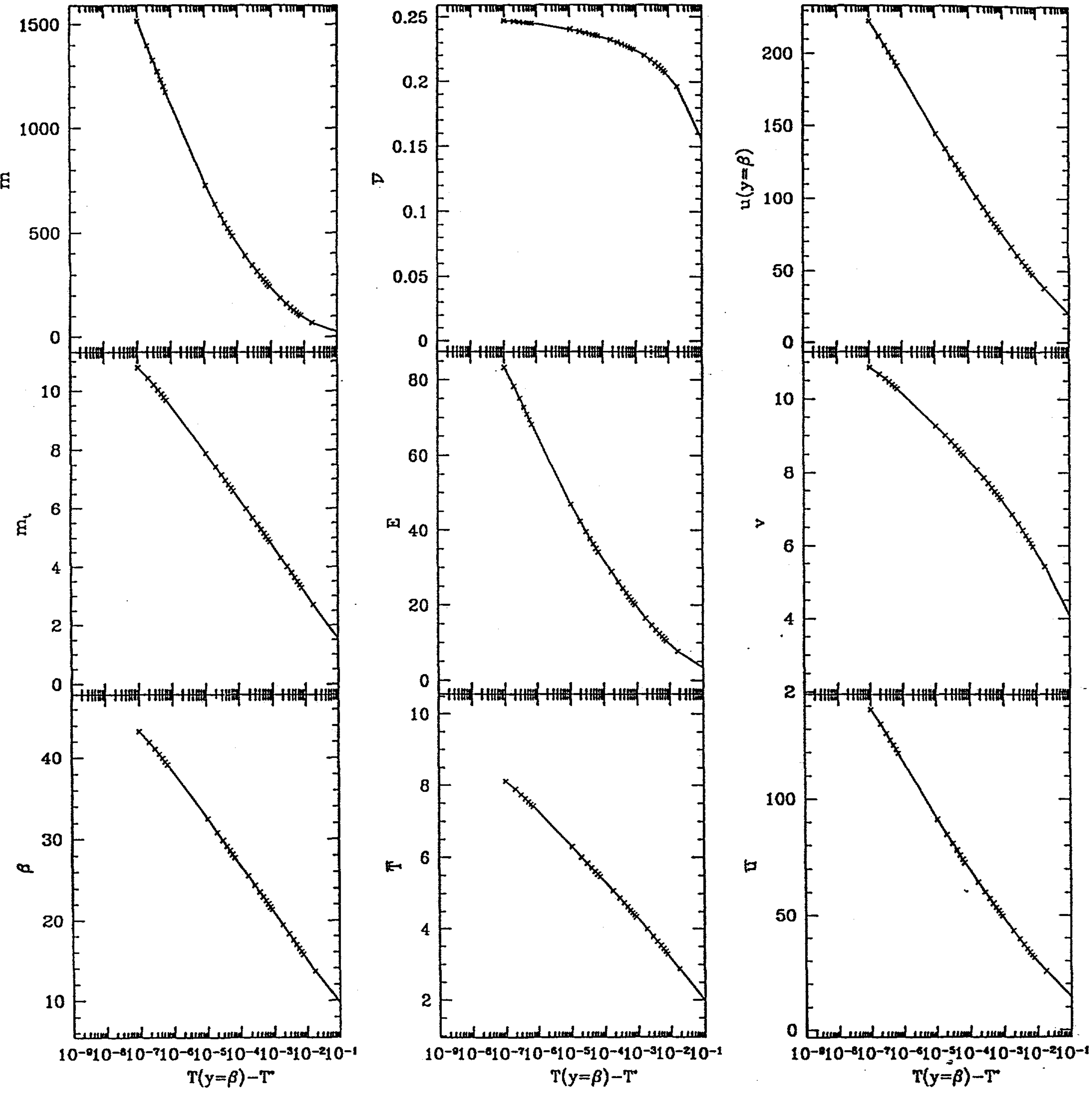

Figure 3.18: The variations of β, m_t, ṁ, $\bar{T}$, $\bar{v}$, E, ū, v, and u(y=β) with T(y=β) -T* for ϕ=27.75°, when r=1, e=e_w=.5, and Δ=.414.

ϕ=28.0°

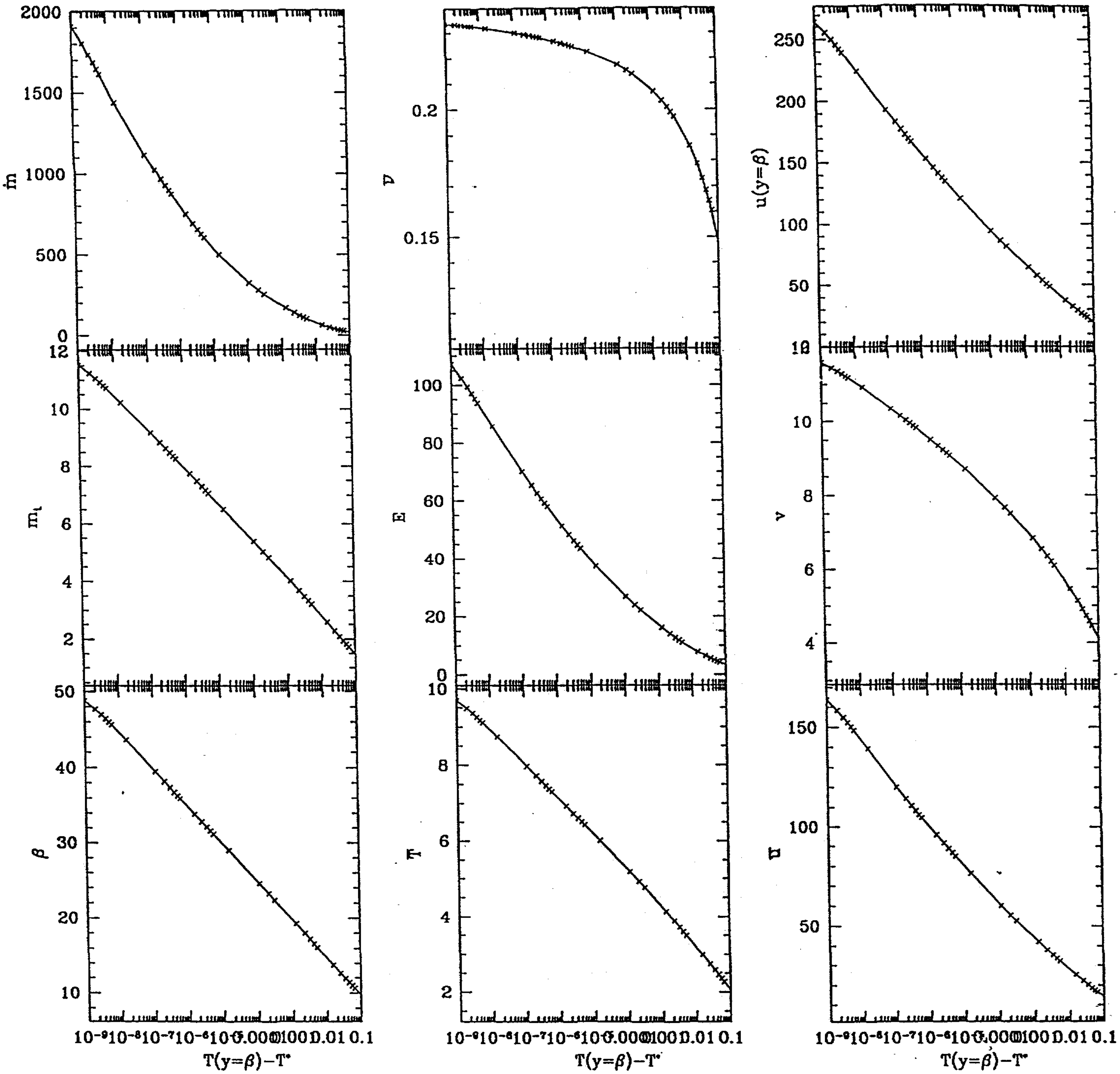

Figure 3.19: The variations of β, m_t, ṁ, $\bar{T}$, $\bar{v}$, E, ū, v, and u(y=β) with T(y=β) -T* for ϕ=28.0°, when r=1, e=e_w=.5, and Δ=.414.

4. VIBRATING BOUNDARIES

4.1 Boundary Conditions

We consider the interaction of a three-dimensional granular flow with an impenetrable boundary that randomly fluctuates about mean velocity **U**. Of particular interest are the mechanisms by which the balance of energy and momentum are satisfied at the flow-boundary interface. Consequently, we focus attention on a parrallelpiped in the flow with two opposite faces of unit area, one of which is coincident with the boundary. In the limit, as the other four sides shrink to zero, the balance of momentum within the parallelpiped requires that

$$\mathbf{M} = \mathbf{P} \cdot \mathbf{N} \quad , \tag{1}$$

where **M** is the rate per unit area at which momentum is transferred to the flow through collision, **P** is the pressure tensor, and **N** is the unit inward normal to the boundary. If F is the rate per unit area of energy supplied by the boundary to the flow due to its fluctuating motion, and D is the corresponding rate at which energy is dissipated through inelastic collisions at the boundary, then in the same limit, the balnce of energy requires that

$$\mathbf{M} \cdot \mathbf{v} + \mathrm{F} - \mathrm{D} = \mathbf{Q} \cdot \mathbf{N} \quad , \tag{2}$$

where **v** is the slip velocity defined as the difference **U-u** between the mean velocity **U** of the boundary and the mean velocity **u** of the flow at the boundary, and **Q** is the energy flux vector. The slip work, **M·v**, is the rate at which work is done by equal tractions acting through velocities that differ by **v**. Thus, the boundary can either supply or absorb fluctuation energy depending on the relative sizes of the slip work **M·v**, the supply rate F, or the dissipation rate D. Even when the boundary does not vibrate (i.e. F=0) and when all interactions between the boundary and the flow particles are dissipative (i.e. D>0), the boundary may actually supply energy to the flow provided that **M·v** exceeds D.

4.2 Transfer Rates

The transfer rates **M**, F, and D depend on boundary geometry and motion. Richman [1993], for example, has determined their forms for bumpy boundaries whose motion was governed by an isotropic Maxwellian velocity distribution function. Under such circumstances, contributions to the total fluctuation energy of the boundary are the same from any three mutually perpendicular components of the boundary's fluctuation velocity. Moreover, it is not possible for the vibratory motion of such boundaries to exert shear stresses on the assemblies with which they interact. Richman and Martin [1993, 1995] improved upon this work by considering boundaries whose fluctuating motion was anisotropic, but restricted their attention to assemblies that experienced no spatial variation of mean velocity at the boundary. Here, we will calculate the transfer rates when the boundaries fluctuate anisotropically *and* when the flows experience gradients of mean velocity at the boundary. Consequently, we will calculate **M**, F, and D based on an anisotropic boundary velocity distribution function and a flow particle velocity distribution function that involves corrections to the Maxwellian due to spatial variations of the mean flow velocity.

The boundary we focus attention on is a flat surface to which hemispheres of diameter d are randomly attached at a disatance s apart. If σ is the flow-particle diameter, then the dimensionless quantities that describe the geometry of the boundary are $r=\sigma/d$ and $\Delta=s/d$. The bumpiness of the boundary is measured by the angle θ formed by the line directed from the center of a hemispherical bump and the center of a flow particle in contact with that and a neighboring bump. As θ increases, the boundary becomes more effective at transferring momentum in directions parrallel to its flat surface; in this sense it becomes "rougher." The angle q is related to the geometric parameters r and Δ according to the relation $\sin\theta=(1+\Delta)/(1+r)$.

The dynamics of a collision at the boundary are described in terms of the pre-collisional velocities **c** of the flow particle and ψ of the boundary particle, the unit vector **k** directed from the center of the boundary particle to the center of the flow particle at impact, and the coefficient of restitution e_W that characterizes the energy dissipated when smooth particles collide. If the velocity of the wall particle is unaffected by the collision, then in terms of the relative velocity $\mathbf{g}\equiv\psi-\mathbf{c}$, the change in linear momentum experienced by the flow particle is

$$m(\mathbf{c}^* - \mathbf{c}) = m(1+e_w)(\mathbf{g}\cdot\mathbf{k})\mathbf{k} \quad , \tag{3}$$

where m is the mass of the flow particle and **c*** is the post-collisional velocity of the flow particle. The corresponding change in energy is

$$\frac{m}{2}(\mathbf{c}^*\cdot\mathbf{c}^* - \mathbf{c}\cdot\mathbf{c}) = m(1+e_w)(\mathbf{g}\cdot\mathbf{k})\left[(\mathbf{U}\cdot\mathbf{k}) + (\Psi\cdot\mathbf{k}) - \frac{1}{2}(1-e_w)(\mathbf{g}\cdot\mathbf{k})\right] \quad , \tag{4}$$

where $\Psi\equiv\psi-\mathbf{U}$ is the fluctuation velocity of the boundary particle.

The statistics associated with collisions between wall and flow particles are governed by two velocity distribution functions: $f(\mathbf{c},\mathbf{r})$, which describes the flow particle velocities; and $p(\psi)$, which gives the probability per unit volume $d\psi\equiv d\psi_1 d\psi_2 d\psi_3$ in velocity space that any particle will have velocity ψ within the range $d\psi$.

The motion of the boundary is described by its mean velocity U and its full second moment B of fluctuation velocity. These are analogous to u and K within the flow and are calculated according to

$$\mathbf{U} = \int \psi\, p(\psi) d\psi \quad , \tag{5}$$

and

$$\mathbf{B} = \int (\Psi \otimes \Psi)\, p(\psi) d\psi \quad , \tag{6}$$

in which the integrations are over all velocities.

At the instant of impact, the center of the boundary particle is located at **x**, and the distance between the centers of the two particles is $\bar{\sigma} \equiv (\sigma + d)/2$ (where σ is the diameter of the flow particle and d is the diameter of the hemispherical bump). The frequency of collisions per unit area of flat wall that involve flow particles with velocites **c** in the range d**c** and wall particles with velocities ψ in the range $d\psi$, and occur within an element of solid angle d**k** centered about **k** on the surface of the wall particle is

$$\frac{\chi}{\pi \sin^2\theta} f(\mathbf{c}, \mathbf{x} + \bar{\sigma}\mathbf{k}) p(\psi)(\mathbf{g} \cdot \mathbf{k}) d\mathbf{k} d\mathbf{c} d\psi \quad . \tag{7}$$

Here, $(\mathbf{g} \cdot \mathbf{k}) > 0$ for a collision to occur, and the factor χ accounts for the effects of excluded volume and the shielding of flow particles from wall particles by other flow particles. Excluded volume effects account for the space occupied by both the flow particles and the the boundary particles. The extent of shielding depends on the motion of the flow particles, the motion of the boundary, and the arrangement of the boundary particles. Consequently, we anticipate that χ will at least depend on v and T at the boundary, as well as θ and **B**.

The transfer rates M, F, and D are statistical averages of the appropriate change per collision weighted by the collision frequency (7). According to equation (3) **M** is the weighted average of $m(1+e_w)(\mathbf{g} \cdot \mathbf{k})\mathbf{k}$. According to the last two terms on the right-hand-side of equation (4), F and D are the weighted averages of $m(1+e_w)(\mathbf{g} \cdot \mathbf{k})(\Psi \cdot \mathbf{k})$ and $m(1-e_w^2)(\mathbf{g} \cdot \mathbf{k})^2/2$. These may be written more compactly in integral form:

$$\begin{Bmatrix}\mathbf{M}\\ \mathbf{F}\\ \mathrm{D}\end{Bmatrix} = \frac{m(1+e_w)}{\pi\sin^2\theta}\int \chi \begin{Bmatrix}(\mathbf{g}\cdot\mathbf{k})\mathbf{k}\\ (\mathbf{g}\cdot\mathbf{k})(\Psi\cdot\mathbf{k})\\ \tfrac{1}{2}(1-e_w)(\mathbf{g}\cdot\mathbf{k})^2\end{Bmatrix} f(\mathbf{c},\mathbf{x}+\bar{\sigma}\mathbf{k})p(\psi)(\mathbf{g}\cdot\mathbf{k})d\mathbf{k}d\mathbf{c}d\psi \quad , \qquad (8)$$

where the velocity integrations are carried out over all velocities such that $(\mathbf{g}\cdot\mathbf{k})>0$, and the $\mathbf{k}$-integration is a surface integral over the area of the boundary particle that is accesible to colliding flow particles.

In order to carry out the averaging procedure, we must first write down the distribution functions $f(\mathbf{c},\mathbf{r})$ and $p(\psi)$. Here we assume that f is the corrected Maxwellian introduced by Grad [1949]:

$$f(\mathbf{c},\mathbf{r}) = \frac{n}{(2\pi T)^{3/2}}\left[1+\frac{1}{2T^2}\mathbf{C}\cdot\mathbf{K}\cdot\mathbf{C}\right]\exp\left\{\frac{-\mathbf{C}\cdot\mathbf{C}}{2T}\right\} \quad , \qquad (9)$$

in which n is the number density of flow particles, T is the granular temperature, $\mathbf{C}$ is the fluctuation velocity $\mathbf{c}$-$\mathbf{u}$ of the flow particles, $\mathbf{K}$ is the deviatoric part of the second moment of $\mathbf{C}$, and all mean fields are evaluated at $\mathbf{r}$. For sheared assemblies of nearly elastic spheres, Jenkins and Richman [1985] have shown that $\mathbf{K}$ is small compared to T and may be approximated in terms of velocity gradients by

$$\frac{1}{2T}\mathbf{K} = \frac{-2^{1/2}\sigma A(v)}{(\pi T)^{1/2}}\mathbf{D} \quad , \qquad (10)$$

where v is the solid volume fraction, $A(v)\equiv\pi[1+5/8G]/2^{1/2}12$, $G\equiv v(2-v)/2(1-v)^3$, and $\mathbf{D}$ is the deviatoric part of the strain rate $\mathbf{D}$. Under these circumstances, the largest corrections to the Maxwellian that we have neglected are proportional to gradients of temperature and solid fraction. In addition, we take $p(\psi)$ as the anisotropic Maxwellian:

$$p(\psi) = \frac{1}{(8\pi^3 B)^{1/2}}\exp\left\{\frac{-1}{2}\Psi\cdot\mathbf{B}^{-1}\cdot\Psi\right\} \quad , \qquad (11)$$

where B is the determinant of $\mathbf{B}$. When B is isotropic, $p(\psi)$ reduces to the simple Maxwellian employed by Richman [1993]. When the velocity gradients vanish, $f(\mathbf{c},\mathbf{r})$ reduces to the simple Maxwellian employed by Richman and Martin [1993, 1995].

Because the corrected Maxwellian (9) for f is the sum of two terms (i.e. the Simple Maxwellian and its correction due to velocity gradients), each transfer rate can be decomposed into two corresponding contributions. The contribution from the simple Maxwellian contains the lowest order approximation to each rate, and the contribution due to velocity gradients is a correction to each. In this manner, we write $\mathbf{M}=\mathbf{M}^0+\mathbf{M}^c$, $F=F^0+F^c$, and $D=D^0+D^c$, where the superscripts "0" and "c" denote the contributions from the first and second terms in f, respectively. If the integrations over velocites c and y in averages (8) are carried out first, then the intermediate results can be written compactly in terms of the quantity

$$\Phi=\frac{\mathbf{v}\cdot\mathbf{k}}{[2T(\mathbf{k}\cdot\mathcal{B}\mathbf{k})]^{1/2}} \quad , \tag{12}$$

where $\mathcal{B}\equiv\delta+\mathbf{B}/T$ and both T and $\mathbf{v}\equiv\mathbf{U}-\mathbf{u}$ are evaluated at $\mathbf{x}+\bar{\sigma}\mathbf{k}$. The resulting integral expression for the first contribution to the rate at which momentum is supplied to the flow is

$$\mathbf{M}^0=\frac{(1+e_w)}{\pi^{3/2}\sin^2\theta}\int\rho\chi T(\mathbf{k}\cdot\mathcal{B}\mathbf{k})\mathbf{k}\left[\pi^{1/2}\left(\tfrac{1}{2}+\Phi^2\right)\mathrm{erfc}(-\Phi)+\Phi\exp(-\Phi^2)\right]d\mathbf{k} \quad , \tag{13}$$

where the mass density ρ, the granular temperature T, and the factor χ are evaluated at $\mathbf{x}+\bar{\sigma}\mathbf{k}$. The corresponding lowest order expressions for F^0 and D^0 are

$$F^0=\frac{2^{1/2}(1+e_w)}{\pi^{3/2}\sin^2\theta}\int\rho\chi T^{3/2}(\mathbf{k}\cdot\mathcal{B}\mathbf{k})^{1/2}(\mathbf{k}\cdot\mathcal{B}\mathbf{k}-1)\left[\pi^{1/2}\Phi\,\mathrm{erfc}(-\Phi)+\exp(-\Phi^2)\right]d\mathbf{k} \quad , \tag{14}$$

and

$$D^0=\frac{(1-e_w{}^2)}{2^{1/2}\pi^{3/2}\sin^2\theta}\int\rho\chi T^{3/2}(\mathbf{k}\cdot\mathcal{B}\mathbf{k})^{3/2}\left[\pi^{1/2}\Phi\left(\tfrac{3}{2}+\Phi^2\right)\mathrm{erfc}(-\Phi)+(1+\Phi^2)\exp(-\Phi^2)\right]d\mathbf{k}. \tag{15}$$

To calculate $\mathbf{M}^0$, F^0, and D^0, it remains to carry out the **k**-integrations (13), (14), and (15) over that portion of a wall particle that is accessible to flow particles.

In principle, we must also determine the contribution to each transfer rate from the correction term in equation (9) for f. However, we are only interested in calculating **M**, F, and D to within errors consistent with the assumptions used by Jenkins and Richman [1985] to derive their constitutive theory for nearly elastic spheres. For example, momentum balance (1) demonstrates that the rate of momentum **M** supplied to the flow must balance the pressure tensor P at the boundary. According to the constitutive theory of Jenkins and Richman, the pressure tensor includes both a lowest order contribution (i.e. it isotropic piece) and a first order correction (i.e., its deviatoric piece due to velocity gradients). Consequently, in order to maintain consistency with the constitutive theory, we must include the first order correction $\mathbf{M}^c$ to $\mathbf{M}$. After carrying out the c and ψ integrations, we obtain the integral expression

$$\mathbf{M}^c = \frac{(1+e_w)}{2\pi \sin^2\theta} \int \rho\chi \mathbf{k}\,(\mathbf{k}\cdot\mathbf{K}\cdot\mathbf{k})\,\mathrm{erfc}(-\Phi)\,d\mathbf{k} \quad , \tag{16}$$

where all mean fields are evaluated at $\mathbf{x}+\bar{\sigma}\mathbf{k}$. In addition, we must also include the first order correction to $\mathbf{M}^0$ from a Taylor series of the mean fields about a common location $\mathbf{x}+\bar{\sigma}\mathbf{N}$.

By contrast, energy balance (2) demonstrates that the competing effects of $\mathbf{M}\cdot\mathbf{v}+F-D$ must balance the energy flux $\mathbf{Q}\cdot\mathbf{N}$ normal to the boundary. However, the constitutive relation for the energy flux derived by Jenkins and Richman [1985] for the energy includes only lowest order contributions (due to the presence of temperature gradients). Consequently, to adequately approximate F and D it is necessary to only calculate the lowest order contributions F^0 and D^0.

In order to write down the results of the k-integrations (13), (16), (14), and (15) for $\mathbf{M}^0$, $\mathbf{M}^c$, F^0, and D^0, we introduce a an x_1-x_2-x_3 Cartesian coordinate system in which the unit inward normal N points in the $\pm x_2$-direction, and the unit tangent vectors τ and $\mathbf{t}$ point in the $\pm x_1$- and x_3-directions, respectively. We also introduce a spherical coordinate system in which ξ is the angle between N and the line from the center of the wall particle to the center of the flow particle at impact, and η is the angle between the projection of the line of centers onto the τ-$\mathbf{t}$ plane and the τ-direction. In terms of these quantities, dk is equal to $\sin\xi d\xi d\eta$ and the k-integrations are on ξ from 0 to θ, and on η from 0 to 2π.

In this system, the components of the second moment of boundary fluctuation velocity are

$$\mathbf{B} = \begin{bmatrix} V_1^2 & B_{12} & B_{13} \\ B_{21} & V_2^2 & B_{23} \\ B_{31} & B_{32} & V_3^2 \end{bmatrix} \quad . \tag{17}$$

In what follows, we consider circumstances in which $V_1^2=V_3^2$, the off-diagonal components of $\mathbf{B}$ are small compared to its diagonal components, and both the slip velocity $\mathbf{v}$ and the change in velocity $\sigma\nabla\mathbf{u}$ are small compared to the square root $T^{1/2}$ of the granular temperature. We then expand the integrands in equations (13) through (16) in Taylor series about $\mathbf{x}+\bar{\sigma}\mathbf{N}$ with respect to these small quantities.

Under these circumstances, it is possible to carry out the **k**-integrations in closed form. The resulting approximations for **M**, F, and D may be written in terms of the following quantities: the dimensionless ratio

$$R \equiv \frac{V_2^2 - V_1^2}{T + V_1^2} \quad , \tag{18}$$

and the functions of R and θ defined by

$$K(R,\theta) \equiv (1+R\cos^2\theta)^{3/2}\cos\theta - (1+R)^{3/2} \quad , \tag{19}$$

$$I(R,\theta) \equiv \begin{cases} \dfrac{1}{\sqrt{R}}\left[\sinh^{-1}\sqrt{R} - \sinh^{-1}(\sqrt{R}\cos\theta)\right] & R>0 \\ \\ \dfrac{1}{\sqrt{-R}}\left[\sin^{-1}\sqrt{-R} - \sin^{-1}(\sqrt{-R}\cos\theta)\right] & R<0 \end{cases} \quad , \tag{20}$$

$$J(R,\theta) \equiv (1+R\cos\theta)^{1/2}\cos\theta - (1+R)^{1/2} - I(R,\theta) \quad , \tag{21}$$

$$X(R,\theta) \equiv \frac{2}{15R^2}\left[(1+R\cos^2\theta)^{3/2}(3R\cos^2\theta-2) - (1+R)^{3/2}(3R-2)\right] \quad , \tag{22}$$

$$Y(R,\theta) \equiv X(R,\theta) - \frac{2}{3R}\left[(1+R\cos^2\theta)^{3/2} - (1+R)^{3/2}\right] \quad , \tag{23}$$

and

$$H(R,\theta) \equiv (1+R)^{1/2}(5+2R) - (1+R\cos^2\theta)^{1/2}(5+2R\cos^2\theta)\cos\theta \quad . \tag{24}$$

When the collisions between boundary and flow particles are nearly elastic, e_w is close to unity and the approximate expression for the components of **M** is:

$$M_i = \rho\chi\left\{\left[(V_2^2+T) + \frac{1}{2}(V_1^2-V_2^2)\sin^2\theta\right] N_i + \frac{\sin^2\theta}{2}[(\mathbf{t}\cdot\mathbf{B}\cdot\mathbf{N})t_i + (\tau\cdot\mathbf{B}\cdot\mathbf{N})\tau_i]\right.$$

$$+ \frac{(T+V_1^2)^{1/2}}{(2\pi)^{1/2}R\sin^2\theta}\left[K(R,\theta) - \frac{(1+4R)}{2}J(R,\theta)\right]$$

$$\left.\frac{\bar{\sigma}2^{1/2}}{\pi}\frac{\partial u_k}{\partial x_j}[V_1^2+T]^{1/2}(\mathcal{I}_{ijk}+\mathcal{I}_{ik}N_k) + \frac{sAT^{1/2}}{\bar{\sigma}}\left(I_{ijk}+\frac{2}{3}N_i\delta_{kj}\right)\right\} \qquad (25)$$

where all the mean fields are evaluated at $\mathbf{x}+\bar{\sigma}\mathbf{N}$. The tensors $\mathcal{I}_{ijk}$, $\mathcal{I}_{ik}$, and I_{ijk}, which arise naturally from the averaging procedure are given by,

$$\mathcal{I}_{ik} = \sin^{-2}\theta\left\{\frac{1}{2R}\left[K(R,\theta) - \frac{(1+4R)}{2}J(R,\theta)\right](t_it_k+\tau_i\tau_i) + \frac{(J(R,\theta)-2R)}{2R}N_iN_k\right\} , \qquad (26)$$

$$\mathcal{I}_{ijk} = \sin^{-2}\theta\ \{(2X(R,\theta)N_iN_jN_k$$

$$- Y(R,\theta)\ [(t_it_k+\tau_i\tau_i)N_i + (t_it_k+\tau_i\tau_k)N_j + (t_it_j+\tau_i\tau_j)N_k]\ )\} \quad , \qquad (27)$$

and

$$I_{ijk} = (\sin^2\theta -2)N_iN_jN_k - \frac{\sin^2\theta}{2}[(t_it_k+\tau_i\tau_i)N_i + (t_it_k+\tau_i\tau_k)N_j + (t_it_j+\tau_i\tau_j)N_k] \ . \qquad (28)$$

Expression (25) for **M** differs from that obtained by Richman and Martin [1993] because it includes the influence of velocity gradients. There are two terms proportional to velocity gradients. The first term is multiplied by $(T+V_1^2)1/2$ and is a first order correction to $\mathbf{M}^0$ due to gradients of the mena velocity. The second is multiplied by A(n) and is the lowest order approximation to the correction $\mathbf{M}^c$.

Equation (25) dictates that even in the absence of slip and mean velocity gradients, the biagonal components of B influence the supply of momentum in the N direction, the off-diagonal **t-N** and **τ-N** components of **B** are responsible for the supply of momentum in the tangential t and τ directions, and the off-diagonal **t-τ** component of **B** has no effect on **M**.

In the same special case to which expression (25) applies, the lowest order expressions for F and D are

$$F = \frac{4\rho\chi[2(T+V_2^2)]^{1/2}}{[\pi(1+R)]^{1/2}\sin^2\theta}\left\{\frac{1}{2}\left[\frac{(T+V_1^2)}{4} - V_1^2\right]J(R,\theta) - \frac{(T+V_1^2)}{4}K(R,\theta)\right\} \ , \qquad (29)$$

and

$$D = \frac{\rho\chi(1-e_w)[2(T+V_2^2)]^{3/2}}{8\pi^{1/2}(1+R)^{3/2}}[H(R,\theta) + 3\,I(R,\theta)] \quad . \tag{30}$$

Because the effects of velocity gradients and slip velocity make higher order contributions to F and D, expressions are identical to those obtained by Richman and Martin [1995], who ignored both effects, and by Richman and Martin [1993], who ignored velocity gradients.

4.3 Steady, Fully Developed, Parallel Flows

In what follows, we will examine several steady, fully developed granular flows in which the mean velocity either vanishes or is parallel to the vibrating boundary or boundaries with they interact. When there is more than one boundary, they are necessarily parallel to one another. Moreover, the spatial variations of the mean fields occur only in the direction perpendicular to the boundaries. In this section, we derive the general boundary value problem for these flows.

We employ the same Cartesian coordinate system introduced to write down the boundary conditions. Here x_1 points in the direction of flow velocity u_1, and x_2 defines the direction upon which the mean fields depend, and measures perpendicular distance from the lower vibrating boundary. We focus on cases in which the boundaries are horizontal. The flows are infinite in the x_1- and x_3-directions. The vertical acceleration (in the $-x_2$-direction) due to gravity is g. For purposes of nondimensionalization, we introduce the characteristic velocity a. The dimensionless fields of solid fraction ν, velocity $u \equiv u_1/a$, and the measure $w^2 \equiv T/a^2$ of granular temperature depend only on the dimensionless coordinate $Y \equiv x_2/\sigma$.

In these flows, the balance of mass and the x_3-component of the balance of momentum are identically satisfied. If $S \equiv -P_{12}/(\rho_p a^2)$ and $P \equiv P_{22}/\rho_p a^2$ are the dimensionless counterparts of the x_1-x_2 and x_2-x_2 components P_{12} and P_{22} of the pressure tensor, then the x_1-component of the momentum equation is

$$S' = 0 \quad , \tag{31}$$

where a prime denotes differentiation with respect to Y, and the x_2-component of the momentum equation is

$$P' = \frac{\sigma g}{a^2}\nu \quad . \tag{32}$$

If $q \equiv -Q_2/\rho_p a^3$ and energy dissipation $\Gamma \equiv \sigma\gamma/\rho_p a^3$ are the dimensionless counterparts to the x_2-component Q_2 of the energy flux and the energy dissipation γ, then the balance of energy reduces to

$$q' + Su' - \Gamma = 0 \quad . \tag{33}$$

It remains to express the constitutive relations in dimensionless form. Here and in what follows we take $a^2 = \sigma g$.

Here we employ the constitutive theory of Jenkins and Richman [1985]. The isotropic piece of the pressure tensor gives,

$$P = 4\nu G F w^2 \quad , \tag{34}$$

where G is given in terms of the radial distribution function g_0 by νg_0, $F \equiv 1 + 1/4G$, and the deviatoric piece gives,

$$S = \frac{2EPu'}{5\sqrt{\pi}Fw} \quad , \tag{35}$$

where $E \equiv 1 + \pi(1 + 5/8G)^2/12$. Equation (35) can be rearranged to express the velocity gradient u' in terms of the ratio S/P according to

$$u' = \frac{5\sqrt{\pi}FwS}{2EP} \quad . \tag{36}$$

The constitutive relations for q and Γ are,

$$q = \frac{2MPw'}{\sqrt{\pi}\,F} \quad , \tag{37}$$

where $M \equiv 1 + 9\pi(1 + 5/12G)^2/32$, and

$$\Gamma = \frac{6(1-e)Pw}{\sqrt{\pi}F} \quad . \tag{38}$$

We employ equations (37), (36), and (38) to eliminate q, u', and Γ from equation (33), and differentiate equation (34) with respect to Y to write ν' in terms of P' and w' wherever it appears. The energy equation can then be written in terms of w and its derivatives:

$$\frac{w''}{w} + \left[(1-2h)\frac{P'}{P}\right]\frac{w'}{w} + 4h\left(\frac{w'}{w}\right)^2 - \lambda^2 = 0 \quad , \tag{39}$$

where λ^2 is defined by

$$\lambda^2 \equiv \frac{1}{2M}\left[6(1-e) - \frac{5\pi F^2 S^2}{2EP^2}\right] \quad , \tag{40}$$

and 2h is the function of solid fraction defined by

$$2h \equiv \frac{-d[\ln(M/F)]/dv}{d[\ln(vGF)]/dv} \quad . \tag{41}$$

The quantity λ^2 is a local measure of the difference between the rate at which energy is dissipated by inelastic collisions and the rate at which energy is supplied to the flow by gravity.

The boundary motion is characterized by the second moment tensor **B** associated with the vibrations of the boundary. Because we have restricted our attention to cases in which $V_1=V_3$, the mean square fluctuation velocity is $3V^2=2V_1^2+V_2^2$. In order to write the conditions that express the balance of momentum and energy at a randomly fluctuating bumpy boundary in nondimensional form, we introduce the dimensionless boundary fluctuation speeds $V_t \equiv V_1/V$ and $V_n \equiv V_2/V$ that satisfy the relation $V_n^2+2V_t^2=3$. Thus defined, $V_n^2/3$ is the fraction of total vibrational energy that is distributed in the normal direction. The boundary's energy is divided evenly among the three coordinate directions when $V_n^2=1$, and is divided evenly between normal and tangential motion when $V_n^2=3/2$. In addition, we introduce the parameter $\alpha \equiv V/a$ which arises when nondimensionalizing the boundary conditions.

The x_3-component of the momentum balance (1) at the boundary dictates that because both v_3 and P_{23} vanish, then so too must B_{23}. That is, if no motion is to occur in the x_3-direction, then the boundary can not supply momentum in that direction. Because v_2, t_2, τ_2, I_{221}, I_{21}, and I_{221} are all zero, the x_2-component takes the simple dimensionless form

$$\alpha^2 v\chi(\Omega^2 + V_n^2) = P\left[1 - \frac{R\sin^2\theta}{2(1+R)}\right]^{-1} \quad , \tag{42}$$

where $\Omega \equiv w/\alpha$. In terms of the dimensionless boundary parameters, the ratio R is given by $V_n^2-V_t^2/\Omega^2+V_t^2$. In the expression for M_1 we employ equations (52), (36), (27), and (28) to eliminate c, u',\ I_{121}, I_{121}. The x_1-component of condition (1) then relates the dimensionless slip velocity $v \equiv -v_1/\alpha$ to Ω, v, and boundary motion and geometry through

$$\pm\frac{[2(\Omega^2+V_t^2)]^{1/2}I_{11}v}{(\pi)^{1/2}\alpha} = \frac{\sin^2\theta}{2}b_{12} + \frac{5\bar{\sigma}FS\Omega}{(2)^{1/2}\sigma EP}\left[(\Omega^2+V_t^2)^{1/2}\left(I_{11} - \frac{Y}{\sin^2\theta}\right) - \frac{A\sigma\Omega\sin^2\theta}{2\bar{\sigma}}\right]$$

$$+\frac{S(\Omega^2+V_n^2)}{P}\left[1-\frac{R\sin^2\theta}{2(1+R)}\right] \quad , \qquad (43)$$

where, from equation (26), $I_{11}(R,\theta)=[K-(1+4R)J/2]/[2R\sin 2\theta)$, $Y(R,\theta)$ is given by equation (23), and $b_{12}=B_{12}/V^2$. The positive (or negative) sign preceding equation (43) applies when the inward normal **N** points in the positive (or negative) x_2-direction. If the energy flux boundary condition (2) is manipulated in a similar manner, then the equation that determines w' at the boundary is

$$\pm\frac{[\pi(\Omega^2+V_n^2)(1+R)]^{1/2}}{(2)^{3/2}\csc^2\theta}\left[1-\frac{R\sin^2\theta}{2(1+R)}\right]\left[\frac{Sv}{P\alpha}+\frac{2Mw'}{\alpha(\pi)^{1/2}F}\right]=$$

$$\left[\frac{\Omega^2+V_t^2}{4}-V_t^2\right]J-\frac{(\Omega^2+V_t^2)}{2}K-(1-e_w)\frac{(\Omega^2+V_n^2)}{8(1+R)}[H+3I) \quad , \qquad (44)$$

where v/a is given by equation (43), and H, I, J, and K are given by equations (24), (20), (21), and (19), respectively. The positive (or negative) sign preceding equation (44) applies when the inward normal **N** points in the negative (or positive) x_2-direction.

The conditions at a free surface reflect the facts that normal stress, shear stress, and energy flux vanish there:

$$P=0 \quad \text{and} \quad S=0 \quad , \qquad (45)$$

and

$$w'=0 \quad . \qquad (46)$$

Equations (31), (32), (34), (36) and (39) determine S(Y), P(Y), v(Y), u(Y), and w(Y) to within five constants of integration. The manner in which the boundary conditions are employed to determine these constants depends on the particular boundary value problem. If, for example, the flows are confined between two bumpy boundaries (at $x_2=0$ and $x_2=L$) that are held a fixed distance apart, then the five constants are determined by conditions (43) and (44) at each boundary, and a prescription of either the mass hold-up

$$m_t \equiv \int_0^\beta v(Y)dY \quad , \tag{47}$$

where $\beta \equiv L/\sigma$, or the mass flow rate

$$\dot{m} \equiv \int_0^\beta v(Y)u(Y)dY \quad , \tag{48}$$

If, instead, one of the constants of integration were prescribed a priori (as would be the case when a known normal pressure is applied to one of the boundaries), then the same five conditions determine the remaining four constants of integration and the dimensionless distance β. Finally, if the flows are bounded from below by a bumpy boundary and unconfined from above, then the five constants of integration and the depth of flow β are determined by the two conditions (43) and (44) below, the three conditions (45) and (46) above, and a prescription of either m_t or $\dot{m}$.

The velocity does not appear in the system of equations (31), (32), (34), (and (39) for S(Y), P(Y), v(Y),and w(Y). Furthermore, condition (43) may be used to eliminate the slip velocity from the energy flux condition (44). Consequently, when m_t is prescribed rather than $\dot{m}$, and when the shear stress either vanishes everywhere or is known at a boundary (as it is at the free surface of an unconfined flow or at the center plane of a symmetric flow), then it is possible to determine S(Y), P(Y), v(Y), and w(Y) independently of u(Y). The velocity profile is then easily determined by integrating equation (36) from the boundary where the slip velocity is known from condition (43). All the boundary value problems that we will consider uncouple in this manner.

4.4 Deterministic Boundary Motion

The boundary conditions derived in sections (4.1) and (4.2) apply to boundaries whose vibration is random and described in terms of a velocity distribution function. Calculating similar boundary conditions for boundaries that vibrate harmonically would require carrying out averages that account for the dependence of the boundaries' velocities on time. To avoid this complication, we assume that the averages carried out based on a statistical (i.e. anisotropic Maxwellian) description of the boundaries' velocities adequately represent boundaries whose motion is harmonic provided we relate the components of second moment tensor **B** that describe the random motion of fluctuating boundaries to the amplitudes and frequencies that describe the periodic motion of harmonic boundaries. To this end, we consider boundaries that vibrate periodically in the three coordinate directions about a position that is independent of time. The particles on the boundary have velocities in the three directions given by

$$x_i = A_i n_i \omega \sin(n_i \omega t+\zeta_i) \quad , \qquad (i=1,2, \text{ or } 3) \tag{49}$$

where $n_2=1$, and n_1 and n_2 are positive integers. The amplitudes A_i, phase angles ζ_i, integers n_1 and n_3, and frequency factor ω are all adjustable parameters that influence the rates at which momentum and energy are transferred to the flows. We restrict attention to boundaries with amplitudes of vibration that are of the same order as the mean free path within the flow, and with periods of oscillation that are of the same order as the time between collisions within the flow. For these boundaries, we interpret the components B_{ij} in the rates (25, (29), and (30) for **M**, F, and D as the time averages of the products $x_i x_j$ over the longest period $2\pi\omega$ of oscillation; i.e.,

$$B_{ij} = \begin{cases} \frac{1}{2} A_i A_j n_i n_j \omega 2 \cos(\zeta_i - \zeta_j) & n_i = n_j \\ 0 & n_i \neq n_j \end{cases} \tag{50}$$

According to this correspondence, any two diagonal components ($B_{11} \equiv V_1^2$, $B_{22} \equiv V_2^2$, $B_{33} \equiv V_3^2$) of **B** will be equal when the corresponding products, A_1n_1, A_2n_2, A_3n_3 are equal; any off-diagonal component of **B** will vanish when the vibrations in the two corresponding orthogonal directions are either at the same frequency and $\pi/2$ radians out of phase, or at frequencies that are unequal integer multiples of same factor.

4.5 Thermalization of Unconfined Assemblies Induced by Isotropic Boundary Vibrations

Of concern here is the influence of bumpy boundaries that vibrate isotropically on the granular assemblies with which they interact. These are boundaries for which the second moment **B** is isotropic. According to expression (25) for **M**, the vibrations of such boundaries transmit no tangential momentum to the flows, and induce no mean motion of the assemblies. Of particular interest are the thermalized states of unconfined assemblies that are compressed by gravity and bounded from below by a horizontal boundary. We will examine the effects of the vibrational energy and bumpiness of the boundary on these states. The general flow equations and boundary conditions derived in section 4.3 will be reduced for these flows and solved numerically.

Here, we take characteristic velocity $a=(\sigma g)^{1/2}$, and locate the origin of the coordinate system to coincide with the location of the lower boundary such that Y varies from 0 at the lower boundary to β at the top of the flow (i.e. the free surface of an unconfined flow or the upper boundary of a confined flow). According to equation (30), the shear stress S is constant throughout the assemblies. In the cases considered here, the shear stress vanishes at a free surface. Consequently, the shear stress vanishes everywhere. Moreover, constitutive relation (36) for u' demonstrates that when S vanishes, the mean velocity is constant and the assemblies move uniformly. But according to tangential momentum balance (43), when S is zero and **B** is isotropic, the slip velocity and therefore the mean velocity everywhere in the flow vanishes. The reduced system of equations that determines the variations of the normal stress and mean fields of solid fraction and granular temperature are then given by (32) for P(Y), (34) for v(Y), and (39) for w(Y).

At a free surface, the boundary conditions are the first stress-free condition (45) and the energy flux condition (46). For bumpy boundaries whose motion is isotropic, **B** is proportional to the identity tensor $\delta_{,,}$ V_n and V_t are unity, and the ratio R vanishes. Under these circumstances, when expression (2.3) for $J(R=0,\theta)$ is employed, the energy flux condition (44) at a bumpy boundary simplifies to

$$\frac{w'}{w} = \pm \frac{(2)^{1/2}F(1-\cos\theta)\csc^2\theta}{Mw(w^2+\alpha^2)^{1/2}}\left[2\alpha^2 - (1-e_w)(w^2+\alpha^2)\right] \quad , \qquad (51)$$

in which $\alpha \equiv V/(\sigma g\}^{1/2}$ is the dimensionless fluctuation speed of the boundary. The positive (or negative) sign preceding the right-hand side of equation (51) applies when the inward normal **N** points in the negative (or positive) Y-direction as it does at a lower bumpy boundary. The first and second terms on the right-hand side of equation (51) are measures of the energy supplied to the assembly by the vibrations of the boundary and the energy absorbed in dissipative collisions with the boundary.

4.5.1 Solution Procedure

We are interested in the effects of gravity and the full range of boundary vibration on unconfined assemblies; from cases in which the vibrational energy of the horizontal boundary tends to zero, to those where the boundary becomes extremely energetic. In the former case, we expect that as the boundary energy tends toward zero, so too will the granular temperature everywhere within the flow. In order to ensure that, even under these extreme circumstances, the solid fraction does not exceed its random close packed value v_m, we take $G(v)=v/(1-v/v_m)5v_m/2$. This form of G is based on the radial distribution function $g_0(v)$ at impact proposed by Lun and Savage [1986], which has the correct value (=1) and slope (=5/2) in the dilute limit, agrees well with that proposed by Carnahan and Starling [1969] for all values of v up to .5, and becomes unbounded as v approaches v_m so that collisions between particles may support high pressures at low granular temperatures. The results presented in the next section are based on the random close paced value v_m=.65 supposed by Johnson et. al. [1990].

Equations (32), (34), and (39) determine P(Y), v(Y), and w(Y) to within three constants of integration. These constants and the depth β are determined by the first of stress conditions (45) and the energy flux condition (46) at the free surface, condition (51) at the boundary, and a fixed mass hold-up m_t calculated according to its definition (47). In principle, the solution procedure is as follows. For fixed values of mass hold-up m_t, coefficients of restitution e and e_w, bumpiness θ, and dimensionless fluctuation speed α of the boundary, we guess at the measure w of granular temperature at the top of the assembly, and numerically integrate equations (32), (34), and (39) downward from the location at which both P and w' vanish to the depth at which the mass hold-up assumes its prescribed value. Condition (51), which may be written as a quadratic equation for α^2, then determines the value of α that sustains that thermalized state. Finally, we iterate on the guess for w at the top until the value of α calculated in this manner agrees with its prescribed value. The distance over which the final integration is carried out is the depth β.

In practice, the solution procedure is somewhat less straightforward. As described in section 1.2, whenever a free surface exists, the theory predicts that the flow is infinitely deep and that the mean fields approach their values at Y=β asymptotically from the base. Integrations initiated as described above therefore yield no spatial variations in P, v and w. In order to overcome this difficulty, we follow the procedure described in section 1.2 by initiating the integrations with a very small value of v at the ``top" of the flow.

4.5.2 Results and Discussion

In this section, we consider only the case in which $e=e_w=.9$ and the boundary parameter θ is equal to $\pi/6$, unless otherwise indicated. This value of θ includes the special case in which the diameter σ of the flow particles is equal to the diameter d of the flow particles, and the spacing s between boundary particles vanishes. In order to present the results compactly, we introduce the normalized function of Y,

$$\xi(Y) = \frac{1}{m_t}\int_0^Y v(Y)dY \quad , \tag{52}$$

which gives the fraction of the total mass m_t below any location Y, and varies from 0 (when Y=0) at the base to 1 (when Y=β) at the top of the assembly.

In presenting our results, we first study the effects of vibrational speed α on the thermalized states of fixed mass hold-ups m_t. In Figures 4.1 a, b, c, and d, for example, we show the variations of $w(\xi)$ with α for ξ=0, .05, .1, .25, .5, .75, and 1 when m_t=2.5, 5, 10, and 20. As expected, the granular temperatures, which are induced entirely by basal vibrations, increase from zero as α increases form zero. For any pair of α and m_t, the temperature deceases monotonically from the base (ξ=0) to the top of the assembly (ξ=1). This is because energy must be conducted into the mass above any location Y to balance the collisional dissipation that occurs within that mass. Furthermore, because the energy flux at the top of the assembly vanishes, the energy flux at the boundary must balance the total dissipation in the assembly. Consequently, the granular temperature typically varies far more widely throughout the lower half of the mass than it does in the upper half, and hardly varies at all through the upper quarter of the mass. These observations become more striking as the mass hold-up increases. According to Figures 4.1 c and d, the measure w of granular temperature is less than .01 in the upper portions of the assemblies for values of α less than .81 when m_t=10 and for all values of α (between 0 and 5) when m_t=20. Under these circumstances, the energy supplied by the vibrating boundary is, in effect, *insufficient to thermalize the entire assembly.*

In Figures 4.2 a and b, we show the variations of w and v with Y for α= .25, 2, and 5 when m_t=5. The solid dots on the profiles indicate the heights at which ξ=.99. These profiles are typical. As the fluctuation speed of the boundary increases, the assembly becomes deeper, more dilute, and more thermalized. The granular temperature increases monotonically from the top to the bottom of the assembly, whereas the solid fraction increases from zero at the top to its maximum at an intermediate location and then decreases to a smaller value at the base. In fact, P' and w' are negative everywhere; but when constitutive relation (34) is differentiated with respect to Y we obtain the relation for v',

$$v' = \frac{\frac{P'}{P} - \frac{2w'}{w}}{\frac{d}{dv}[\ln(vGF)]} \quad , \tag{53}$$

which is positive only where P'/P is greater than 2w'/w.

Next we study the effects of varying the mass hold-up on the thermalized states induced by boundaries whose vibrational speeds α are fixed. In Figures 4.3 a, b and c, for example, we plot the variations of $w(\xi)$ with m_t for ξ=0, .05, .1, .25, .5, .75, and 1 when α= .25, 2, and 5. As expected, for fixed values of vibrational speed α and mass fraction ξ, the granular temperature typically decreases as the total mass hold-up increases. Interestingly, this effect on $w(\xi)$ diminishes as ξ decreases, until at the base

(ξ=0) the granular temperature is virtually insensitive to mass hold-ups beyond about 2.5. Figure 4.3 also demonstrates that as vibrational speed increases, so too does the mass that can be effectively thermalized. As α varies from .25 to 2.5 to 5, for example, the maximum values of m_t for which w is everywhere greater than .01 increases from 8.22 to 11.10 to 11.94.

In Figures 4.4 a and b we show the variations of w and v with Y for m_t=2.5, 5, 10, and 20 when α=2. Again the solid dots indicate the locations at which ξ=.99. Although the effect of increasing the mass of the assembly from m_t=2.5 to 20 is to decrease the granular temperatures everywhere, the decrease is far more pronounced near the top of the assembly than at the base. At the two lower values (m_t=2.5 and 5) of mass hold-up, the boundary vibrations are sufficient to fully thermalized the assemblies and to disperse them at solid fractions that are everywhere significantly less than the random close packed value. However, at the two higher values (m_t=10 and 20), the assemblies are, in effect, only partially thermalized. These more massive assemblies consist of an upper passive region, in which the solid fraction is essentially constant and nearly equal to its maximum value, supported by a thermalized region that extends approximately 11 particle diameters above the base.

Finally, in Figures 4.5 a and b, we study the effects of boundary bumpiness on the induced thermalized states by plotting the profiles of w(Y) and v(Y) for θ=0, $\pi/3$, and $\pi/2$ when α=2 and m_t=5. The effects demonstrated here, as the boundary evolves from perfectly flat (θ=0) to extremely bumpy ($\theta=\pi/2$), are typical. As θ increases from zero, so too does the energy imparted to the assembly by the tangential components of the isotropic boundary vibrations. For this reason, as the boundary becomes bumpier, the granular temperatures increase and the solid fraction decrease throughout the assembly. However, these effects are moderated by the fact that the energy imparted to the assembly by the normal component of the boundary vibrations actually decreases as the boundary becomes bumpier and experiences fewer normal and greater number of oblique impacts with the assembly. Consequently, as the boundary becomes bumpier it becomes only moderately more effective at transferring energy to the assembly. The net effect of varying θ on the resulting thermalized states is therefore relatively minor.

4.6 Thermalization and Mean Motion Induced by Anisotropic Boundary Vibration

In this section we study the effects of bumpy boundaries that vibrate anisotropically on the granular assemblies with which they interact. These are boundaries whose second moment of velocity fluctuation **B** is anisotropic, and whose vibratory motion can by itself induce slip. In particular, we study the effects of these boundaries on unconfined flows compressed by gravity. Although the shear stress vanishes everywhere within the flows, the boundary may transmit tangential momentum to the assemblies, which therefore may experience mean motion. In these unconfined flows we examine dependence of both the thermalized state and the mean motion induced not only on the distribution of energy and boundary bumpiness, but also on the total amount of vibrational energy.

4.6.1 Solution Procedure

Here, we are concerned with unconfined flows that are compressed by gravity and driven by horizontal boundaries that vibrate anisotropically. We take the characteristic velocity a equal to $(\sigma g)^{1/2}$ and locate the origin of coordinate system at the boundary such that Y varies from 0 at the boundary to β at the free surface. Here, we take G(v) as $v(2-v)/2(1-v)^3$ and solve the full equations numerically. Now w and u are equal to their dimensional counterparts $(T)^{1/2}$ and u_1 scaled by $a=(\sigma g)^{1/2}$. The ratio $\alpha \equiv V/(\sigma g)^{1/2}$ will appear in the boundary conditions and affect the solutions for w and u.

In these simple flows, according to equation (31), the shear stress is constant throughout the assembly. Because, according to the second of stress conditions (45), the shear stress vanishes at the free surface, it vanishes everywhere. Because, according to equation (36), the velocity gradient is proportional to the shear stress, it also vanishes, and the assemblies move uniformly. Therefore, the system of equations that determines the variations of the stresses and mean fields are given by (32) for P(Y), (34) for v(Y), and (39) for w(Y).

The boundary at Y=0 moves with velocities given by equation (49) for x_I. They oscillate with frequency ω in the x_1- and x_2-directions, a higher frequency $n_3\omega\backslash$ $(n_3\neq 1)$ in the x_3-direction, and amplitudes A_1, A_2, and $A_3=A_1/n_3$ in the x_1-, x_2-, and x_3-directions. The phase difference $\zeta_1-\zeta_2$ is equal to ζ. According to relation (50), this boundary corresponds to one whose velocity fluctuations are described by the second moment tensor,

$$B_{ij}=\begin{bmatrix} V_1^2=A_1^2\omega^2/2 & B_{12}=V_1V_2\cos\zeta & 0 \\ B_{21}=V_1V_2\cos\zeta & V_2 2=A_2^2\omega^2/2 & 0 \\ 0 & 0 & V_3^2=A_1^2\omega^2/2 \end{bmatrix}, \qquad (54)$$

Under the influence of these boundaries, the material flows only in the $+x_{\_1}$-direction.

The conditions at the bumpy boundary determine uniform velocity u=v, and the granular temperature there. They are the balance of momentum (43) with S=0,

$$u=\frac{\alpha(\pi)^{1/2}R\sin^4\theta}{[2(\Omega^2+V_t^2)]^{1/2}}\left[K-\frac{1+4R}{2}J\right]^{-1}V_tV_n\cos\zeta\ , \qquad (55)$$

where $\Omega = w(0) \backslash \alpha$ and $R = V_n^2 - V_t^2)/(\Omega^2 + V_t^2)$, and the balance of energy (44),

$$\frac{-Mw'[(\Omega^2 + V_n^2)(1+R)]^{1/2}}{(2)^{1/2}\alpha F \csc^2\theta}\left[1 - \frac{R\sin^2\theta}{2(1+R)}\right] =$$

$$\left[\frac{\Omega^2 + V_t^2}{4} - V_t^2\right] J - \frac{(\Omega^2 + V_t^2)}{2} K - (1-e_w)\frac{(\Omega^2 + V_n^2)}{8(1+R)} [H+3I) \quad , \qquad (56)$$

in which we have used the fact that S=0. The boundary conditions at the free surface are given by the first of conditions (45) and condition (46).

In principle, for fixed values of e, equations (32), (34), and (39) determine P(Y), ν(Y), and w(Y) to within three constants of integration. For fixed values of V_n, V_n^2, α, and e_w, those constants and the depth of flow are determined by the first of the stress free conditions (45) and energy flux condition (46) at the free surface, the energy flux condition (56) at the base, and by prescribing the mass hold-up m_t.

In practice, the solution procedure is somewhat more complicated. As described in the earlier sections that dealt with unconfined flows, in order to initiate the numerical integrations we must slightly relax the normal pressure condition at the free surface by assigning a small value to ν, and by guessing the value of w there. In this manner, we integrate equations (32), (34), and (39) from the free surface (where w' vanishes) to the location Y at which m_t assumes its prescribed value. With ν, w and w' at the boundary determined by the integrations, we check that condition (56) is satisfied for chosen values of V_n, θ, α, and e_w. If it is not, we iterate on the guess for w at the free surface until it is satisfied. Equation (55) then determines the uniform scaled velocity $u/\cos\zeta$.

4.6.2 Results and Discussion

Of primary interest are the effects of the boundaries' motion, geometry, and vibrational energy on the thermalized states and mean motion that their vibrations induce. For this reason, in carrying out the solution procedure described above, we have varied only V_n, θ, and α. All the results presented here are for m_t=5 and $e = e_w = .9$. Interestingly, because the shear stress vanishes throughout the assemblies, the solid fraction and temperature profiles do not depend on the mean motion of the assembly. Consequently, the predicted profiles ν(Y) and w(Y) apply both to assemblies that do and do not experience mean motion. Mean motion will occur if the phase angle ζ between the vibrations in the x_1- and x_3-directions is unequal to $\pi/2$. Because the mean velocity scales with phase angle ζ, it need not be specified.

In Figure 4.6, we plot the variations of the granular temperature w(0) at the boundary with bumpiness θ for normal fluctuation speeds V_n^2=0, 1, 3/2, 2, and 3, when α=2. We observe that when the vibrations are due entirely to tangential motion ($V_n^2=0$), the temperatures increase as the boundaries become bumpier, and when vibrations are due entirely to normal motion ($V_n^2=3$), the temperatures decrease as the boundaries become bumpier and experience fewer normal and more oblique impacts. Moreover, for fixed values of θ between $\pi/6$ and $\pi/3$, the granular temperatures throughout the assemblies increase monotonically as the energy of tangential vibration is converted to energy of normal vibration.

In Figure 4.7 we show the variations of w(0) with bumpiness θ for dimensionless root mean fluctuation speed $\alpha \equiv V/(\sigma g)^{1/2}=1, 2, 3, 4$, and 5, when $V_n^2=1$. The temperature w(0) increases with increasing θ because, for each value of α, two-thirds of the total vibrational energy is in the tangential mode. Interestingly, under these circumstances, w(0) is rather insensitive to θ and apparently very nearly scales with α.

In Figure 4.8 we show the variations of scaled velocity $u/\cos\zeta$ with bumpiness θ for the case when $\alpha=1, 2, 3, 5$, and 5, and $V_n^2=1$ taken from Figure 4.7. Over this range of θ, for fixed values of α, the slip velocity increases with decreasing bumpiness θ. While both the driving force due to vibrations and the resisting force due to slip diminish with decreasing θ, this result suggests that the former is less sensitive to θ than the latter. In addition, Figure 4.8 demonstrates that the velocity u very nearly scales with α.

In Figure 4.9 we show the variations of w(0) with V_n^2 for $\alpha=1, 2, 3, 4$, and 5, when $\theta=\pi/6$. In Figure 4.10 we show the corresponding variations of scaled velocity $u/\cos\zeta$. For fixed values of total boundary vibrational energy α, Figure 4.9 demonstrates that the granular temperature monotonically increases as that energy is converted from tangential motion ($V_n^2=0$) to normal motion($V_n^2=3$).

Figure 4.10 demonstrates that when the boundary motion is distributed entirely in either normal or tangential motion, it is unable to induce mean motion. However, away from these extreme cases, the boundary does induce slip. In fact, at least for $\theta=\pi/6$, slip is maximized when V_n^2 is about .72. That this optimum value of V_n^2 is nearly independent of α is another indication that u roughly scales with α.

In Figures 4.11 and 4.12 we show the granular temperature and solid fraction profiles w(Y) and v(Y) for $V_n^2=0, 1, 1.5, 2$, and 3, when $\theta=\pi/6$ and $\alpha=2$. Solid dots on the profiles indicate the value of Y below which 99% of the mass m_t is contained. For these parameters, as V_n^2 increases from 0 to 3, the boundary becomes more effective at thermalizing the assembly and the flows become deeper, more thermalized, and more dilute. Qualitatively similar observations can be made for other fixed combinations of bumpiness θ and vibrational energy α.

4.7 Figures

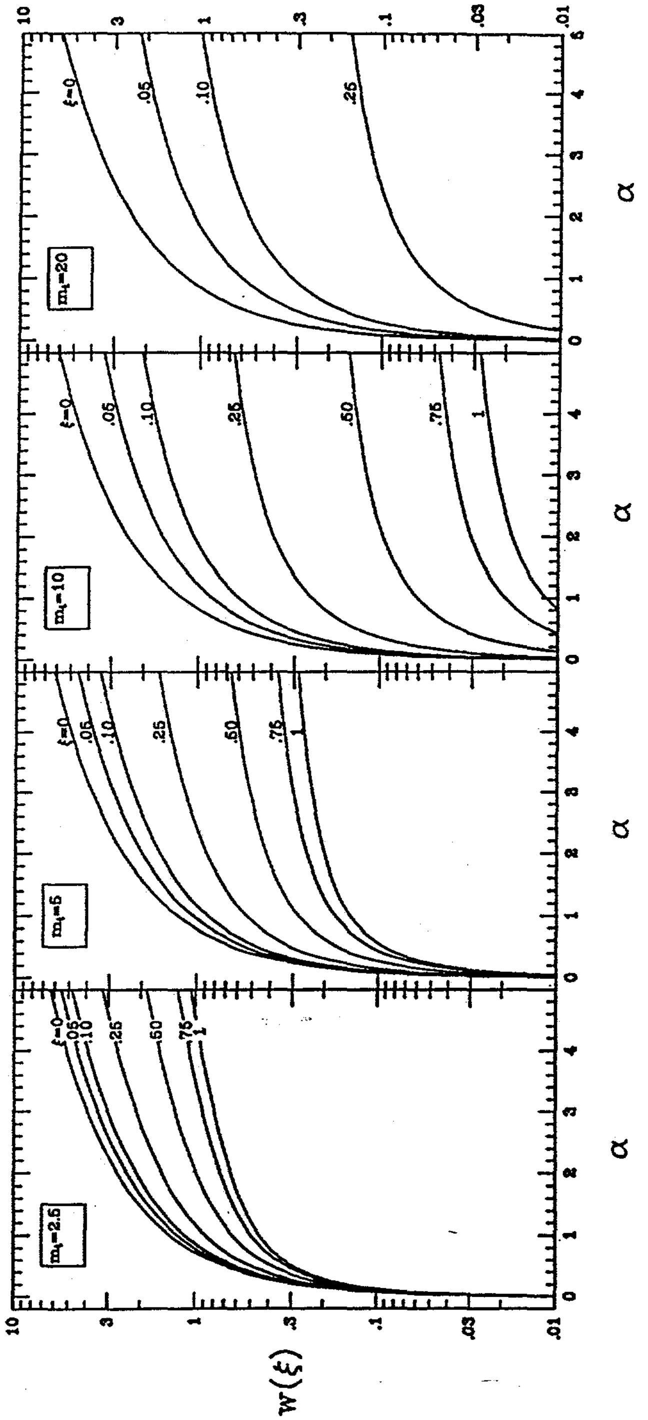

Figure 4.1: The variations of $w(\xi)$ with α for a) m_t=2.5, b) m_t=5, c) m_t=10, and d) m_t=20, when ξ=0, .05, .10, .25, .5, .75, and 1, $\theta=\pi/6$, and $e=e_w$=.9.

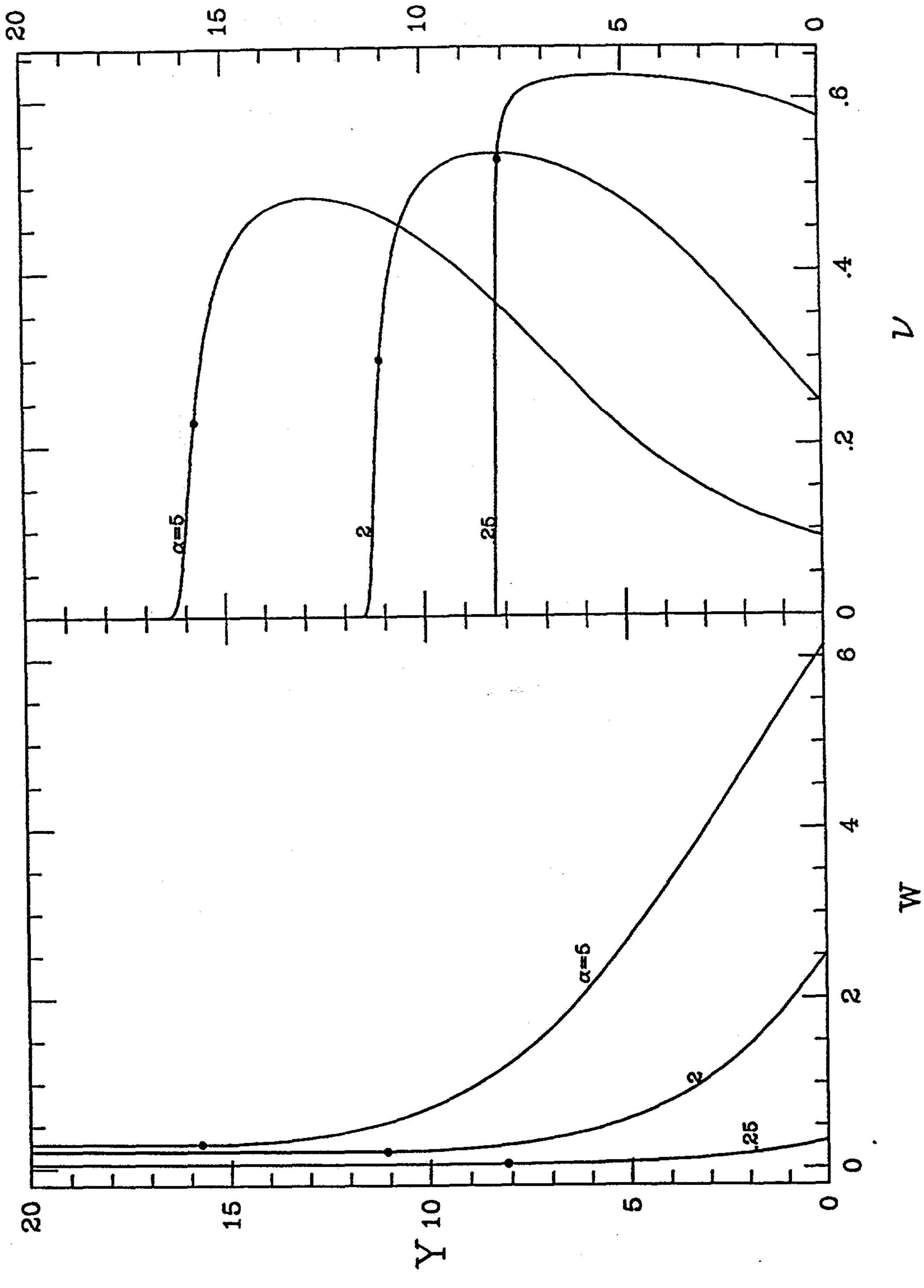

Figure 4.2: The variations of a) w and b) v with Y for α=.25, 2, and 5, when, m_t=5, $\theta=\pi/6$, and $e=e_w$=.9.

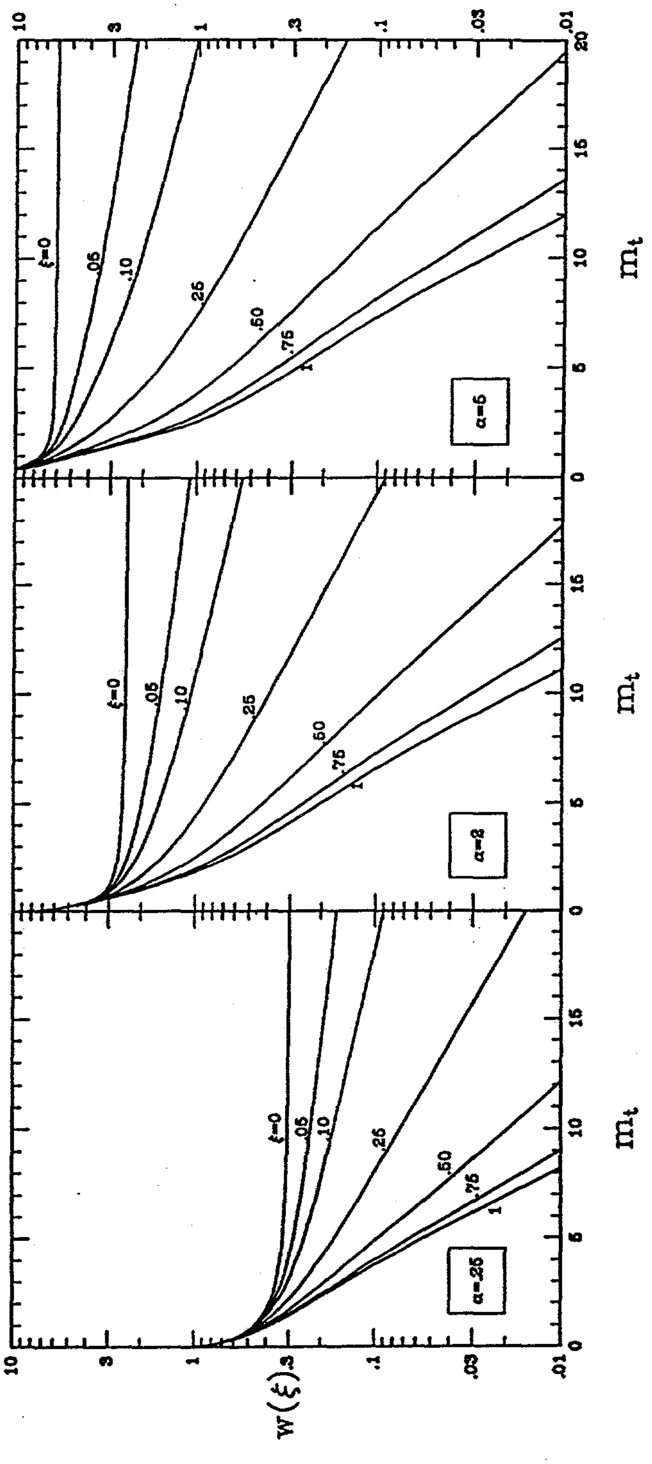

Figure 4.3: The variations of $w(\xi)$ with m_t for a) $\alpha=.25$, b) $\alpha=2$, and c) $\alpha=5$, when $\xi=0, .05, .10, .25, .5, .75$, and 1, $\theta=\pi/6$, and $e=e_w=.9$.

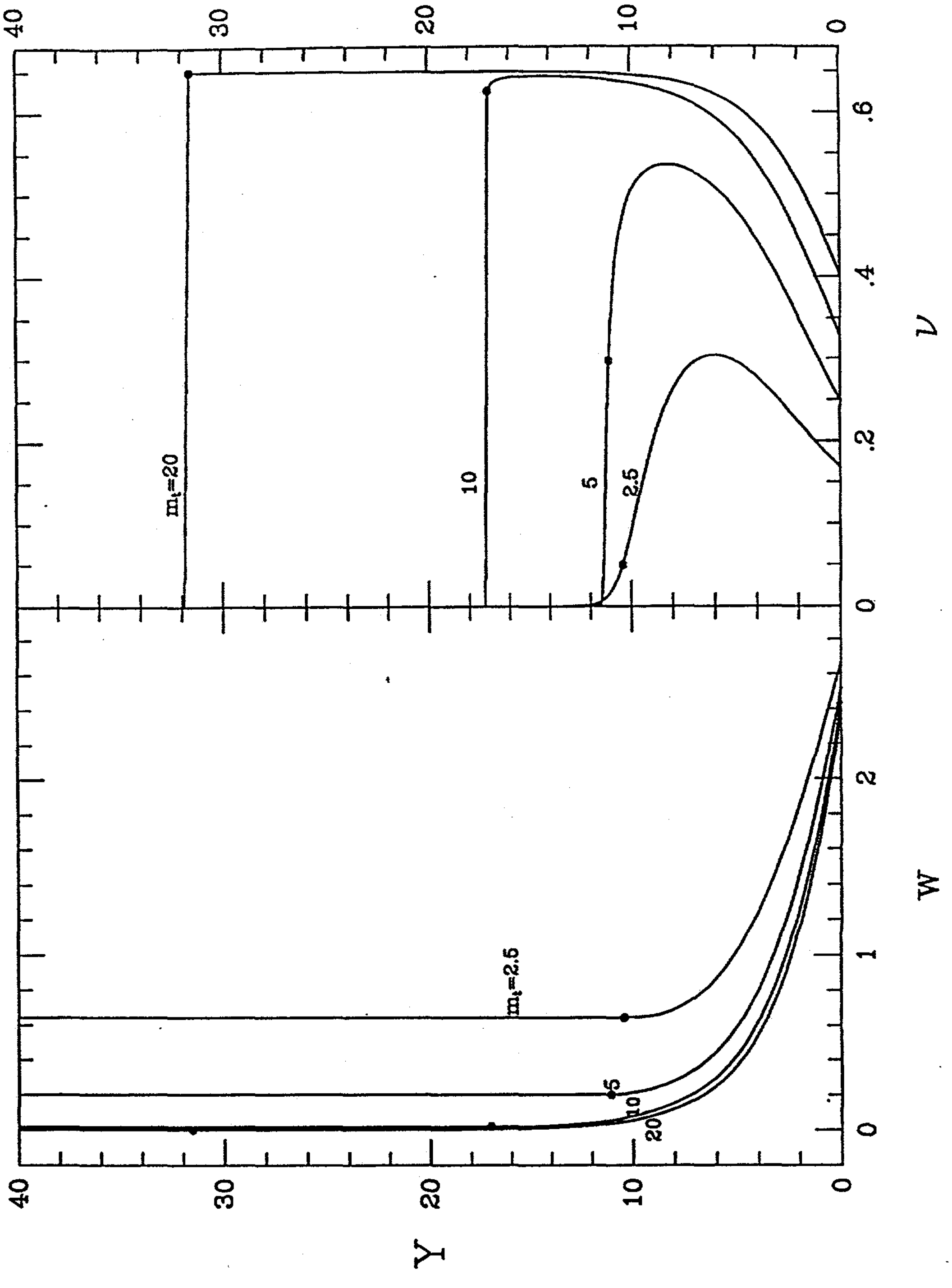

Figure 4.4: The variations of a) w and b) v with Y for m_t=2.5, m_t=5, m_t=10, and m_t=20, when α=2, $\theta=\pi/6$, and e=ew=.9.

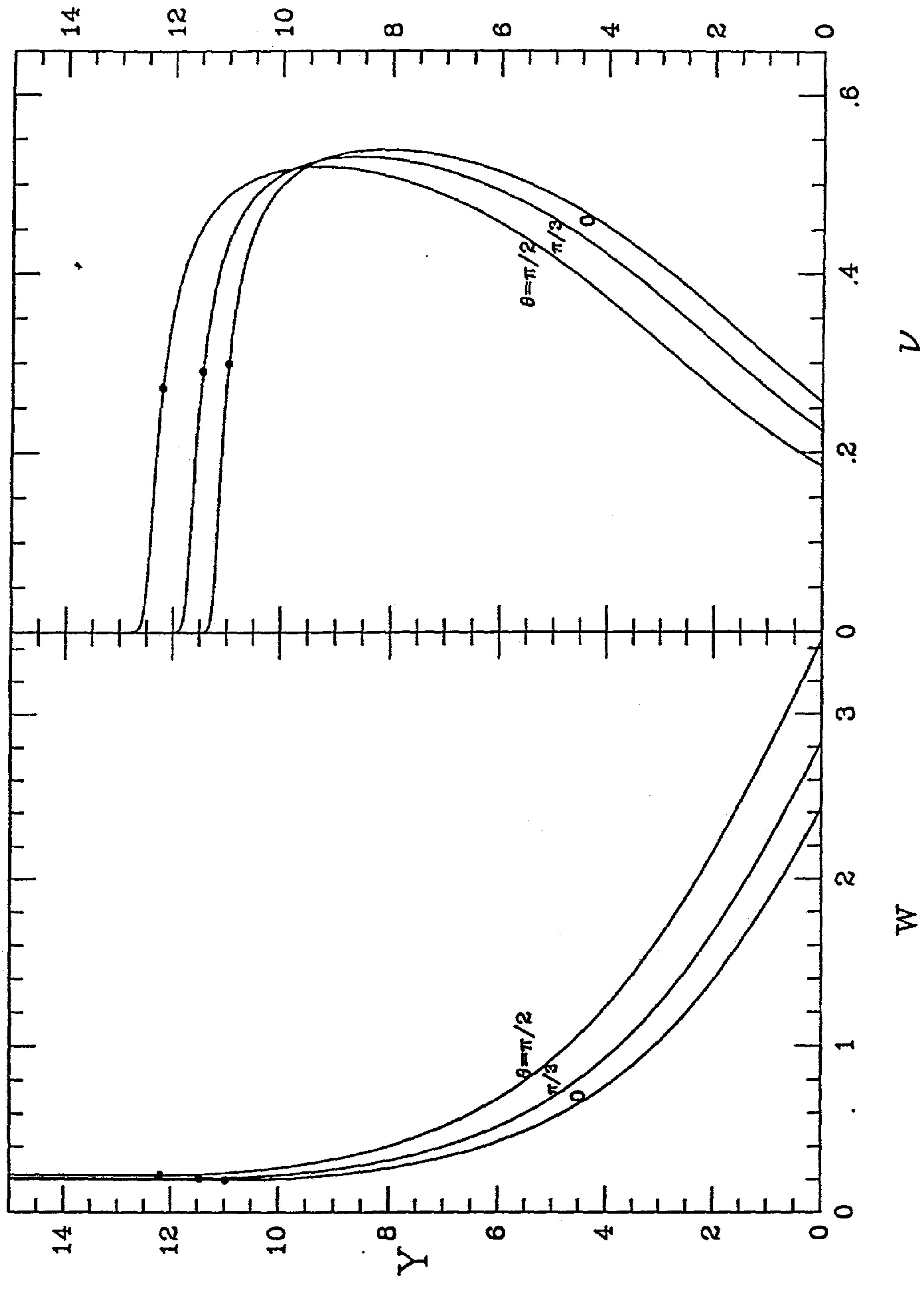

Figure 4.5: The variations of a) w and b) v with Y for θ=0, π/3, and π/2 when α=2, m_t=5, and e=e_w=.9.

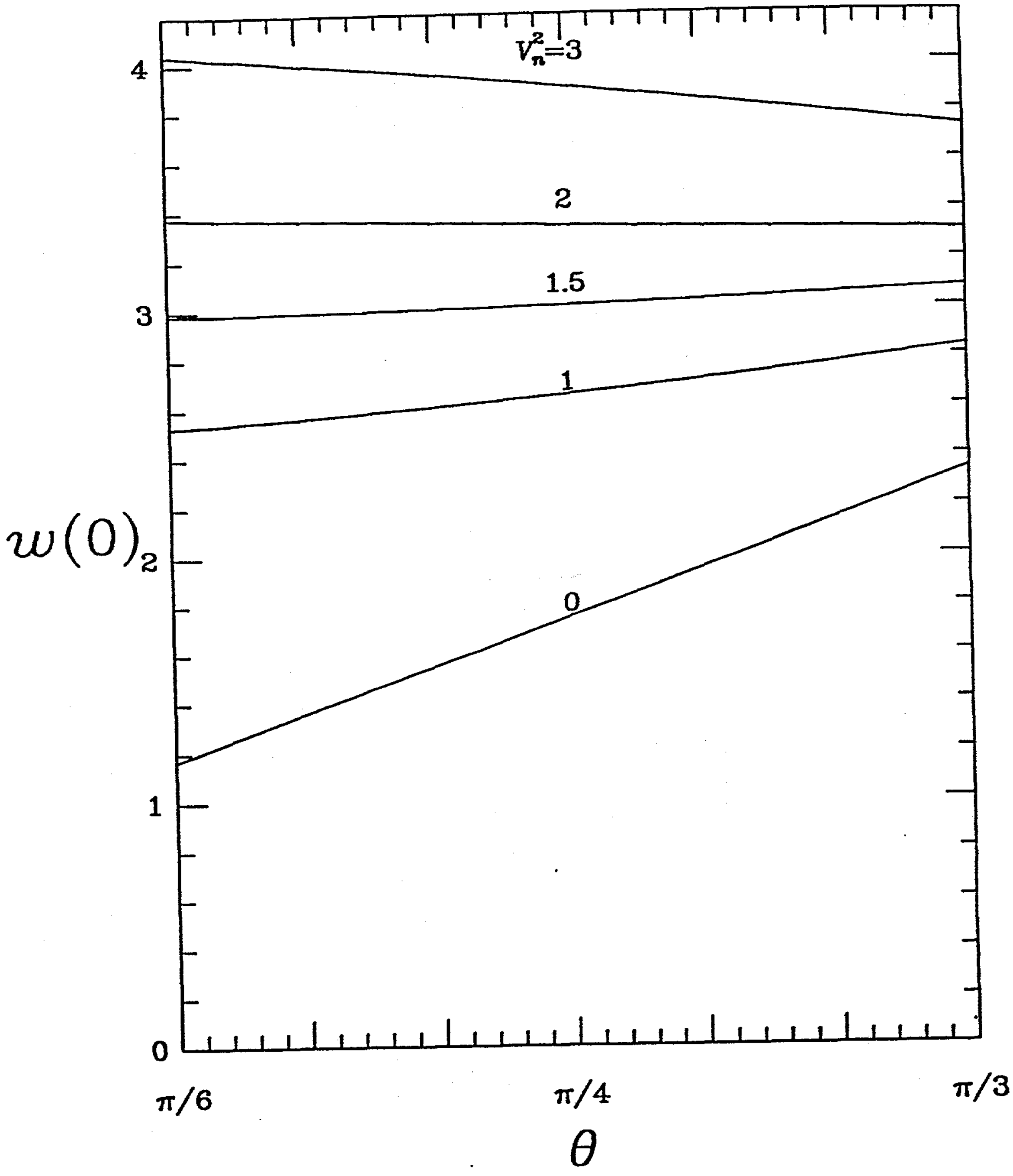

Figure 4.6: The variations w(0) with θ for $V_n^2=0, 1, 3/2, 2,$ and 3, when $\alpha=2$, $e=e_w=.9$, and $m_t=5$.

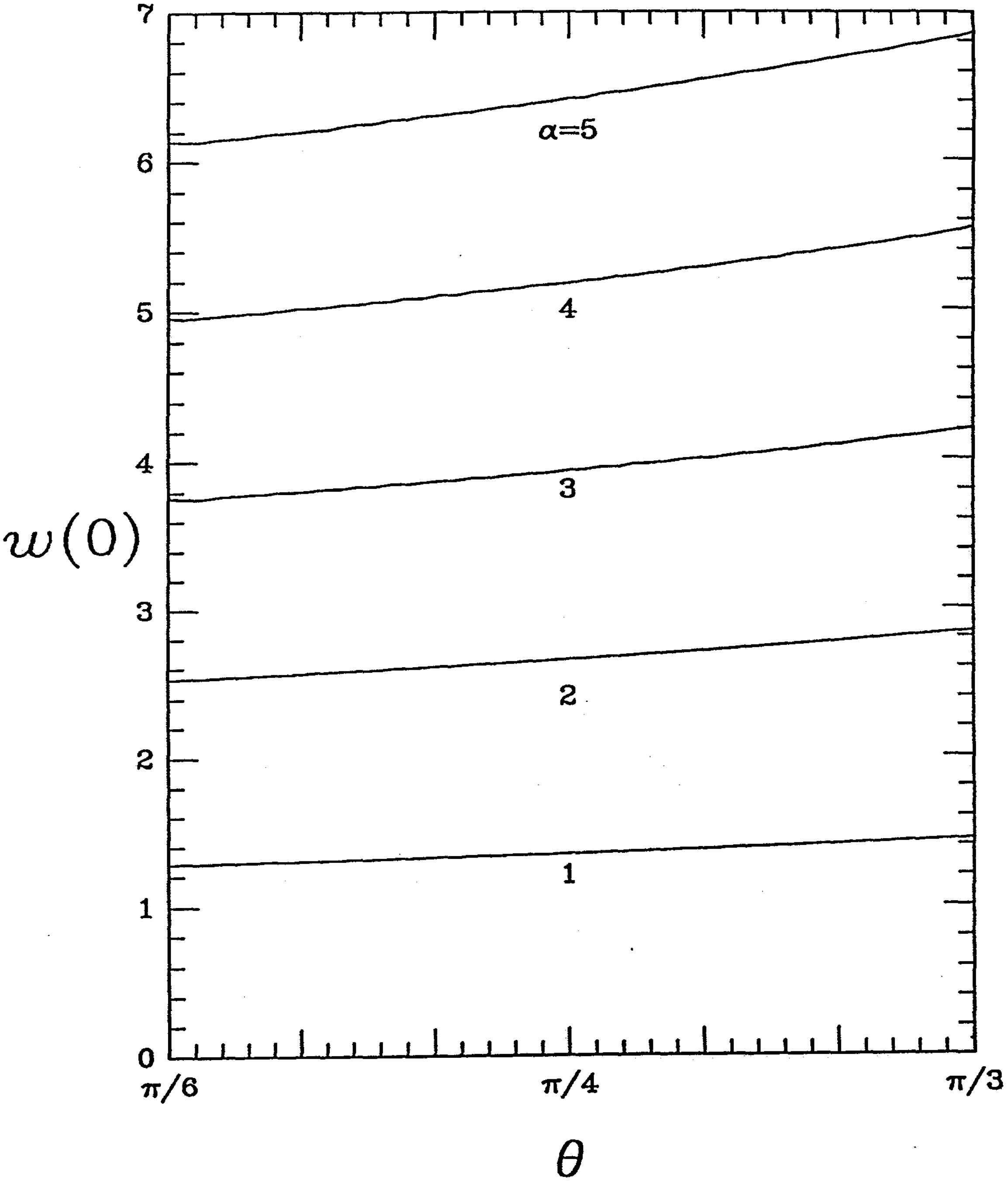

Figure 4.7: The variations of w(0) with θ for $\alpha=1, 2, 3, 5$, and 5, when $V_n^2=1$, $e=e_w=.9$ and $m_t=5$.

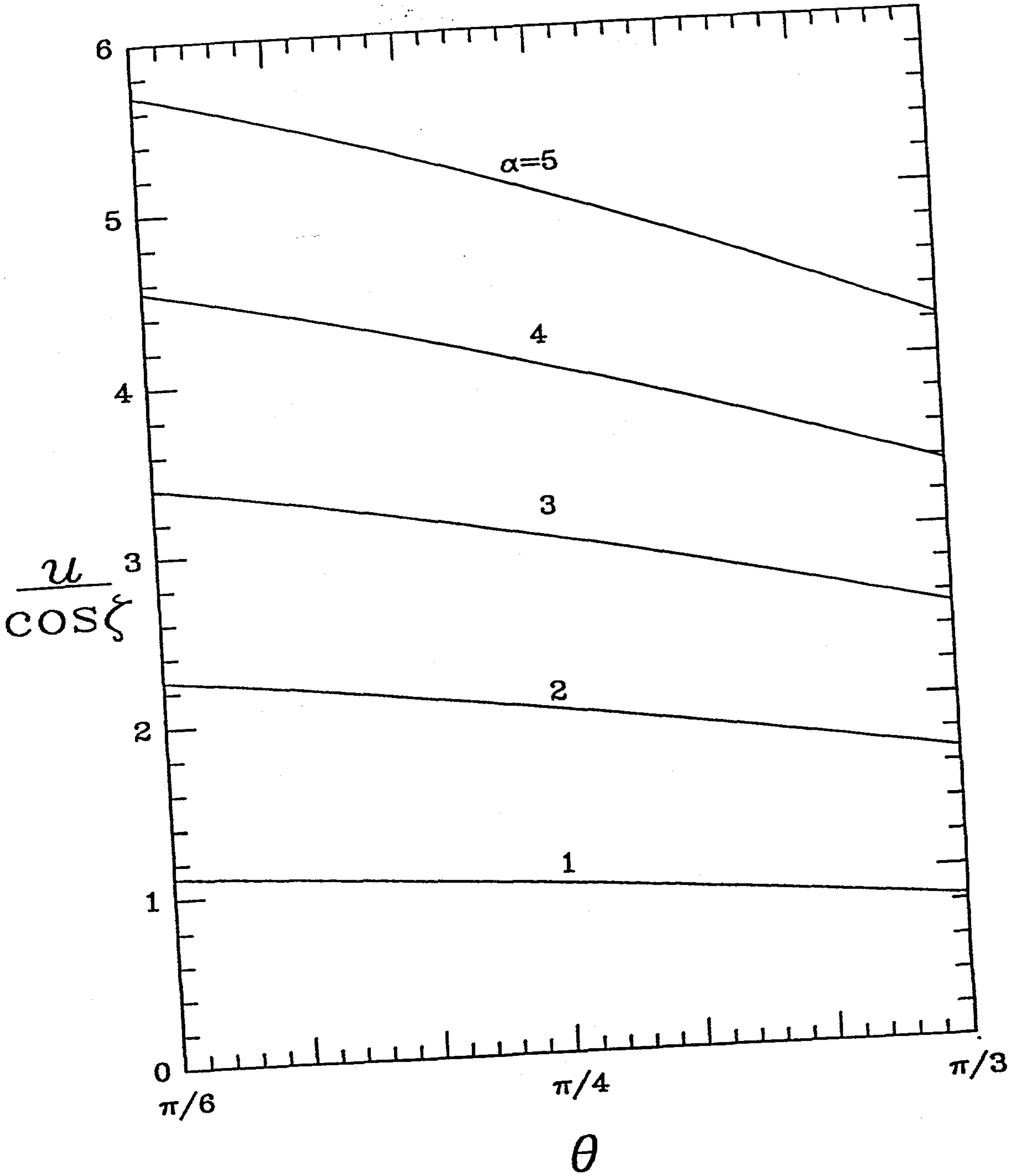

Figure 4.8: The variations of $u/\cos\zeta$ with θ for α=1, 2, 3, 5, and 5, when $V_n^2=1$, $e=e_w=.9$ and $m_t=5$.

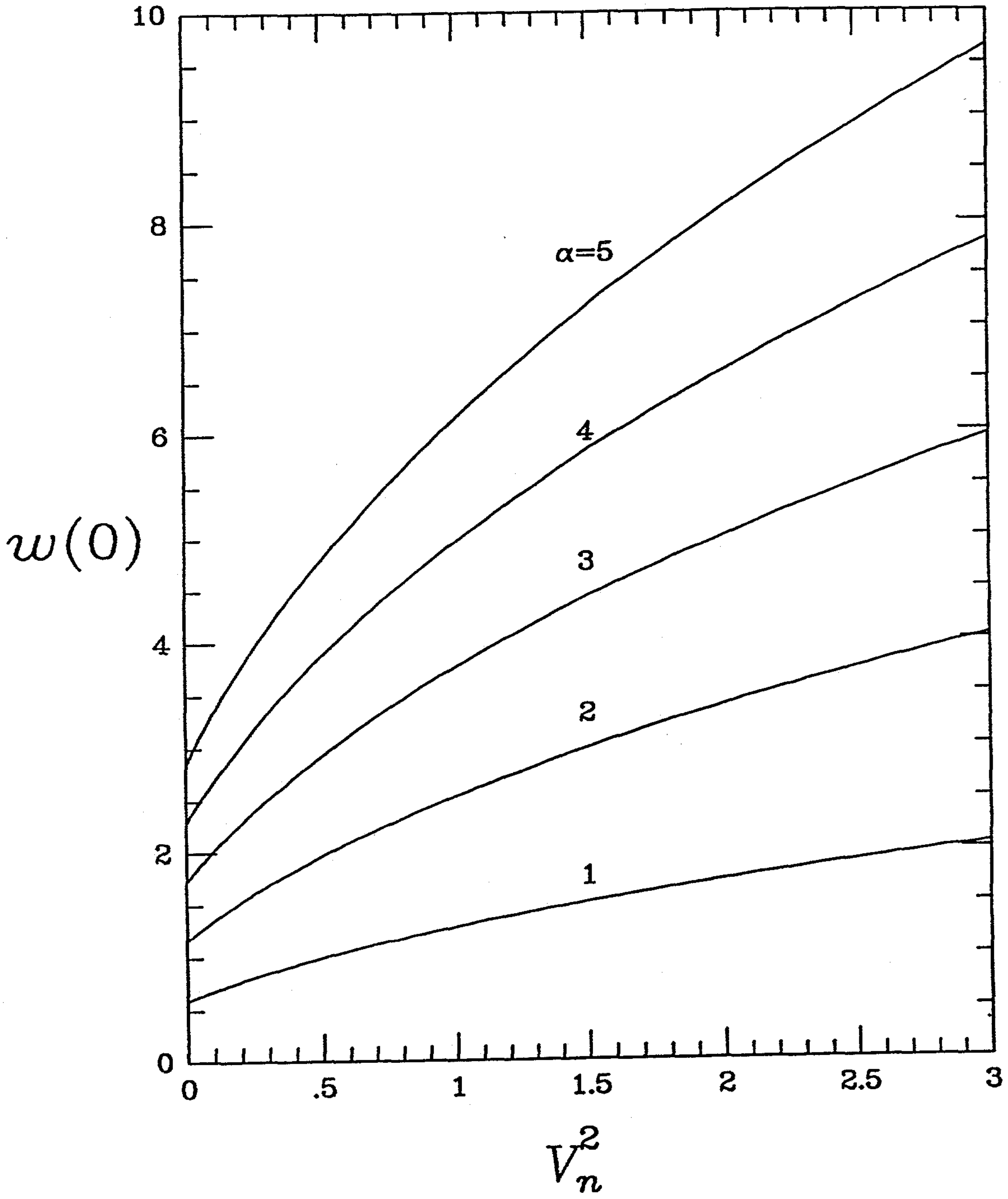

Figure 4.9 The variations of w(0) with V_n^2 for α=1, 2, 3, 4, and 5, when $\theta=\pi/6$, $e=e_w=.9$, and $m_t=5$.

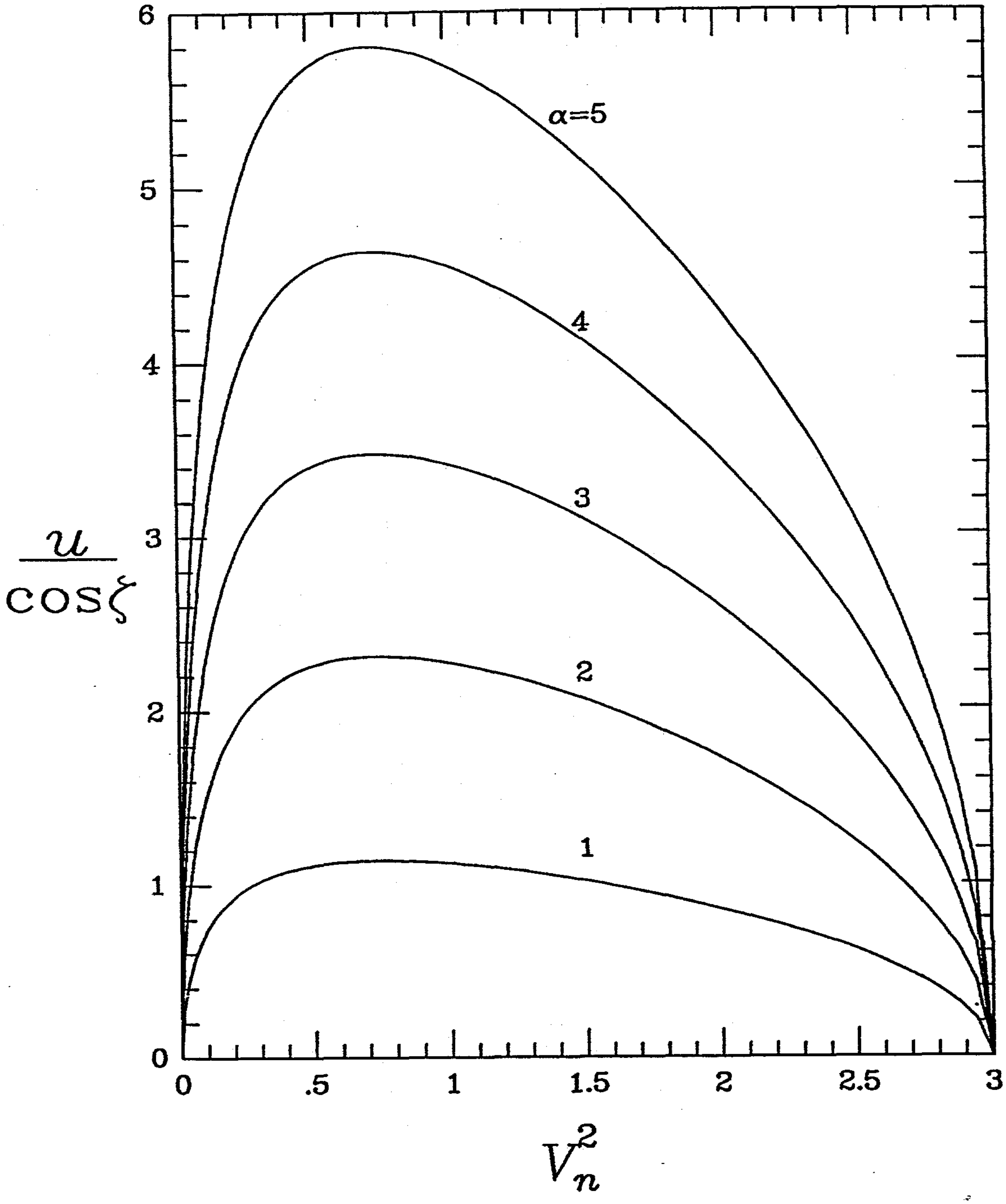

Figure 4.10: The variations of $u/\cos\zeta$ with V_n^2 for α=1, 2, 3, 4, and 5, when $\theta=\pi/6$, $e=e_w=.9$, and $m_t=5$.

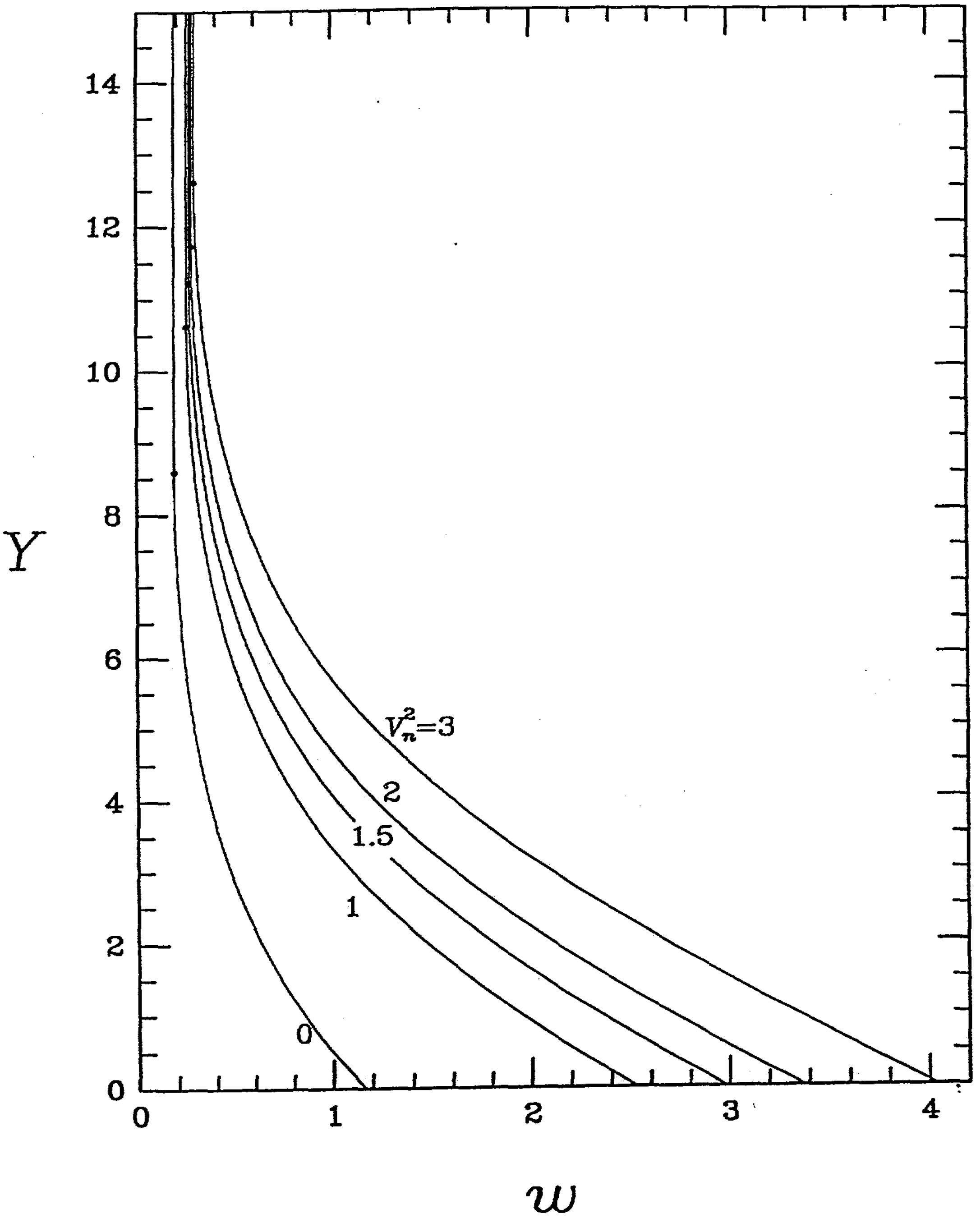

Figure 4.11: The variations of w with Y for V_n^2=0, 1, 1.5, 2, and 3, when α=2, $\theta=\pi/6$, $e=e_w$=.9, and m_t=5. Solid dots on the profiles indicate the value of Y below which 99% of the mass m_t is contained.

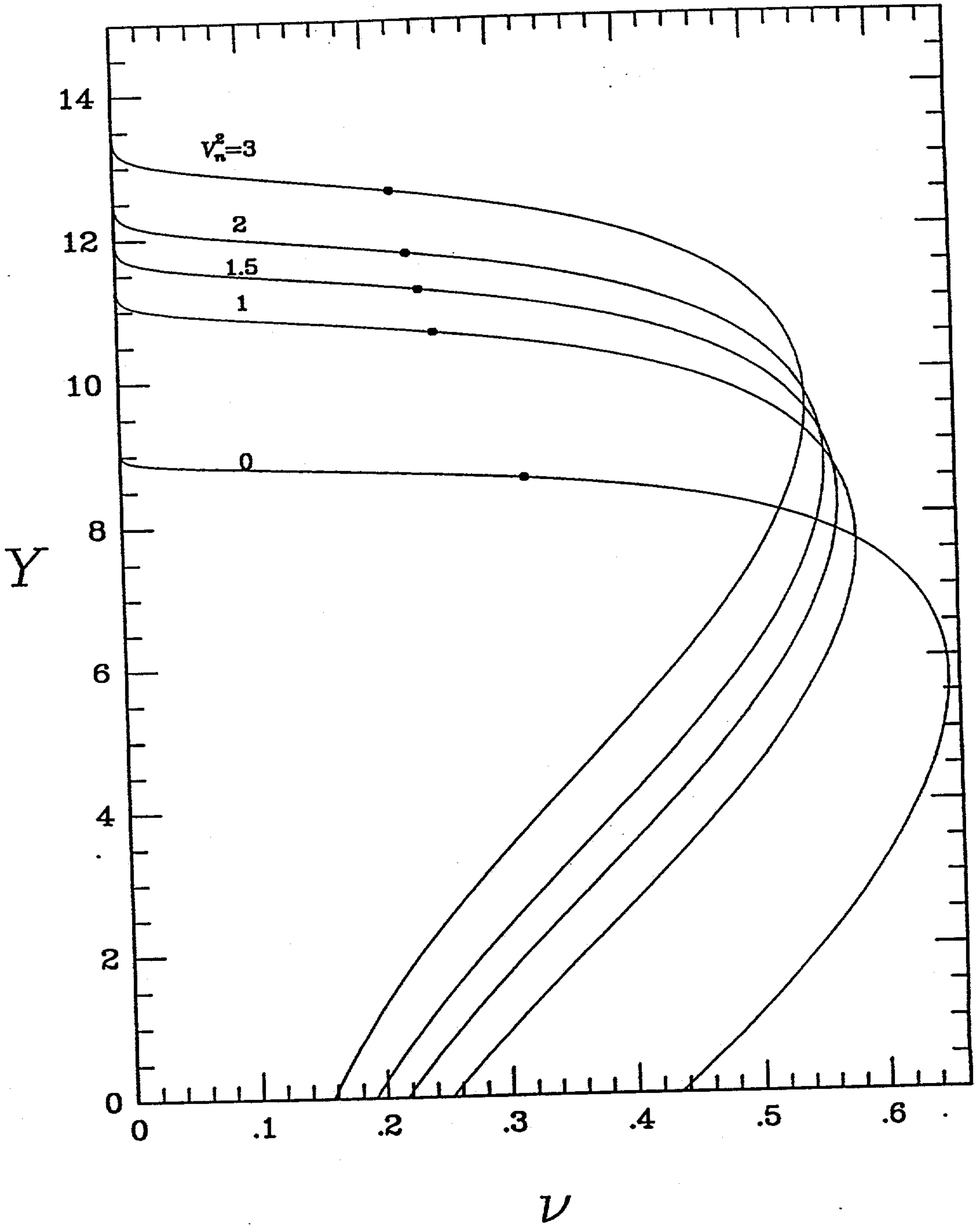

Figure 4.12: The variations of ν with Y for $V_n{}^2$=0, 1, 1.5, 2, and 3, when α=2, θ=π/6, e=e_w=.9, and m_t=5. Solid dots on the profiles indicate the value of Y below which 99% of the mass m_t is contained.

5. REFERENCES

Campbell, C.S., 1989, The Stress Tensor for Simple Shear Flows of a Granular Material, J. Fluid Mech., Vol. 203, pp. 449-473.

Carnhan, N.F., Starling, K.E., 1969, Equation of State of Nonattracting Rigid Spheres, J. Cem. Phys., Vol. 51, pp. 635-636.

Grad, H., On the Kinetic Theory of Rarified Gases, Comm. Pure and Applied Mathematics, Vol. 2, pp. 331-407.

Hopkins, M.A., Shen, H.H., 1992, A Monte Carlo Solution for Rapidly Shearing Granular Flows Based on the Kinetic Theory of Dense Gases, Vol. 244, pp. 477-491.

Jenkins, J.T., Richman, M.W., 1985, Grad's 13 Moment System for a Dense Gas of Inelastic Spheres, Arch. Rat. Mech. Anal., Vol. 87, pp. 355-377.

Johnson, P.C., Nott, P., Jackson, R., 1990, Frictional-Collisional Equations of Motion for Particulate Flows and Their Applications to Chutes, J. Fluid Mech., Vol. 210, pp. 501-535.

Lun, C.K.K., Savage, S.B., 1986, The Effects of an Impact Velocity Dependent Coefficient of Restitution on the Stresses Developed by Sheared Granular Materials, Acta Mech., Vol. 63, pp. 15-44.

Oyediran, A.A., Richman, M.W., Martin, R.E., Alexandrou, A.N., 1992, Granular Flows Down Bumpy Inclines, accepted in Acta Mech.

Richman, M.W., 1988, Boundary Conditions Based upon a Modified Maxwellian Velocity Distribution for Flows of Identical, Smooth, Nearly Elastic Spheres, Acta Mech, Vol. 75, pp. 227-240.

Richman, M.W., 1993, Boundary Conditions for Granular Flows at Randomly Fluctuating Bumpy Boundaries, Mech. Mat'ls., Vol. 16, pp. 211-218.

Richman, M.W., Marciniec, 1990, Gravity-Driven Granular Flows of Smooth, Inelastic Spheres Down Bumpy Inclines, J. Appl. Mech., Vol. 112, pp. 1036-1043.

Richman, M.W., Martin, R.E., 1993, Confined Granular Flows Induced by Identical, Parallel, Vibrating Boundaries, Proc. Symp. Dev. in Non-Newtonian Flows, (eds. D.A. Siginer, W.E. Van Arsdale, M.C. Altan, A.N. Alexandrou), ASME, AMD-Vol. 175, pp. 49-56.

Richman, M.W., Martin, R.E., 1995, The Effects of Anisotropic Boundary Vibration on Confined Thermalized Assemblies, J. Appl. Mech., in press.

Richman, M.W., Martin, R.E. ,1993, A Theory for Flows of Identical, Smooth, Highly Inelastic Spheres, in preparation.

Walton, O.R., Braun, R.L., 1986, Stress Calculations for Assemblies of Inelastic Spheres in Uniform Shear, Acta Mech., Vol. 63, pp. 73-86.

6. APPENDIX

Here we provide the elements of the 5x5 coefficient matrix [C] of equation (2.35). The subscripts on the elements of [C] are unrelated to the x_1-x_2-x_3 coordinate directions.

The first row of equation (2.35) is the differentiated form of shear stress relation (2.7). The coefficients are,

$$C_{11} = \frac{u'}{5\sqrt{\pi\tau}} \quad , \qquad C_{12} = -a_{12}\frac{dH}{dv} - \frac{p_{12}}{2(1+e)(vG)^2}\frac{d(vG)}{dv} \quad , \qquad (A1)$$

and

$$C_{13} = 0 \quad , \qquad C_{14} = -H \quad , \qquad C_{15} = \frac{2\tau^{1/2}}{5\pi^{1/2}} \, . \qquad (A2)$$

The second row of equation (2.35) is the differentiated form of the normal stress relation (2.9). The coefficients are,

$$C_{21} = vGF \quad , \quad C_{22} = \tau\frac{d(vGF)}{dv} + a_{22}\frac{d(vGH)}{dv} \quad , \quad C_{23} = vGH \; , \qquad (A3)$$

and $C_{24}=C_{25}=0$. The third row of equation (2.35) is the energy flux relation (2.11). The coefficients are,

$$C_{31} = \kappa \quad , \qquad C_{32} = \lambda\tau \quad , \qquad C_{33} = \eta \quad , \qquad (A4)$$

and $C_{34}=C_{35}=0$. The fourth row of equation (2.35) is the differentiated form of the x_2-x_2 deviatoric component (2.20) of the balance of second moment. The coefficients are,

$$C_{41} = \frac{-12(1+e)(3-e)vGa_{22}}{5\sqrt{\pi\tau}} \quad , \qquad C_{42} = \frac{-24(1+e)(3-e)\tau^{1/2}a_{22}}{5\pi^{1/2}}\frac{d(vG)}{dv} + a_{12}u' \; , \qquad (A5)$$

and

$$C_{43} = \frac{-24(1+e)(3-e)vG\tau^{1/2}}{5\pi^{1/2}} \quad , \qquad C_{44} = vu' \quad , \qquad C_{45} = va_{12} - \frac{1}{3}p_{12} \, . \qquad (A6)$$

The fifth row of equation (2.35) is the differentiated form of the x_1-x_2 component (2.21) of the balance of second moment. The coefficients are,

$$C_{51} = \frac{6(3-e)a_{12}}{\pi^{1/2}(3e-1)\tau^{3/2}} \;, \quad C_{52} = \frac{5u'}{2(1+e)(3e-1)G^2}\frac{dG}{d\nu} \;, \quad C_{53} = 0 \;, \qquad \text{(A7)}$$

and

$$C_{54} = \frac{-12(3-e)}{\pi^{1/2}(3e-1)\tau^{1/2}} \;, \qquad C_{51} = -\left[\, 1 + \frac{5}{2(1+e)(3e-1)G} \right] \;. \qquad \text{(A8)}$$